Spectroscopic Observation of Materials
under
Dynamic Conditions

by

Gagan Saini

B.E., Indian Institute of Technology Delhi (1999)
M.S., Georgia Institute of Technology (2004)
S.M., Massachusetts Institute of Technology (2006)

Submitted to the Department of Materials Science and Engineering
in partial fulfillment of the requirements for the degree of

DOCTOR OF PHILOSOPHY

at the

MASSACHUSETTS INSTITUTE OF TECHNOLOGY

September 2010

Author . . . .
Department of Materials Science and Engineering
June 2, 2010

Certified by . . . .
Keith A. Nelson
Professor of Chemistry
Thesis Supervisor

Certified by . . . .
Edwin L. Thomas
Morris Cohen Professor of Materials Science and Engineering
Thesis Supervisor

Accepted by . . . .
Christine Ortiz
Chair, Departmental Committee on Graduate Students

Spectroscopic Observation of Materials

under

Dynamic Conditions

by

Gagan Saini

Abstract

A new method is developed for direct real-time visualization of shock generation, propagation, and convergence in a sample. The approach opens up new possibilities for controlling the shock parameters and allows one to access pressures in the multiple gigapascal range. Optical generation of shock waves is followed by optical measurement of sample response during and after shock propagation. In this approach, a shock wave is generated that propagates laterally in the plane of the sample (perpendicular to the direction of the optical beam) rather than through the sample plane as in a more conventional approach. The optical configuration and sample geometry make shock wave formation and propagation directly accessible to optical imaging and spectroscopic probes with wavelengths ranging from UV to far-IR. With proper shaping of the optical shock generation pulse, focusing of the shock response can be initiated to provide increased shock pressure.

The method has been validated through measurements of shock propagation in liquid water that illustrate some of the possibilities for shock generation, control, and measurement, and demonstrate the utility and potential of the new technique. The charge-coupled device (CCD) and streak camera images recorded provide for the first time a direct dynamic picture of cylindrical shock convergence within the nanosecond time window. This unique technique enables rapid and direct measurement of the dynamic shock responses of advanced materials and structures to diagnose and subsequently optimize their readiness in mitigating blast threats.

Thesis Supervisor: Keith A. Nelson
Title: Professor of Chemistry

Thesis Supervisor: Edwin L. Thomas
Title: Morris Cohen Professor of Materials Science and Engineering

"...The woods are lovely, dark and deep,

But I have promises to keep,

And miles to go before I sleep,

And miles to go before I sleep..."

- Robert Frost

Acknowledgments

I strongly believe that scientific research is one area that stretches one's mental faculties beyond the realms of conventional thinking and enables the probing and answering of new queries in the never ending deep quest for knowledge. There are numerous people that have helped me while working on this thesis to constantly raise the bar in order to get the best out of me, and their contributions are greatly appreciated.

First and foremost, I would like to thank both my thesis advisors, *Professor Keith A. Nelson* and *Professor Edwin L. Thomas*, not only for the expert guidance they provided me during my research, but also for providing me the ability to work in a simulating environment eager of discovery and continuous learning. Their vast research experience and scientific intuition have taught me to ask the right questions and to think more critically. Professor Nelson has been a constant source for my motivation and I am always impressed by his dedication towards science. Professor Thomas showed incredible faith in me, and has always been very supportive of my direction of research. I sincerely thank the members of my thesis committee, *Professor Lorna J. Gibson* and *Professor Samuel M. Allen*, for their interest in this work and for providing valuable comments.

I am fortunate enough to work with *Dr. Thomas Pezeril* during his tenure as a post-doctoral associate and beyond. His strong theoretical background and experimental finesse have helped me to design the experimental setup as well to analyze data. We spent many weekends in the lab laboring over alignment and dismal signal quality. He is my mentor as well as my good friend. Special thanks to you, Thomas! *Dr. Steven E. Kooi* has been a great help and I admire his relentless patience in working with me on alignment of laser systems, data collection and analysis. I also share scientific and non-scientific opinions on different matters with him.

I have been blessed to be part of two wonderful research groups - *Nelson Group* and *Thomas Group*. The group members also actively contributed to the development of this work through fruitful discussions and interactions. I would also like to thank *Dr. Cindy Bolme* who is always happy to answer any queries I have related to the experiments and *Christoph Klieber* for his help and support during the period of thesis writing. I am happy to work and collaborate with *Dr. Alexei Maznev*, *Dr. Jae-Hwang Lee*, *Dr. Julian J. Rimoli*, *Dr. Darius Torchinsky*, *Johanna Wendlandt*, *Jeremy Johnson*, *Piotr Fidkowski*, *Taeho Shin*, *Kit Werley*, *Jon Singer*, and *David Veysset* on various projects throughout the course of my stay at MIT.

I am also grateful to administrative staff at Institute for Soldier Nanotechnologies, Department of Materials Science and Engineering, and Department of Chemistry, especially to *Gloria Pless*, *Angelita Mireles*, *Kathleen Farrell* and *Li Miao*. I would like to thank the *U. S. Army Research Office* for their generous funding and continued support to the project even when things were not working as per proposed plan.

Finally, I would like to thank the *family and friends* that have supported me through the ups and downs of graduate student life at MIT. I could not have done it without you. *Thank you!!!*

Dedicated to my loving mother Dr. Santosh Saini,

my beloved father Dr. Om Parkash Saini,

my dear brother Dr. Rajiv Saini,

my sister-in-law Dr. Sughanda Saini,

and to my little nephew Swapnil.

for their love, gratitude and support...

Every journey begins with a single step.

This journey is for you

&

this is the step...

Contents

List of Figures

15

18

List of Tables

Chapter 1

Introduction

The nonlinear viscoelastic dynamics and deformation mechanisms in polymers during and immediately following ballistic or blast events remain obscure because they are extremely difficult to study experimentally. Polymers are known to exhibit strong rate-dependent mechanical behaviors. Also, in different frequency regimes, the rate sensitivities of polymers change as various primary and secondary molecular mobility mechanisms become operative. Because of the experimental difficulties inherent in studying blast, there is currently a limited understanding of the mechanisms of loading, damage and failure of structures, and the mechanisms of injury to humans, produced by blast events. A detailed understanding of how materials respond to ballistic and blast rate shock-loading is critical for the design and development of new protective materials.

Studying the dynamic mechanical behavior within the shocked region of a material during the shock requires specialized techniques and diagnostic equipment [1]. Historically, if one wanted to study materials under ballistic shock loading conditions, a gas gun apparatus was necessary to generate appropriate high strain rate events. The mechanical behavior under laser-shock conditions is quite complex, with shock pulses lasting from less than 100 ps to more than 100 ns, delivering strain rates from 10^6 to $10^9 \, \mathrm{s}^{-1}$ and pressures exceeding several gigapascals [2]. Recent advances in high power ultrafast laser amplifier systems have opened the possibility of optically generating ballistic shocks which reach pressures that are comparable to those in shock

waves generated by a gas gun apparatus.

Regardless of whether a shock wave is laser-driven or results from being inside the blast radius of an improvised explosive device (IED), the impacted material still experiences rapid delivery of high mechanical energy density. Accordingly, the response of a candidate armor material, a biological tissue, or a novel fabric component, tested on micron size scales, could reveal much about its macroscopic response properties.

The characterization of materials subject to shock loading due to ballistic or blast impact is germane to the development of high-performance engineering materials that are optimized for high performance under extreme conditions. This is especially important for soldier armor for personnel protection, since blunt trauma affects human tissue, organs, biopolymers, and gels. Yet due to the rapid and destructive nature of these conditions, direct real-time measurements of time-evolving physical properties of the materials during the response to shock are a big challenge. While post-mortem analysis of shocked materials provides useful information about the overall outcome, it provides little mechanistic insight into how, and on what time scales, the material response evolved under impact. This makes iterative optimization of materials performance extremely difficult. There is still much to be learned about the response of soft and hard matter to violent impacts.

Moreover, advanced multicomponent material systems including block copolymers, multilayer assemblies, self-assembled composites, and others may undergo extremely complex responses to shock including solid-solid phase separation or phase transitions, plastic deformation and cracking, delamination, chemical degradation, melting, vaporization, etc. Direct real-time measurement of mechanical responses during the shock event can reveal failure mechanisms and dynamics that may then be addressed systematically through optimization of individual component performance under impact and optimization of composite phononic properties including tailored reflection, scattering and damping of shock wave components. The time-dependence of structural relaxation and dynamic behavior helps to depict modes of energy dissipation through the material. The dynamics of structural changes induced by ballistic impact and the dissipation of mechanical energy on the time scale of the

24

shock event and thereafter are of obvious concern for the design and effectiveness of protective materials.

Toward this end, a novel pairing of optical shock generation and optical imaging is used, providing a powerful tool for studying the time-dependent material response to large-amplitude short-time mechanical transients. The synergy in their combination allows for the observation of microstructural changes at fast timescales. This thesis presents an experimental protocol for the assessment of material performance under shock loading conditions. The results presented foreshadow more routine measurements of laser shock dynamics in which the shock and the material response to it are characterized. Such measurements could enable the testing of new blast mitigation strategies and the design and optimization of protection systems with improved performance against blast.

This thesis starts off with a description of the use of impulsive stimulated thermal scattering (ISTS), a laser-based photoacoustic technique, to study the propagation of bulk and surface in-plane and through-plane acoustic waves in unshocked materials at ambient temperature and pressure. Chapter 2 presents details of the ISTS setup and measurements on a number of samples including a multilayer sample that shows interesting acoustic properties. A comprehensive set of mechanical properties including elastic, shear, and bulk modulus are obtained by fitting experimental data to a model for acoustic dispersion curves.

In Chapter 3, I present an overview of shock theory and methods of shock characterization. I also review some recent advances on generating shock by various techniques as well as different kinds of tools being used for shock measurement. The chapter includes studies done using a gas gun to generate shock but focuses on methods of laser-induced shock loading. The section on shock wave spectroscopy describes different measurement techniques of probing materials under shock loading like Raman scattering, fluorescence spectroscopy, infrared spectroscopy, and coherent anti-Stokes Raman scattering (CARS). The second half of Chapter 3 focuses on shock wave characterization through interferometric techniques like femtosecond time-resolved spatial interferometry with a Mach-Zehnder interferometer, spectral interferometry or

frequency domain interferometry, ultrafast dynamic ellipsometry, etc. The experimental set-up and data generated through Sagnac interferometry have been shown to provide detailed information about the dynamic properties and pressure profiles of laser-generated shocks propagating in thin metal films.

Chapter 4 demonstrates the coupling of ISTS measurements and laser shock generation in sample structures (polymers sandwiched between aluminum and gold layers, all on a bulk glass or sapphire substrate). Numerical modeling and preliminary experimental results indicate that the ISTS measurements under shock loading are challenging, and the limitations of this technique are discussed.

Chapter 5 introduces a novel method for direct, real-time optical measurement of mechanical responses to shock loading. This chapter presents a unique technique to generate laser-induced in-plane shock waves (or cylindrical shock waves) and is a step forward to understand the non-linear propagation of converging and focusing shock waves. This chapter provides an introduction to the experimental technique with a detailed description of the laser system used for the experiments and an explanation of the method of shock generation. The characterization of an illustrative test sample composed of a thin confined layer of water loaded with carbon nanoparticles is conducted to demonstrate the utility and potential of this new technique.

Chapter 6 details the feasibility of single-shot spatially resolved streak photographic pressure measurements of shock waves in water. Streak camera photography is used to study dynamics of the shock phenomena with high spatial and temporal resolution. Numerical simulations are also provided to support the validity of the experiments.

Finally, Chapter 7 presents a conclusion of this thesis where results are summarized and future directions of research are suggested.

Chapter 2

Impulsive Stimulated Thermal Scattering (ISTS) / Transient Grating Photoacoustics

2.1   Introduction

The determination of thermal and mechanical properties of thin films is of great technological significance for polymer, micro-electronics, defense and bio-medical applications. Elastic properties of a solid are important because they relate to various fundamental solid-state phenomena such as interatomic potentials, equations of state, and phonon spectra [3]. Elastic properties are also linked thermodynamically with specific heat, thermal expansion, Debye temperature, and the Grüneisen parameter. Most importantly, knowledge of elastic constants is essential for many practical applications related to the mechanical properties of a solid: load-deflection, thermoelastic stress, internal strain (residual stress), sound velocities and fracture toughness [4].

Many different techniques have been used including dynamic mechanical analysis (DMA), heat capacity and thermal conductivity measurement methods, ultrasonics, and optical or non-contact methods [5]. These conventional spectroscopic and scanning probe techniques can determine the chemistry, morphology, and electrical

characteristics of the upper near surface region of thin films. It is generally difficult, however, to measure their frequency-dependent mechanical properties. Brillouin light scattering (BLS) spectroscopy, picosecond laser pulses to excite longitudinal waveguide modes, and impulsive stimulated thermal scattering (ISTS) or transient grating (TG) photoacoustics are optical methods used to determine transverse and longitudinal acoustic wave properties.

The longitudinal acoustic phonon spectrum is most commonly measured by BLS spectroscopy [6]. In this technique, a single CW laser beam is incident upon the sample and this light is scattered from the thermal phonons in the material. By measuring the frequency shift at a selected angle for the scattered light, energy and momentum conservation can be used to recover the phonon frequency and wavevector. Measurements conducted at various scattering angles can thus build an acoustic phonon spectrum [7]. Typically the signal levels in Brillouin spectroscopy are very low, and each data point generally requires hours of signal averaging. Extensive angle-dependent studies are rare, especially since at small angles parasitic scattering can overwhelm the signal. To overcome this significant experimental disadvantage, I have chosen the ISTS technique, by which a large, coherent population of acoustic phonons at a user-selected wavevector can be created in the material of interest and then subsequently probed. The presence of this large coherent phonon amplitude boosts signal levels significantly, and the beating of Stokes and anti-Stokes contributions to the scattered light can become large enough that the scattering may even be recorded in time domain on a single-shot basis, as opposed to integrated over several hours in the frequency domain [8]. The ISTS technique is used to generate data from which bulk and thin film properties of novel materials have been evaluated [9].

ISTS is a time-resolved optical spectroscopy technique in which pulsed laser light is used to generate coherent acoustic waves whose time-dependent oscillations and decay are monitored in real time. It is a non-contact, accurate, fast and non-destructive tool for the characterization of acoustic waves in bulk materials and single or multilayer films. In ISTS, two short excitation pulses (preferably pico or femtosecond) derived from the same laser via diffraction of +1 and -1 orders of a 1 D linear phase
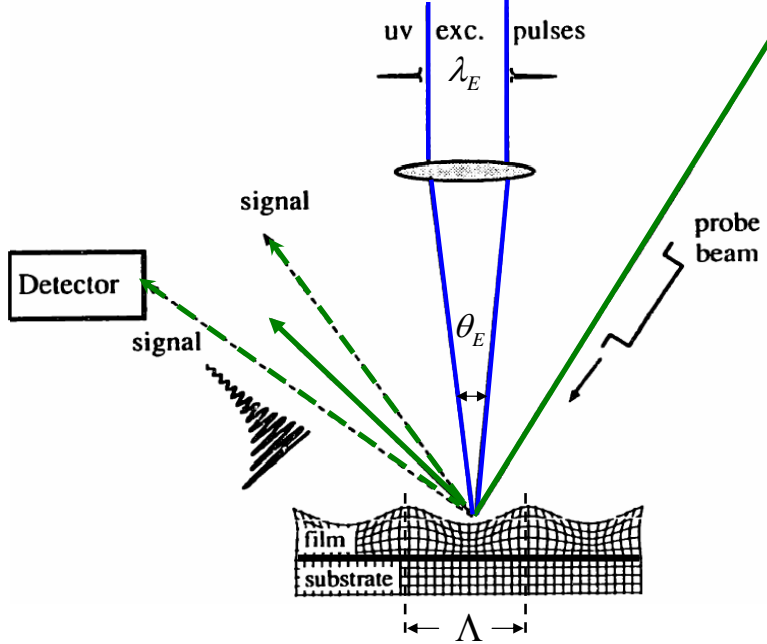
Figure 2-1: Schematic illustration of impulsive stimulated thermal scattering (ISTS) technique. Two ultrashort pump pulses, shown here in blue, are incident on the sample with relative angle θ_E to generate a grating pattern of wavelength Λ, as formulated in Equation 2.1. A probe beam, designated in green, is incident upon the grating at the Bragg angle, and exchanges energy and momentum with material excitations of the grating wavevector. The coherently scattered probe light, shown here by the dashed line, is recorded in the time domain by an amplified photodetector. Figure from reference [11].

mask, are crossed spatially and temporally in an absorbing sample to form an optical interference pattern (see Figure 2-1). The phase mask used in our work is a periodic grating of grooves etched into silica. Optical absorption at the interference maxima leads to mild, spatially periodic sample heating, and thermal expansion at the heated regions launches coherent monochromatic counter-propagating surface acoustic waves which form a transient diffraction grating [10].

The optical interference pattern lasts for only the duration of the laser pulse, and given the short duration of the exciting pulses compared to any acoustic oscillation period, the material is driven impulsively. The excitation so generated shares the grating character of the optical excitation pattern. Once driven, the evolution of this excitation in time is probed by coherent scattering of a separate beam. For optimal scattering to occur, this beam must be introduced at the Bragg diffraction angle set

29

by the wavelength of the imprinted grating. In practical terms, this beam may be a piece of the original driving laser that has been mechanically and incrementally stepped at regular delayed intervals to build up a time-dependent signal trace of diffracted light. With the advent of fast digitizing electronics, it may also be a CW laser whose diffraction off the time-evolving transient material grating is recorded on a digitizing scope.

The magnitude of the in-plane acoustic wavevector, q, is given by

$$q = \frac{4\,\pi\,\sin(\theta_E/2)}{\lambda_E} = \frac{2\,\pi}{\Lambda} \tag{2.1}$$

where λ_E is the wavelength of the excitation pump light, θ_E is the crossing angle between the two excitation pulses at the surface of the thin film (bulk samples also may be used, and the signal may be observed in transmission mode for samples that are not opaque) and Λ is the wavelength of the surface acoustic waves.

The probe beam is coherently scattered or diffracted into the path of the other beam by the acoustic diffraction grating, and the superposed optical fields are detected and subtracted, revealing damped acoustic oscillations on nanosecond time scales (~ 30 MHz - 3 GHz acoustic frequencies). This diffracted signal is collected by fast detection electronics comprised of amplified photodiodes and a transient digitizing oscilloscope to resolve the time-dependent material response.

An acoustic dispersion curve (variation of acoustic frequency with respect to acoustic wavevector) is generated by changing the grating spacing through translation of the phase mask substrate, which contains about 20 patterns that are optimized for diffraction at the wavelength of the excitation laser [12]. The study of pseudo-Rayleigh and pseudo-Lamb acoustic waveguide modes in supported and free-standing layered films has been used to determine the intrinsic mechanical properties of materials in the particular structure or configuration [13, 14]. There is a strong dependence of the acoustic frequency on the elastic properties, density, thickness and mechanical boundary conditions (e.g. substrate adhesion or delamination) of each film in a multilayer stack. Hence, the measurement of multiple acoustic waveguide modes and their dis-

persion reveal acoustic behavior which is then used to extract the elastic and other properties of the film. The detailed quantitative theory of ISTS acoustic excitation and probing processes is well discussed in papers by Yan, Duggal, Rogers and Nelson [15, 16, 17, 18]. For thin films in a multilayer structure, boundary conditions at the interfaces lead to coupling between longitudinal and transverse potentials and hence every surface acoustic mode has both longitudinal and transverse character [19]. In practice, the study of a relatively soft polymeric sample material can be simplified if it is surrounded by stiffer impedance boundaries (e.g. sapphire) so that the acoustic response is well confined within the softer sample.

In what follows, I will first introduce the ISTS or the transient grating technique from a theoretical point of view. From there, I will describe the experimental set-up that has been built and used to perform the photoacoustic measurements made in this thesis. I then proceed with detailed information on materials (fabrication and characterization) which have been studied for various practical applications and conclude with the data analysis of these material systems.

2.2   Theoretical Considerations

Let us consider the ith component of the probe electric field E_{inc}^i incident on an excited portion of the medium. In the linear response regime, the jth component of the scattered electric field E_{sc}^j of the probing laser light is proportional to the change in refractive index δn. As changes in the magnetic permeability $\delta \mu^{ij}$ in such experiments are negligible, the relevant part of the refractive index is the material's permittivity, and so $\delta n \propto \delta \epsilon^{ij}$. Mathematically, the scattered field is proportional to

$$E_{sc}^j(\vec{k} \pm \vec{q}, t) \propto \delta \epsilon^{ij}(\vec{q}, t) E_{inc}^i(\vec{k}, t) \tag{2.2}$$

where $\vec{k}$ is the incident wavevector, $\vec{k} + \vec{q}$ is the scattered wavevector, and $\vec{q}$ is the transient grating wavevector.

Equation 2.2 states that in order to compute the signal embedded in the time-

31

dependence of E_{sc}^j, I need to compute the time-dependence of the material's permittivity, or equivalently its polarizability, induced by the pump laser. This quantity couples to many of the intensive variables of the system. For longitudinal waves, which create variations in density, the variables that concern us are density ρ and temperature T. The importance of the former is obvious whereas the latter is relevant mainly for the reason that changes in temperature are usually strongly coupled to changes in density.

The theory for ISTS has been developed elsewhere for the case of longitudinal waves and I will review the derivation below [8, 20].

2.2.1   ISTS Theory

The ISTS or the transient grating experiment, as depicted in Figure 2-1, results from the action of two coherent, polarized pulses of equal field strength incident upon the sample at an angle θ_E. The intersection of these two beams results in a modulation of the overall field with period Λ. The field may interact with the sample through electrostriction, which instantaneously induces stresses in the material and launches a longitudinal wave. The second mechanism of longitudinal-wave excitation is by the absorption of the excitation light into the sample, either into electronic or vibrational degrees of freedom. In either the electronic or vibrational route, the absorbed energy is rapidly thermalized, and the result is a grating pattern in temperature. Regions of higher temperature have a lower equilibrium density, and so the resulting step-function compressional stress launches longitudinal acoustic waves with force $F \propto \delta T$. This process of launching acoustic waves via sudden heating is known as *impulsive stimulated thermal scattering* (or ISTS).

Using linearized equations of motion, Fourier transformed from real space to the wavevector domain, representing conservation of mass, momentum and energy, I can solve the system to get the ISTS response function $G_{\rho T}$ given by

$$G_{\rho T}(q, s) = \frac{1}{\Delta} \left\{ -\frac{\kappa q^2}{c_v} \frac{k_B T_0}{S(q)} \right\} \tag{2.3}$$

where κ is the thermal expansion coefficient, T_0 is the local temperature, c_v is the specific heat at constant volume, q is the wavevector, s is the Laplace variable, k_B is the Boltzmann constant, $S(q)$ is the static structure factor, and Δ is the dispersion relation simplified using the Debye approximation and is given by

$$\Delta = (s + \Gamma_H)(s + i\omega_A + \Gamma_A)(s - i\omega_A + \Gamma_A)\left[s + \frac{c_0^2}{c_A^2 \tau_R}\right] = 0 \tag{2.4}$$

where $\Gamma_H = \chi q^2$ is the thermal diffusion rate, $\chi = \zeta/\rho_0 c_p$ is the thermal diffusivity, ζ is the thermal conductivity, c_p is the specific heat capacity at constant pressure, c_0 is zero-frequency longitudinal acoustic speed, Γ_A is the acoustic damping rate, ω_A is the acoustic frequency, c_A is the acoustic speed, and τ_R is the Debye relaxation time.

The roots of Equation 2.4 determine the nature of the excitations observed in the system. Complex roots indicate propagating excitations, and real roots relate to diffusive ones. The first root is purely real, and provides the thermal diffusion time Γ_H. This represents the decay of the induced grating response via the transport of heat from the grating peaks to nulls. The other real root is the fourth term which denotes another dissipative mode. In this case it has a time scale related to the relaxation time τ_R, which implies a time-dependent transient grating response due to structural relaxation.

The second and third terms in Equation 2.4 represent left and right propagating acoustic waves of frequency ω_A and damping rate Γ_A. The acoustic frequency is given by

$$\omega_A = c_A q = c_0 q \left[D + \sqrt{D^2 + (c_0 q \tau_R)^{-2}} \right]^{1/2} \tag{2.5}$$

33

where

$$D = \frac{1}{2}\left[c_\infty^2 c_0^{-2} - (c_0 q \tau_R)^{-2}\right] \tag{2.6}$$

where c_∞ is the infinite frequency longitudinal acoustic speed.

The signal in an ISTS experiment Laplace transformed back into the time domain is thus given by

$$G_{\rho T} = A\left[e^{-\Gamma_H t} - e^{-\Gamma_A t}cos(\omega_A t)\right] + B\left[e^{-\Gamma_H t} - e^{-c_0^2 c_A^{-2} t/\tau_R}\right] \tag{2.7}$$

where

$$A = -\frac{\kappa}{c_p} \frac{c_0^2}{c_A^2} \frac{c_A^2 q^2 \tau_R^2 + c_0^2 c_A^{-2}}{c_A^2 q^2 \tau_R^2 + c_0^4 c_A^{-4}} \tag{2.8}$$

and

$$B = -\frac{\kappa}{c_p} \frac{q^2 \tau_R^2 (c_A^2 - c_0^2)}{c_A^2 q^2 \tau_R^2 + c_0^4 c_A^{-4}} \tag{2.9}$$

ISTS signal given by Equation 2.7 is split into contributions due to simple driven acoustic and thermal responses (proportional to A) and contributions from the structural relaxation dynamics (proportional to B). In practice, I am able to use this to recover relaxation dynamics from $\sim 10^{-7}$ s to $\sim 10^{-3}$ s, limited on the shorter time-scales by the acoustic response and on longer time scales by thermal diffusion or the repetition rate of the measurement. The most common information provided by ISTS is mapping of the structural relaxation spectrum through the measured acoustic parameters and thermal expansion dynamics.

ISTS response contains a single amplitude term A that multiplies both dynamical parts, thermal diffusion and acoustic responses. The total response consists of a steady-state response, the thermal expansion, and a transient response, the acoustic oscillations, the latter arising because the driving force is sudden and the response overshoots the steady-state value, by exactly the steady-state amplitude amount, so
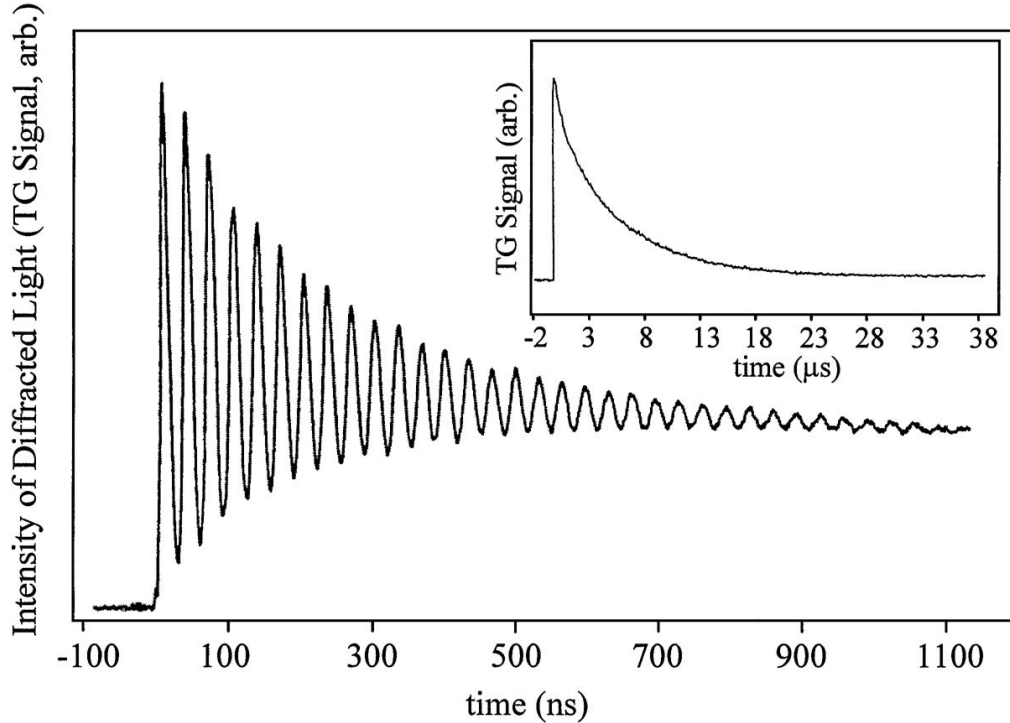
Figure 2-2: Typical ISTS signal showing temporal behavior of probe light diffracted by motions induced with picosecond laser pulses crossed at the surface of a 4.40 μm, free-standing polyimide film with an acoustic wavelength of 20.55 μm. The onset of diffraction coincides with the arrival of the excitation pulses. The oscillations are associated with acoustic standing waves. The inset shows the signal on microsecond time scales; the slow decay is associated with the thermal component of the response. The frequencies and decay rates of the oscillations define the acoustic velocities and attenuation rates. The rate of decay of the thermal component can be used to determine the in - and out-of-plane thermal diffusivities. Figure from reference [13].

I have oscillations between the acoustic maximum and zero about the steady-state amplitude until they are acoustically damped, then on longer time scales thermal diffusion from grating peak to null removes the steady-state response. Equation 2.7 is used to extract acoustic parameters, thermal diffusivities and thermal conductivities. Figure 2-2 shows a typical ISTS signal generated from coherently excited surface phonons in the time domain.

The precise nature of the displacements in a film-substrate assembly will depend on important details including the shear and bulk moduli of all the film layers and the substrate and on where the heat is deposited (e.g. only at the front of a thick

35

layer, roughly uniformly throughout a thin layer, throughout many layers and the substrate surface, etc.). These factors determine the initial, impulsively imposed heat distribution, the anisotropic compressional and shear stress distributions resulting from it, and the projection of the overall response along different acoustic waveguide modes whose displacements relieve the stresses. The key information that I extract does not come from precise determination of the acoustic amplitude but only from the dynamics of the response, i.e. acoustic frequencies and decay rates [21].

On the other hand, in some samples there is complex structural relaxation on a time scale that is long compared to the acoustic oscillation period but shorter than the thermal diffusion time. This makes it take longer to reach the steady-state thermal expansion response, and so the steady-state response then consists of a fast part A, which is still the acoustic amplitude, plus a slow part. The slow part would normally have some distinct dynamics associated with the slow structural relaxation, at the very least a single-exponential rise time [13, 22].

Material properties influence the ISTS signal intensity based on thermal expansion due to laser excitation. Gold produces a strong ISTS signal, since it exhibits a large amplitude signal A, and this is the reason I have an overlayer of gold on top of polymer for several samples studied by this technique. A polymer that absorbs the pump or excitation wavelength strongly and whose ISTS signal can be probed directly would not need the gold overlayer for signal enhancement.

2.2.2   Homodyne versus Heterodyne Detection

The diffracted intensities in an ISTS experiment can range anywhere from 10^{-5} at best to 10^{-8} of the incident probe intensity depending upon the efficiency of the pumping as well as diffraction. As the probing field needs to be weak relative to the pump to avoid further exciting the sample, detection of small signal fields can present a significant challenge. To overcome this difficulty, I have taken advantage of the principle of heterodyne detection to boost detectable signal levels. In this case, the time-dependent signal field $E_{sc}(t)$ is superposed upon a static, coherent local oscillator or "reference" field E_{LO} which is typically several orders of magnitude

larger than $E_{sc}(t)$. The intensity registered by the detector is then given by

$$I = |E_{sc}(t) + E_{LO}|^2 = |E_{sc}(t)|^2 + |E_{LO}|^2 + 2cos(\varphi)E_{sc}(t)E_{LO} \qquad (2.10)$$

where φ is the optical phase between the scattered and local oscillator (LO) fields.

In Equation 2.10, $E_{sc}(t)^2$ is the intensity of the original scattered field. It is called the homodyne contribution, and its quadratic dependence indicates that a sinusoidal signal will be detected at twice its frequency. The homodyne signal may be considered negligible if the LO field amplitude is adjusted properly.

E_{LO}^2 is a static quantity and provides a large DC offset; having no time-dependence, it can also be ignored. Thus, I see that amplification is provided by the cross term, or heterodyne contribution $2cos(\varphi)E_{sc}(t)E_{LO}$, which gives the time-dependence of the field $E_{sc}(t)$ itself. I note that the optical phase φ must be optimized to provide the largest possible signal, and may be adjusted to provide a positive or negative signal relative to the baseline provided by E_{LO}^2.

2.3 Experimental System

Figure 2-3 shows the ISTS experimental arrangement in reflection geometry for opaque samples. The set-up has also been used in transmission mode for transparent materials. The pump and probe beams are focused onto the mask with spherical lenses (not shown in Figure 2-3). A phase mask is used to diffract the short excitation laser pulse (250 fs, $\lambda = 400$ nm, 500 μJ, from an amplified Ti:sapphire laser system) into multiple orders. The phase mask or diffraction grating is designed to optimize the diffraction efficiency of incident pump light into the first (± 1) diffraction orders. These first order diffraction maxima are recombined by a spherical lens that images the mask pattern onto the sample using a one-lens imaging system, while all the higher orders and the zero order beams are blocked by a spatial filter.

The excitation wavevector q can be varied between 1.5×10^5 m^{-1} and 1.5×10^6 m^{-1} by translating the phase mask to locations on it having etched patterns with different
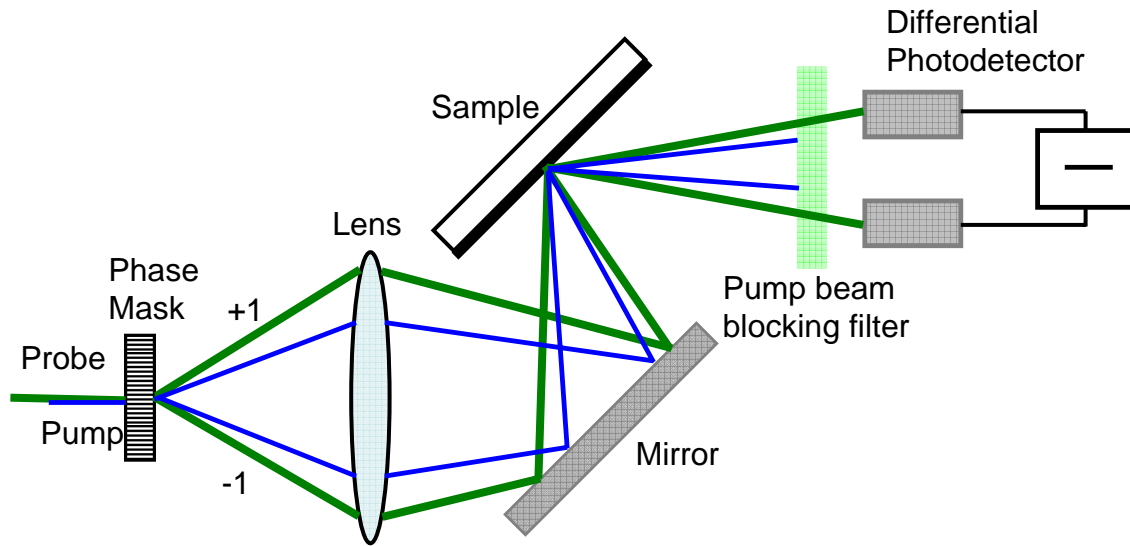
Figure 2-3: Schematic diagram of impulsive stimulated thermal scattering (ISTS) experiment. The pump (i.e., excitation) pulses, shown in blue, are 250 fs in duration and 400 nm in wavelength, generated using an amplified Ti:sapphire laser system. The 532 nm continuous-wave probe (i.e., detection) laser beam, shown in green, is generated by a single-mode Nd:YAG laser. Pump and probe beams are diffracted into ± 1 orders by a binary phase mask pattern. The two resulting pump beams are recombined to form the spatially periodic excitation pattern that results in coherent acoustic wave generation. The two probe beams are used for optical heterodyne detection of time-dependent signal that is diffracted by the acoustic response. The phase mask pattern is one of many with different spatial periods on a glass slide, so the acoustic wave vector may be varied by moving different patterns into the beam path.
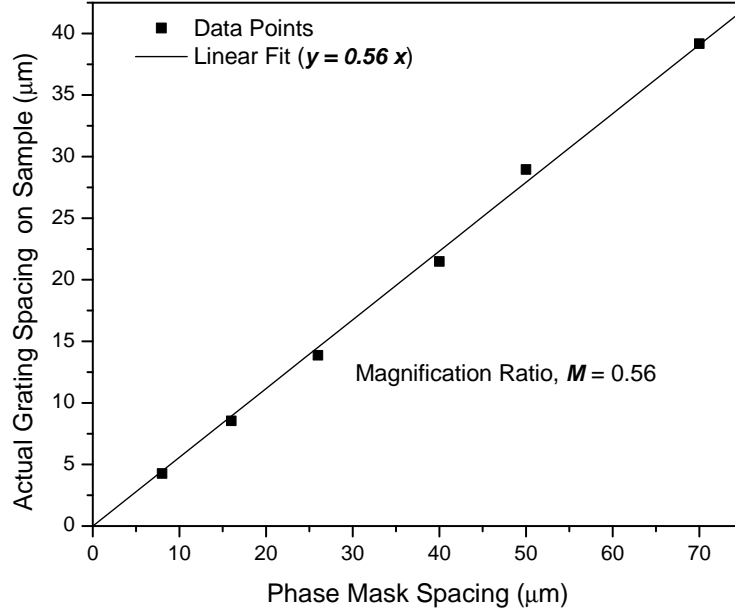
Figure 2-4: Calibration of transient grating spacing in ethylene glycol using a series of phase masks with different spatial periods. The imaging ratio for the one lens focusing system is 1:0.56.

periods. The time-dependent material response is monitored by a CW probe laser beam (532 nm, 30 mW, Coherent Verdi) that is incident on the phase mask parallel to and directly above the excitation beam. The reflected part of each probe beam is collinear with and phase-coherent with the diffracted signal from the other probe beam, and the collinear probe and diffracted signal superpose to permit optical heterodyne detection of the signal. Detection of acoustic waves is performed by a custom-built differential detector (Cummings Electronics Laboratory, Model 3031-0003 amplified avalanche photodiode) whose amplification has a bandwidth of approximately $10\,\mathrm{kHz}$ - $3\,\mathrm{GHz}$. The AC coupling allows for measurement of induced gratings without a fluctuating background due to pointing instability and fluctuations in the local oscillator field E_{LO}. The signal is then averaged by a fast digitizing oscilloscope (Tektronix TDS 7404, $4\,\mathrm{GHz}$).

The transient grating wavelengths generated by the different phase mask patterns were carefully calibrated to within 1% accuracy prior to the experiment, by making ISTS measurements in ethylene glycol doped with $10^{-3}\,\mathrm{M}$ Coumarin 515 laser dye at 294 K (room temperature) in transmission mode (See Figure 2-4). Ethylene glycol
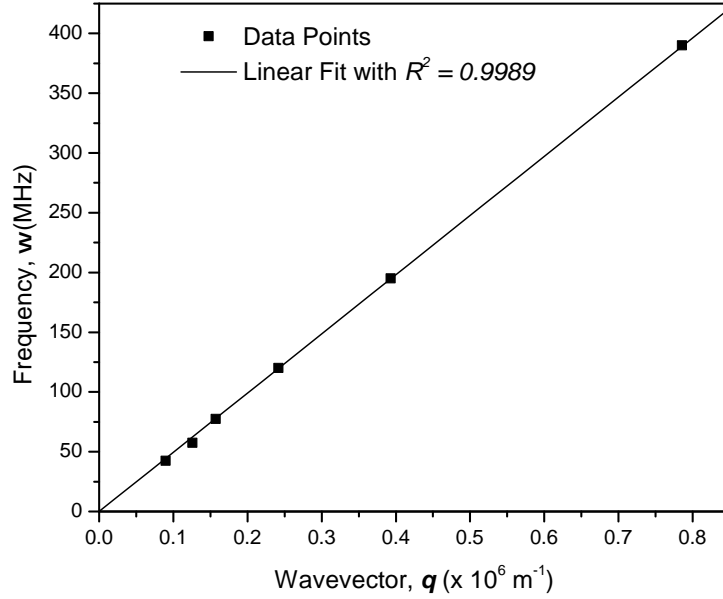
Figure 2-5: Dispersion relation showing acoustic frequency versus wavevector for ethylene glycol at 294 K. Notice the linear relationship suggesting zero dispersion or constant acoustic speed independent of wavevector in this range.

has a temperature-dependent acoustic velocity v near room temperature [23] given by

$$v\,(km/s) = 1.658 - 2.1 \times 10^{-3}\,(T - 298) \tag{2.11}$$

where T is the temperature in Kelvin.

2.4 Material Systems

This section will focus on the motivation to study thin films and multilayer structures of polymers, ceramics and metals. I will present ISTS studies on polymers (poly(methyl methacrylate), polystyrene, polyimide, polycarbonate, polydimethylsiloxane), nanocrystalline materials (titania), multilayer structures, ceramic materials (boron carbide and aluminum oxynitride).

40

2.4.1 Multilayer Thin Films

The mechanical behavior of multicomponent materials that contain ordered or partially ordered domains can be markedly different from those exhibited by each individual neat component [24]. This opens the possibility to optimize mechanical properties of materials for specialized applications based on the manner in which the individual components are combined and structured. Amorphous polymers such as poly(methyl methacrylate) (PMMA) and nanocrystalline materials such as titania (TiO_2) are particularly attractive for many engineering applications due to their intrinsic properties including transparency, relatively high moduli, and ease of processibility, which enable a wide range of systematically variable multicomponent morphologies to be produced [25].

In multilayer systems with these components, it should be possible to control the mechanical behavior, as well as the acoustic properties including phase and group velocity dispersion and possibly phononic bandgap structure, by controlling the ordering and thickness of each individual layer and/or by optimizing the number of layers [26, 27]. I have used multilayer structures of PMMA and TiO_2 nanoparticles as model systems to understand the mechanical behavior of complex multilayer stacks. A better understanding of the mechanical properties of these types of systems will be used in the design of new materials for energy-dissipation applications [28].

2.4.2 Polymer Films

As discussed earlier, non-destructive probing of elastic properties has become a state-of-art approach in thin film research and applications because of recent advances and growing popularity of acousto-optical methods, in particular, BLS and ISTS [29]. The ability of these methods to measure acoustic waves propagating along different directions in a sample can hardly be overestimated for anisotropic films, frequently found in practical applications (stretched packing films, for example). Mechanical anisotropy correlates with preferred orientation of structural units in tested material; this correlation is extensively used to analyze the effect of processing conditions on

41

structure and mechanical stability of films. It should be noted that the other parameter widely used for anisotropy characterization is optical birefringence, which shows much less sensitivity than the elastic modulus tensor in some polymer films.

The study of highly anisotropic supported polyimide films has been reported in the present work. Polyimide coatings chosen for this investigation are well known for their directionally dependent properties; both free-standing and supported polyimide films are often used as model polymer layers with strong uniaxial anisotropy of optical, mechanical, and thermal characteristics. Moreover, outstanding mechanical properties, high dimensional and thermal stability, low thermal expansion, and low dielectric constant of polyimide make it the material of choice for protective coatings and for interlayer dielectrics and passivation layers in the microelectronic industry. Aromatic polyimides are the most successful and widely used polymeric high-performance material for space applications. The high technological importance of polyimide coatings calls for adequate directionally dependent characterization tools, and thus application of ISTS to such films is practically important.

Other materials systems used in the studies were polymer films of polystyrene (PS), polydimethylsiloxane (PDMS), SU-8 (epoxy-based negative photoresist), polycarbonate (PC) and Ceraset$^{\circledR}$ polysilazanes.

2.4.3   Ceramic Materials

Ceramic materials may have a crystalline or partly crystalline structure, or may be amorphous (i.e. glass). The two ceramic materials I will focus on are aluminum oxynitride and boron carbide.

Aluminum Oxynitride

Aluminum oxynitride (AlON) is a polycrystalline transparent ceramic and a premier armor material. It has excellent mechanical properties and thus is a viable material for applications requiring high hardness, mechanical strength, and broad electromagnetic transparency [30, 31]. AlON films are widely applied as protective coatings against

42

wear, diffusion and corrosion, optical coatings, opto-electronics, micro-electronics, and other fields of technology. This is due to the possibility for a broad combination of the physical and chemical properties of the oxynitride films with variable concentrations of aluminum, oxygen, and nitrogen. The film properties can be tailored between those of pure aluminum oxide (Al_2O_3) and aluminum nitride (AlN), depending on the application [32, 33]. AlON has a cubic spinel crystal structure with a melting temperature, T_m, close to $2150\,°C$, and a mass density, ρ, around $3.69\,g/cm^3$ [34].

Boron Carbide

B_4C is the third hardest existing material after diamond and cubic BN with hardness of 41 GPa and elastic modulus of 540 GPa, and its collection of unique properties together with its relatively easy fabrication makes it suitable for many diverse applications such as bulletproof armor, rocket propulsion, neutron absorption, and abrasive powder [35, 36]. Stoichiometric B_4C has a rhombohehral structure with an ultra-high melting temperature, T_m, close to $2450\,°C$, and a low mass density, ρ, around $2.52\,g/cm^3$ [37].

2.5 Sample Preparation

Fabrication and Characterization

Typically, the sample is a multilayer structure with a substrate, either silica glass or sapphire, and then adding other material layers as per need using spin-coating (for polymeric materials) and e-beam deposition for metals like aluminum and gold. Various fabrication steps are required to build layer-by-layer the final sample and this needs precision and accuracy. The thicknesses and uniformity of the multilayers are characterized using ellipsometry, profilometry, and atomic force microscopy (AFM). On the other hand, some samples have been scanned under SEM or TEM, where a multilayer film cross section is prepared by focused ion beam (FIB) cross sectioning.

2.5.1 PMMA -TiO$_2$ Multilayer Structure[*]

Inorganic TiO$_2$ nanoparticles and PMMA have been used as high and low elastic modulus materials, respectively, for constructing multilayer phononic structures. TiO$_2$ nanoparticles were prepared by the synthetic scheme of Sanchez et al. [38]. The nanocrystalline TiO$_2$ particles were composed of anatase phase (refractive index ~ 1.85 at 500 nm) with an average diameter of about 1 to 5 nm. The TiO$_2$ nanoparticles attached with an organic surface capping group (acetylacetone) were readily dissolved in butanol. I estimate the weight fraction of TiO$_2$ nanoparticles in thin film to be around 90% to 95%. PMMA (Aldrich, St. Louis, MO, M$_w$: 15,000 g/mol) was used as received and dissolved in toluene. For fabrication of an organic-inorganic multilayer phononic structure, (TiO$_2$-PMMA)$_5$, solutions of TiO$_2$ (in butanol) and PMMA (in toluene) were alternately spin coated on a glass substrate to target thicknesses, based on phononic bandgap models [27], of 110 nm (TiO$_2$) and 135 nm (PMMA). The thicknesses were controlled by concentration of the solution, amount of solution, and spin speed. A final gold layer (130 nm thick) was deposited by e -beam so that the ISTS excitation pulses would be strongly absorbed and the probe light would be highly reflected. The final sample assembly is shown in Figure 2-6.
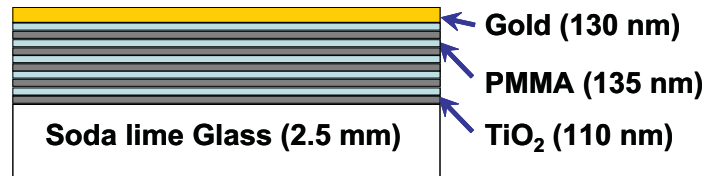
Figure 2-6: Depiction of sample assembly for PMMA-TiO$_2$ multilayer structure used in ISTS measurements (not to scale).

2.5.2 Polymer Films

Several types of transparent substrates were used. Type 1, 25 mm diameter microscope cover slides made of optical borosilicate glass (Fisher brand 25CIR-1D) were used most. Other substrates used were BK-7 glass, sapphire, polycarbonate and

---

[*]Done collaboratively with Jongseung Yoon in the group of Prof. Edwin L. Thomas

PMMA. All substrates were cleaned before use by plasma surface treatment and etching system (Plasma Etch).

Polymer films (PS or PMMA) were spin-coated onto the glass substrate to get desired thicknesses of the samples used in this investigation. The polymer film thickness was a function of the solvent used, the concentration of the polymer solution, and the rotational speed of the spin-coater. For PS and PMMA, the solvent of choice was found to be toluene because it readily dissolves both polymers and has a high boiling point, so it does not volatilize too rapidly [39]. The spin time for all the samples was one minute, with thirty seconds allowed for deceleration to a complete stop. To remove the solvent, the films were baked at $90\,^{\circ}\mathrm{C}$, below the boiling point of toluene, for approximately 30 minutes. To increase thickness uniformity, the films can be annealed around the T_g of the polymer, but this was not found to be necessary after investigation of surface roughness by AFM. The spin-coating apparatus used can make a significant difference in thickness uniformity. Films were initially coated using the Specialty Coating Systems G3P-8 spincoater. This particular model required a constant nitrogen purge in the spinning chamber. The result is very large film thickness variation along the radius due to currents caused by the nitrogen flow. To resolve this, a spincoater from Laurel Technologies, WS400-A 6NPP Lite, was employed since it operates without needing external gas flow.

Thickness uniformity and accurate measurement of the polymer film thickness were extremely important in this experiment since either thickness or acoustic velocity were required to effectively interpret the time-resolved signal. Profilometry and ellipsometry can be used to measure the polymer film thickness. Profilometry was best suited for a polymer monolayer on a hard substrate, such as silicon or sapphire. This technique, while reasonably accurate ($\pm 1\,\mathrm{nm}$), was not preferred since it locally damages the film. Thus, ellipsometry was used to evaluate the thickness of a polymer film on a substrate such as silicon, though it becomes very difficult for transparent substrates such as sapphire.

For polyimide films, substrates were primed by a 0.1% solution of DuPont VM-651 (active component is 3-aminopropyltriethoxysilane) in deionized water. The puddle

of the primer stood on a substrate for 20 s. The substrate was spin dried for 60 s at 3000 rpm. The thickness of the priming layer was estimated by ellipsometry using a three-wavelength nulling ellipsometer AutoElII-NIR-3 (Rudolph Technologies). Measured thickness value of 1.6 nm was in good agreement with literature data [40]. Poly(biphenyl dianhydride-p-phenylenediamine) (BPDA-PDA) polyimide films were applied on the primed side of glass slides by spin coating at 1000 - 3000 rpm for 60 s. Both DuPont PI-2610 polyamic acid precursor and its solutions in N-methyl-2-pirrolidone were used. The diluted precursor with concentrations ranging from 40% and above was used for the thinnest coatings (<1 μm thick). Neat precursor was used for the fabrication of thicker coatings. Immediately after coating, the slides/wafers were soft-baked at 130 °C for 90 s on a hot plate. To obtain thick (10 - 20 μm) films, multiple-coating technique after soft-bake were used, and the spin-coating was repeated. The final curing was done in a vacuum oven at 350 °C for 24 h; the ramp rate was 1 °C/min.

2.5.3 Ceramic Materials

Aluminum Oxynitride and Boron Carbide

Ceramic samples of aluminum oxynitride and boron carbide were provided by Dr. Dattatraya P. Dandekar from Army Research Laboratory (Aberdeen Proving Ground, MD). The samples were 25 mm diameter and 2 mm thick solids. A thin (310 nm) gold layer was deposited by e-beam so that the ISTS signal intensity was enhanced.

2.6 ISTS Data and Analysis

2.6.1 Data Acquisition and Processing

ISTS photoacoustic measurements were made using the experimental setup shown in Figure 2-3. The acoustic wave-vector magnitude q and corresponding frequency $\omega(q)$ were determined by the angle between the excitation pulses which controlled the associated optical interference fringe spacing. The detector was attached to a

Tektronix model TDS-7404 digital oscilloscope which has a bandwidth from DC to 4 GHz. The oscilloscope was externally controlled via GPIB interface and the data traces recorded on a computer using a home-made Agilent VEE program. The data were averaged over 25 - 50 repetitive measurements.

2.6.2 Data Analysis

Measurement of multiple (or single) acoustic waveguide modes at various acoustic wavelengths yields their acoustic dispersion relation, that is acoustic frequency as a function of wavevector, $\omega(q)$, which can be used to extract the elastic properties of the films. The analysis begins with Fourier transformation of the data which yields the acoustic frequency of each mode observed at each wavelength. The dispersion curves are calculated as solutions of the thermoelastic equations of motion for a multilayer system, using numerical code that allows the measured dispersion data to be fit with variable material parameters in order to determine the parameter values.

The analysis of the dispersion results was done by iteratively varying parameters such as layer thicknesses, densities, and longitudinal and transverse acoustic velocities. Initially, thickness and density of the films were fixed to roughly estimated values and the fitting was done by varying the longitudinal and transverse velocities of the films. When the best fit was obtained, the thickness and density were also varied to see if this give a closer fit or not. The sum of squared differences between the measured dispersion and calculations provides a metric for the quality of the model. When the model fit the data well, a set of elastic constants including Young's modulus E, shear modulus G, bulk modulus K, and Poisson's ratio ν could be calculated using Equations 2.12 - 2.15.

$$K = \rho \left(v_l^2 - \frac{4}{3} v_t^2 \right) \tag{2.12}$$

$$G = \rho \, v_t^2 \tag{2.13}$$

$$E = \frac{3 \, K \, G}{K + \frac{1}{3} \, G} \tag{2.14}$$

$$\nu = \frac{E}{2G} - 1 \tag{2.15}$$

where ρ is the density, v_t is the shear velocity, and v_l is the longitudinal velocity.

2.7   Results and Discussion

2.7.1   Multilayer Organic/Inorganic Hybrid Structure

The acoustic dispersion curves of PMMA, TiO_2 nanoparticles, and PMMA-TiO_2 multilayers were determined in order to characterize the evolution of mechanical properties of the multilayer structure. There is a strong dependence of the acoustic frequency on the elastic properties, density, thickness, and mechanical boundary conditions (e.g., substrate adhesion or delamination) of each film in a multilayer stack. The measurement of multiple acoustic waveguide modes and their dispersion reveal acoustic behavior that can then be used to extract the elastic properties of the film by fitting of a multilayer acoustic model to the experimental data [9].

Representative ISTS data from a PMMA-TiO_2 multilayer structure (depicted in Figure 2-6) at 12 μm acoustic wavelength are shown in Figure 2-7. In each case the substrate was soda-lime glass and there was a 130 nm gold overlayer. The data show time-dependent acoustic oscillations and their decay. The acoustic frequencies were extracted through Fourier transformation of the data. Multiple frequencies indicate several acoustic waveguide modes that were excited and probed in the measurement.

The dispersion curves of the samples investigated are shown in Figure 2-8 (a). These dispersion curves are derived from acoustic frequencies measured in the multilayer structure at different experimentally set wavevectors as displayed in Figure 2-7. In the case of a thin films, pseudo-Rayleigh and pseudo-Lamb surface acoustic waveguide modes are generated. When the acoustic wavelength is long compared with the film thickness, the effects of the film are small compared with those of the substrate. On the other hand, when the wavelength is short compared with the film thickness, the substrate has a small effect on the modes and the mode velocities approach the intrinsic transverse velocity of the film. There are many Rayleigh modes which can propagate on a layered medium and for a given system, the number of possible modes

48
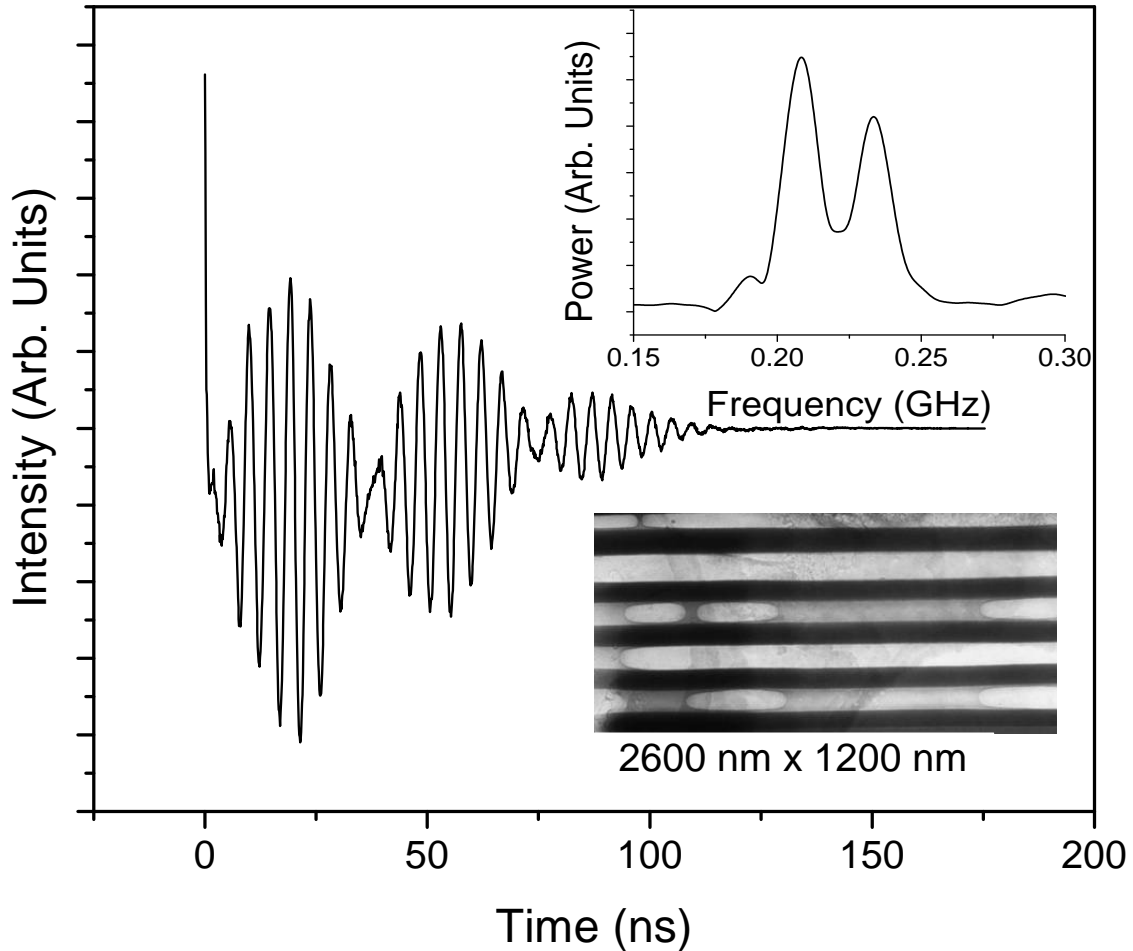
Figure 2-7: Diffracted ISTS signal from PMMA-TiO$_2$ multilayer film sandwiched between gold and glass at 12 μm acoustic wavelength. The top inset shows the power spectrum (i.e., Fourier transform of the diffracted ISTS signal) and clearly illustrates the presence of two thin-film acoustic waveguide modes. The bottom inset shows a transmission electron microscope (TEM) image of the PMMA-TiO$_2$ multilayer film cross section prepared by a focused ion beam (FIB) with the scale shown. There are five alternating layers of TiO$_2$ (darker layers) and PMMA (brighter layers) with individual PMMA and TiO$_2$ thicknesses of 135 nm and 110 nm respectively. The sample assembly is depicted in Figure 2-6.
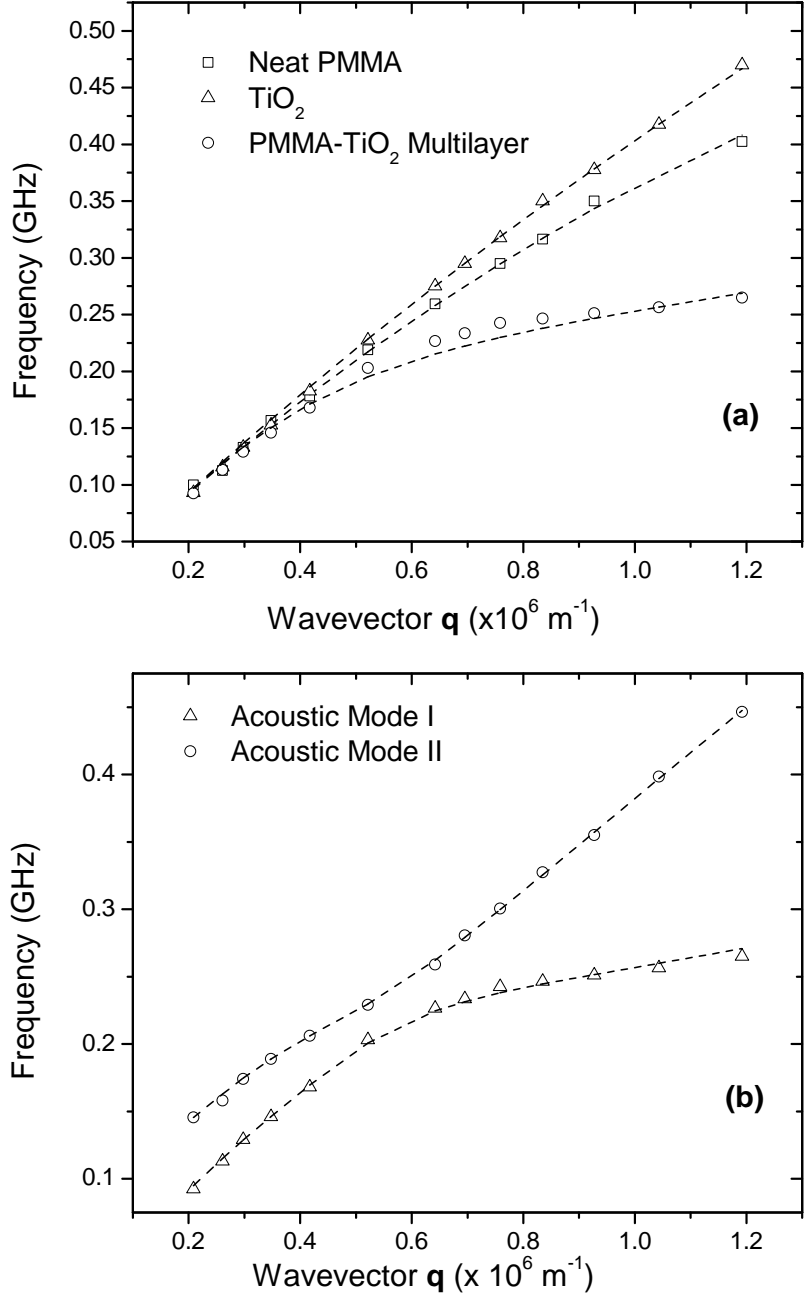
Figure 2-8: (a) Lowest-order acoustic waveguide mode frequency dispersion curves of neat PMMA, TiO_2, and PMMA-TiO_2 multilayer structure. The dashed lines show numerical simulations from which dynamic mechanical parameters were determined. (b) Acoustic waveguide mode frequency dispersion curves of PMMA-TiO_2 multilayer structure. The dashed lines show numerical simulations from which dynamic mechanical "effective"parameters for the multilayer structure were determined, assuming it was one uniform layer. Note the avoided crossing (near $q \sim 0.55 \times 10^6$ m^{-1}) which indicates coupling between the acoustic waveguide modes.

depends only on the product of the acoustic wavevector and the thickness of the film layer, i.e. on the ratio between the acoustic wavelength and the layer thickness.

Numerical simulation of the lowest-order acoustic waveguide mode frequency dispersion curve was performed to extract the physical parameters of PMMA and TiO_2 nanoparticle layers that are indicated in Table 2.1. The uncertainties of the multi-parameter fitting were also estimated by iteratively changing and fixing individual parameters such as layer thicknesses, densities, longitudinal and transverse acoustic velocities, and letting the other parameters vary to optimize the fit. When acceptable fits could no longer be reached by varying the other parameters, the fixed parameter was deemed to be outside of its uncertainty window. More than 5% variation in any of the fitted parameters resulted in a serious deterioration of the quality of the fit to the experimentally observed values. The upper bound on the overall uncertainties of the extracted parameters was estimated to be 5%.

Table 2.1: Mechanical properties of PMMA, TiO_2, and PMMA-TiO_2 multilayer structure, extracted from the recorded acoustic dispersion curves shown in Figure 2-8 using ISTS technique.

Material System	Density [g/cm^3]	Young's Modulus [GPa]	Bulk Modulus [GPa]	Shear Modulus [GPa]	Poisson's Ratio
PMMA	1.1	4.9	4.3	1.9	0.31
TiO_2	3.6	210	150	80	0.27
PMMA-TiO_2^*	2.2	12	12	4.6	0.33

*Averaged or "effective" properties are given for the multilayer structure, determined by assuming it was a single uniform layer.

The results of our fits are in good agreement with values for the bulk materials found in literature [41, 42]. The elastic parameters for TiO_2 nanoparticles encapsulated in organic surfactant are in proportion to the weight fraction of TiO_2 ($\sim$ 90-95 wt%) in the matrix. The results suggest that the equivalent parallel spring model works well for this system of aggregated nanoparticles [43]. The dispersion curve of the multilayer structure PMMA-TiO_2 has been simulated quantitatively with the parameters extracted from the neat samples. The acoustic phase velocity values,
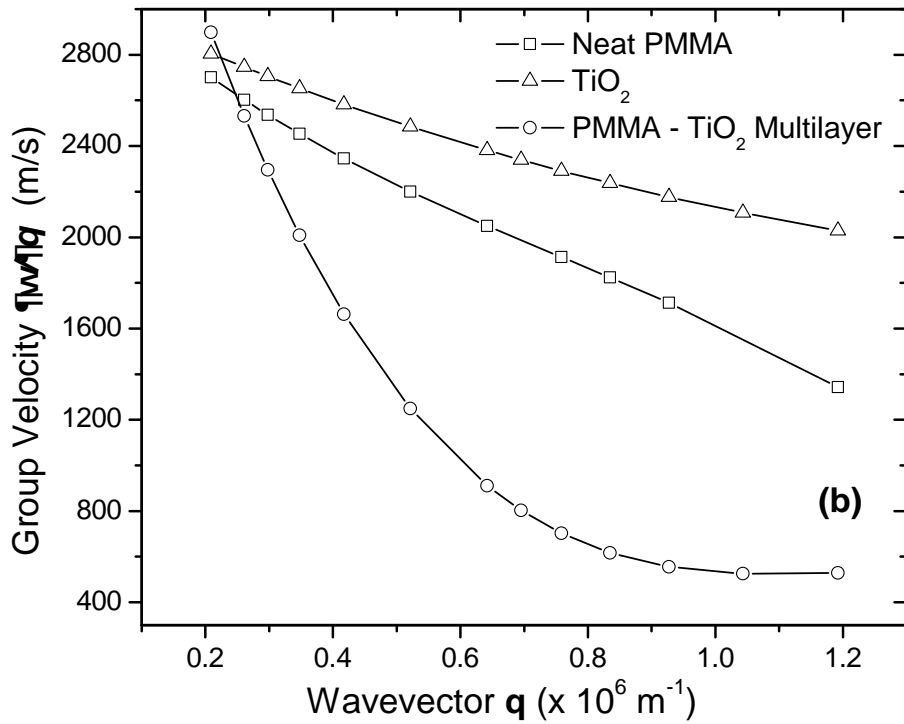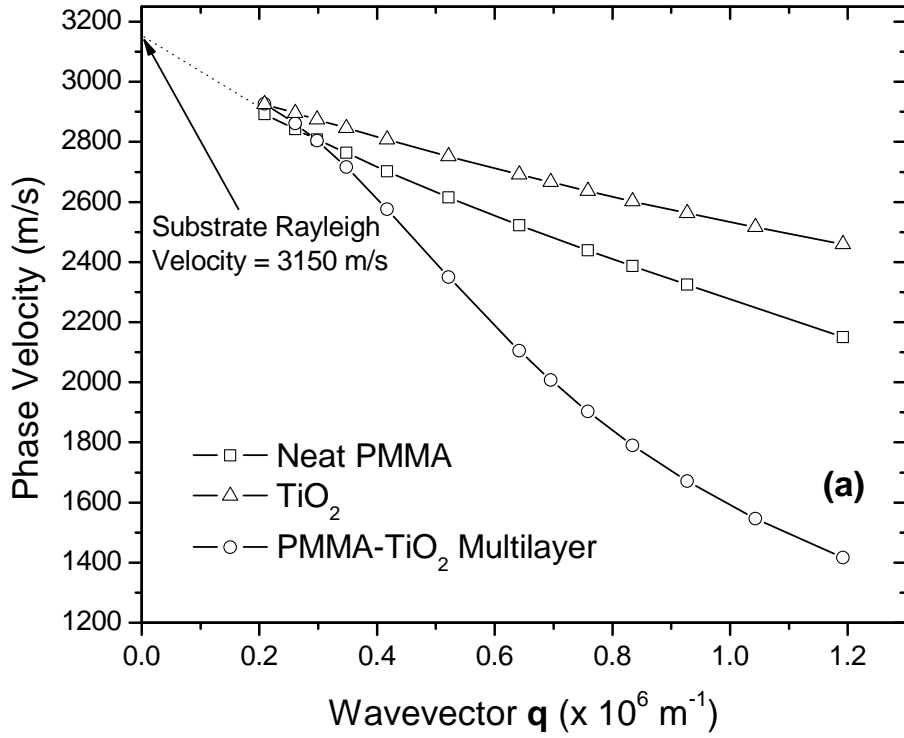
Figure 2-9: (a) Acoustic phase velocity dispersion curves of PMMA, TiO$_2$, and PMMA-TiO$_2$ multilayer structure. (b) Acoustic group velocity dispersion curves of PMMA, TiO$_2$, and PMMA-TiO$_2$ multilayer structure. Note the near-zero group velocity of the multilayer structure in the high wavevector range. Phase velocity $v_p = \frac{\omega}{q}$ and group velocity $v_g = \frac{\partial \omega}{\partial q}$.

which are lower than those of either constituent, are well reproduced. If the multi-layer structure is modeled as a single equivalent layer, this layer has modulus values in quantitative agreement with the simplest formula for an equivalent series spring system [43]. As expected, the modulus of the equivalent layer lies closer to that of the softer material (PMMA) than the harder one (TiO_2 nanoparticles).

The phase velocity dispersion curves for the three samples, along with limiting values for the substrate and the bulk materials, are shown in Figure 2-9 (a). The qualitative trends are as expected, namely higher velocities, approaching that of the substrate, at smaller wave vectors in which the correspondingly longer acoustic wavelengths extend farther into the substrate and more closely reflect the substrate properties. In each case, the shortest acoustic wavelengths are still longer than the film thickness d; that is, I am always in the $qd \ll 1$ regime and so the bulk values that would be reached in the limit of very short wavelength are never approached closely, but the trend is toward these values as wavevector is increased.

Figure 2-9 (b) shows the group velocity dispersion curves of PMMA, TiO_2 and PMMA-TiO_2 multilayer structure. Of particular interest is the result for the multilayer sample, in which the group velocity is extremely low in the range of higher acoustic wave vectors. This means that the speed of acoustic energy transport in the plane of the multilayer film is unusually slow at these wave vectors. This may have useful implications for dissipative structures since slow speeds offer longer times for damping to occur. In this structure, the low group velocity appears to arise from an avoided crossing between the two lowest-order acoustic waveguide modes. More generally, acoustic band gap structures might be constructed that would exhibit similar properties in all directions in selected wavevector ranges.

2.7.2   Ceramic Materials

ISTS measurements on ceramics were conducted to verify that the results could be compared reliably to ultrasonics results. This is important for anticipated work on ceramics under static or dynamic high-pressure conditions, in which non-contact measurements are highly advantageous. Typical diffracted ISTS signal from alu-
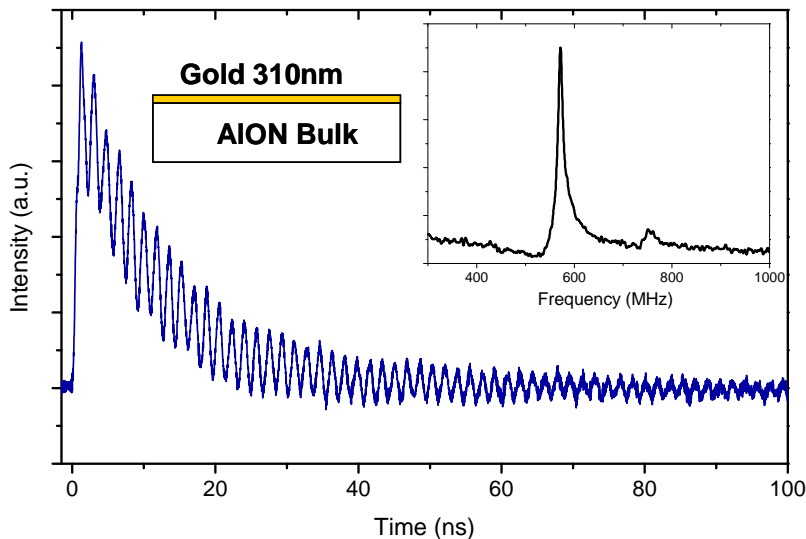
Figure 2-10: Diffracted ISTS signal in reflection mode from an aluminum oxynitride disc with an overlayer of 310 nm thick gold at 6.6 μm acoustic wavelength. The top right inset shows the power spectrum (i.e., Fourier transform of the diffracted ISTS signal) and clearly illustrates the presence of two acoustic waveguide modes. The top left inset show a depiction of the sample assembly (not to scale).

minum oxynitride (AlON) is shown in Figure 2-10. The acoustic response consisting of counter-propagating waves gives rise to damped oscillatory material motion on a nanosecond time scale and the thermal response gives rise to quasi-steady-state signal which persists until thermal diffusion washes out the temperature grating, usually on many nanoseconds or microsecond time scales. The oscillations are associated with acoustic standing waves. The oscillation frequency depends upon the material's acoustic velocity and the decay rate depends upon the acoustic attenuation rate as discussed earlier.

The acoustic dispersion curves are generated for both AlON and boron carbide as shown in Figure 2-11. I also performed ISTS measurements on AlON in transmission mode (as shown in inset of bottom Figure 2-11). The data interpretation is much simpler as only bulk longitudinal modes are excited and hence, I can directly measure the longitudinal acoustic speed from the slope of the dispersion curve. The average longitudinal acoustic speed calculated for AlON is 10.5 km/s.

The acoustic waveguide mode frequency dispersion curves for AlON and boron carbide were used to extract the physical parameters of these ceramic materials, as
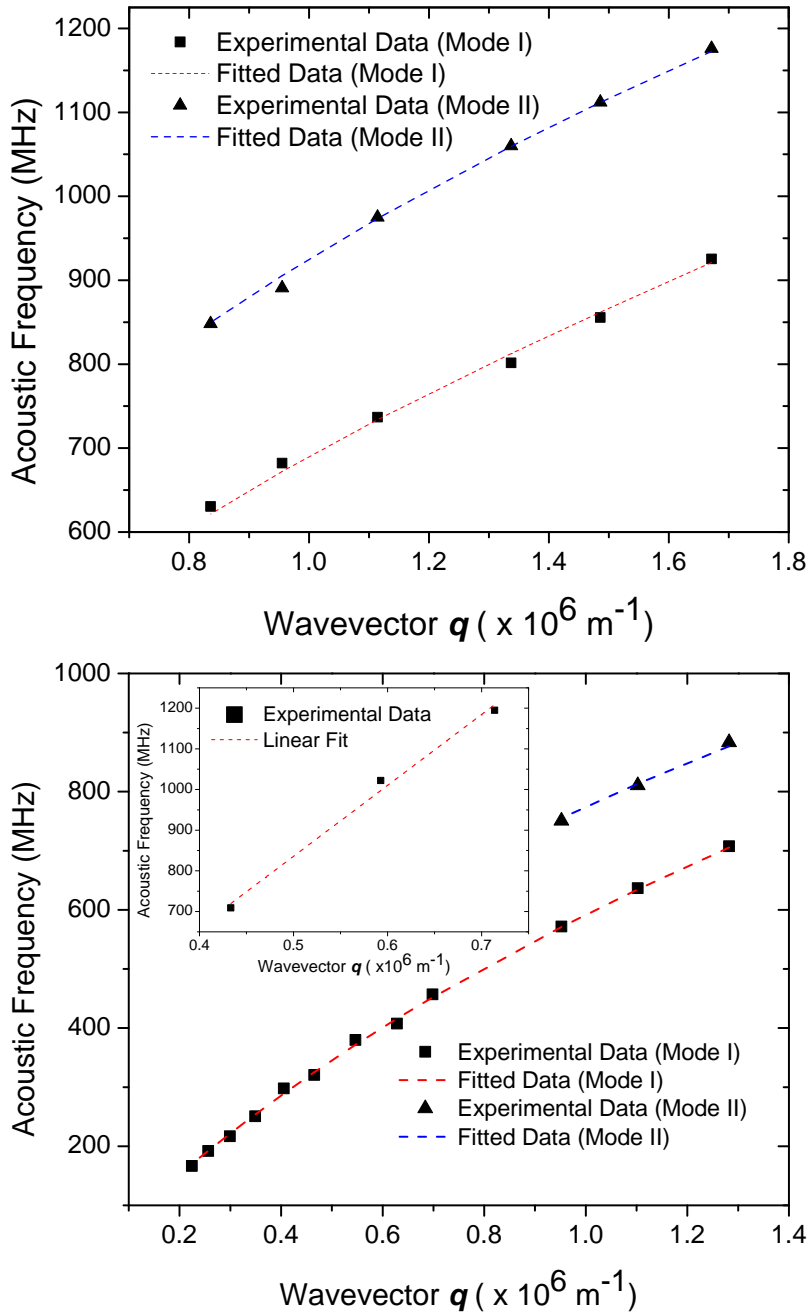
Figure 2-11: Acoustic dispersion curves of boron carbide (Top) and aluminum oxynitride (Bottom) generated from ISTS experiment in reflection mode. The dashed lines show numerical simulations through which mechanical parameters are determined. The inset in the bottom figure shows the acoustic dispersion curve for aluminum oxynitride from ISTS experiments in transmission mode on the same sample without the gold overlayer. The longitudinal acoustic speed is 10.5 ± 0.3 km/s, directly given by the slope of the linear regression curve.

indicated in Table 2.2. The calculated values of acoustic and mechanical properties agree well with the ultrasonic wave velocity measurements done at Army Research Laboratory, Aberdeen [44].

Table 2.2: Acoustic and mechanical properties of aluminum oxynitride and boron carbide computed by modeling the experimental ISTS data obtained in generating the acoustic dispersion curves shown in Figure 2-11.

Material System	Density [g/cm^3]	Longitudinal Speed [km/s]	Transverse Speed [km/s]	Young's Modulus [GPa]	Shear Modulus [GPa]
AlON	3.7	10.7	5.5	295	110
AlON*	3.7	10.3	5.9	320	130
Boron Carbide	2.5	13.8	8.4	430	180
Boron Carbide*	2.5	13.5	8.6	430	185

*Ultrasonic wave velocity measurements done at Army Research Laboratory, Aberdeen in 2001.

2.7.3   Polymer Films

Polyimide Films

One way to check the independence of elastic properties on thickness for a particular material and fabrication method is the analysis of dispersion relations for films of variable thickness, as demonstrated for polyimide free-standing films studied by ISTS technique [45]. Six BPDA-PDA coatings with thickness in the 0.1 to 0.75 m range (less than 1 μm characteristic size) were examined in the transmission geometry, using polarized and depolarized BLS measurements [6], and the observed modes were combined into the dispersion diagram shown in Figure 2-12. The probed waveguide modes possess mixed polarization; that is, they have displacement fields in the sagittal plane. As a result, their phase velocities were functions of both the in-plane and out-plane shear and longitudinal moduli. Therefore, for the particular case of BPDA-PDA polyimides, which are known to possess transverse isotropic symmetry (the in-plane mechanical properties are different from the out-of-plane ones), the dispersion relation

can be completely described by five parameters (ρ, $v_l^\parallel$, $v_t^\parallel$, $v_l^\perp$, and $v_t^\perp$). Lower indices l and t denote longitudinal and transverse polarizations, respectively and upper indices $\parallel$ and $\perp$ denote in-plane and out-of-plane directed excitations, respectively.

Polarized and depolarized BLS measurements [6] showed that Brillouin shift of a mode is proportional to wavevector, q, and does not depend on film thickness. This trivial behavior is demonstrated in Figure 2-13 for a 20 μm thick BPDA-PDA coating for all four combinations of geometry and polarization. Mechanical anisotropy is clearly seen as the difference in the slope (proportional to phase velocity) of linear $\omega(q)$ functions obtained for orthogonal directions for both longitudinal and shear excitations. 20 μm is much thicker than the acoustic wavelengths at these BLS wavevectors, so bulk behavior, with the acoustic frequencies independent of film thickness in this range, is expected.

Table 2.3: Sound velocities and mechanical properties for BPDA-PDA coatings.*

Wave	In-plane	Out-of-plane
Longitudinal	$v_l^\parallel = 3560$ m/s	$v_l^\perp = 2340$ m/s
	$c_{11} = 17.7$ GPa	$c_{33} = 7.67$ GPa
Shear	$v_t^\parallel = 1710$ m/s	$v_t^\perp = 1140$ m/s
	$c_{66} = 4.09$ GPa	$c_{44} = 1.82$ GPa

*Relative error is $\pm 1.5\%$.

Table 2.3 presents sound velocities calculated from the slopes of the Figure 2-13 plots; standard deviation of the values does not exceed 1.5%, assessed by letting parameters vary and seeing how much that changed the fits, just like with the other samples. Previous study of elastic properties of BPDA-PDA at hypersonic frequencies was performed by the ISTS technique on free-standing films, reporting $v_l^\parallel = 3580 \pm 150$ m/s, $v_t^\parallel = 2050 \pm 100$ m/s, $v_l^\perp = 2330 \pm 100$ m/s, and $v_t^\perp = 1130 \pm 50$ m/s [11]. All velocities except the in-plane shear speed, $v_t^\parallel$, are in excellent agreement with our measurements.

All model parameters were predetermined: $v_l^\parallel$, $v_t^\parallel$, $v_l^\perp$, and $v_t^\perp$ values for BPDA-PDA coatings were taken from 10 - 20 μm thick film BLS measurements (Table 2.3); BPDA-PDA mass density, ρ, 1.40 g/cm^3 [46]; v_l, v_t, and mass density of the substrate
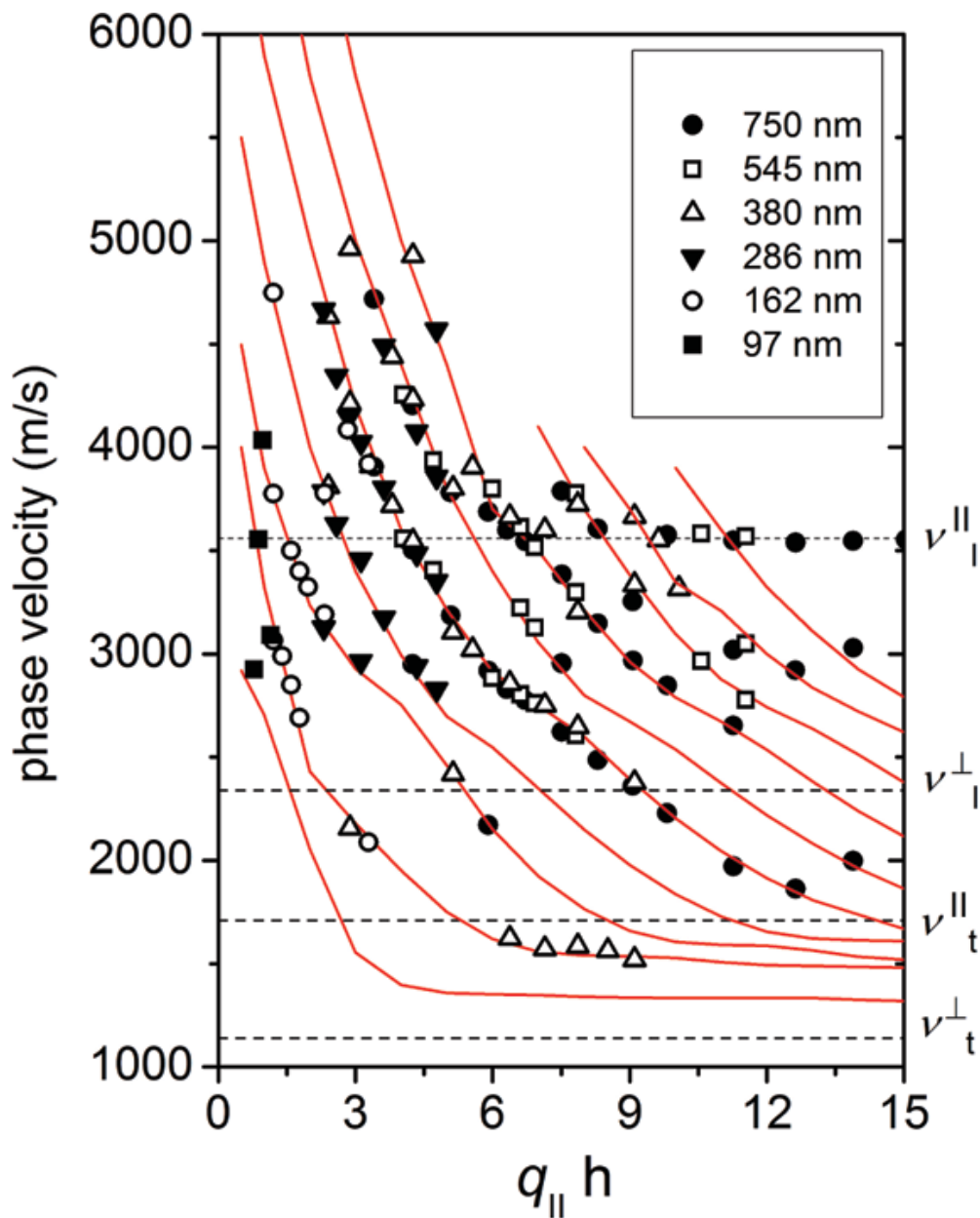
Figure 2-12: Dispersion diagram of the in-plane elastic excitations in supported BPDA-PDA films. The plot contains data for six different thicknesses in the 0.1 to 0.75 μm range and for q in the 0.006 to 0.022 nm^{-1} range. Correspondence between the symbols and the thickness of coating is given in the inset legend. The red solid lines represent the transverse isotropic theoretical model with all model parameters predetermined.
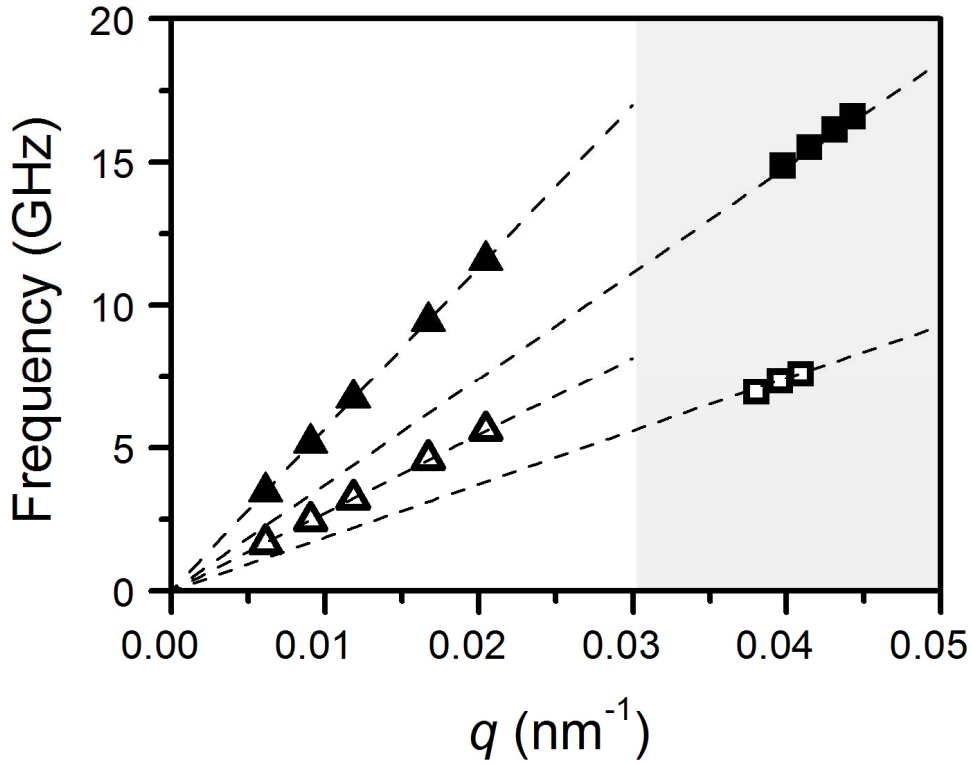
Figure 2-13: Mechanical anisotropy in 20 μm thick BPDA-PDA film. Acoustic phonons propagating with longitudinal (solid symbols) and transverse (open symbols) polarization parallel (triangles) and normal (squares) to the film surface. Figure from reference [6].

were determined beforehand. Tight correspondence of the experimental data and the model for the whole thickness range implies that elastic moduli (and mass density) determined for 10 - 20 μm thick films are valid down to 0.1 μm film thickness; no size effect is observed.

Polystyrene

Typical ISTS signal for a polystyrene thin film is shown in the top curve of Figure 2-14. The wavevector-dependent results and the dispersion relations fit to them are shown in the bottom part of the figure. The results of ISTS characterization of polystyrene yield elastic and shear moduli values of 3.0 GPa and 1.0 GPa respectively with uncertainties of 5%, in close agreement with literature values [47, 48, 49].
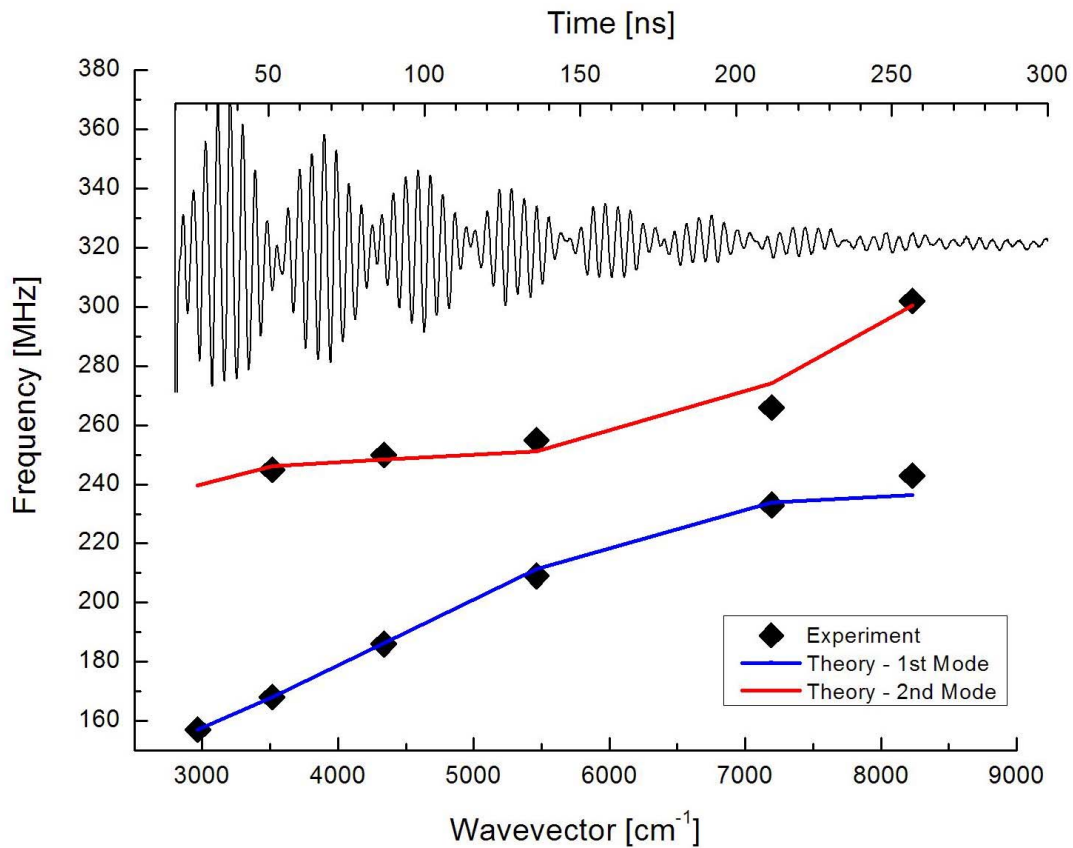
Figure 2-14: Experimentally observed acoustic dispersion relation for 1.270 μm thick polystyrene film on a sapphire substrate with an overlayer of 14 nm gold, along with theoretical calculations. The bottom part of the figure shows observed ISTS signal, where the acoustic wavevector was 7200 cm^{-1} (or 8.727 μm acoustic wavelength) and the Fourier transform of the signal showed two modes at 235 MHz and 265 MHz.

Other Polymer Systems

ISTS measurements were carried out on a variety of polymeric systems in different sample configurations. These measurements were averages of 25 signals recorded from different spots on the samples so that variations in sample properties could be homogenized. This was also done to verify that high-quality ISTS data could be recorded even from samples undergoing irreversible change such as that induced by shock loading. An array of ISTS signal is plotted in Figures 2-15 and 2-16. It should be emphasized that these single-shot measurements are applicable to a very wide range of single-component and composite materials.

2.8 Conclusions

ISTS measurements made on a PMMA-TiO$_2$ multilayer structure suggest that it may serve as a prototype for acoustic bandgap materials or other designs with substantial acoustic impedance mismatch between alternating layers. The lowest-order acoustic waveguide modes have been characterized in samples composed of the individual materials and the multilayer structure in the sub-GHz frequency range. Throughout this range, the acoustic phase velocities in the multilayer sample are lower than those of either of the two components, and the effective modulus values of the multilayer structure lie between those of its constituents. A regime has been observed in which the multilayer structure exhibits extremely low acoustic group velocity in the lowest-order waveguide mode, suggesting possible applications in structures that exploit the slow sound speed for increased dissipation or, at larger amplitudes, improved mitigation of dynamic mechanical impact.

The reasons for studying boron carbide are concerned with the observed loss of shear strength in the material under shock wave compression. It is not clearly understood whether such a change is intrinsic to crystalline boron carbide or is due to the associated amorphization of boron carbide above 25 GPa [50]. Measurements extended to high pressures induced by laser shock would provide the compression curve and the shear strength of boron carbide at high rates of loading and as a function
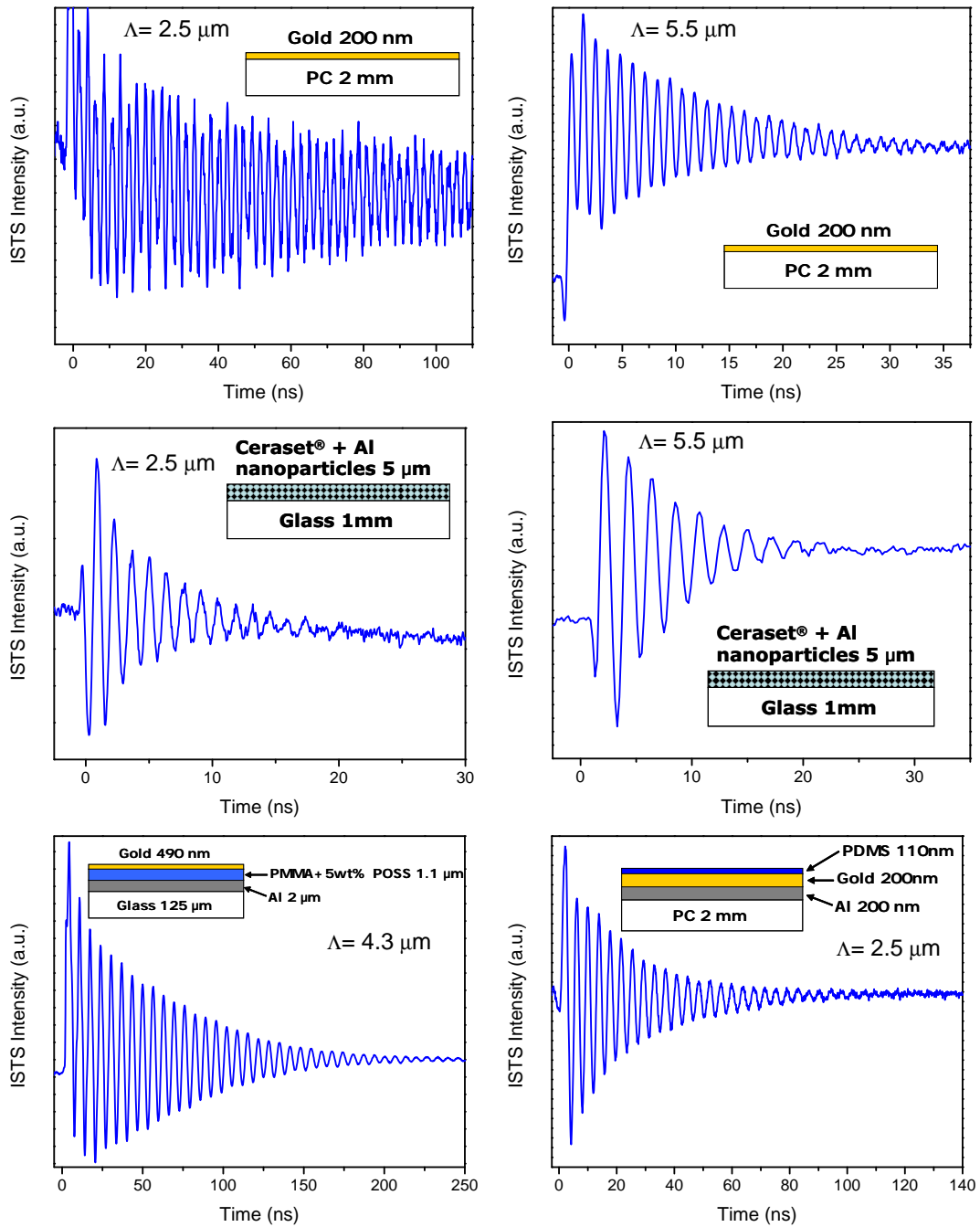
Figure 2-15: Diffracted ISTS signal from variety of polymeric films at different acoustic wavelengths Λ. The inset depicts the sample assembly used in each measurement (not to scale). The frame shows averages of 25 signals recorded from different spots on the sample so as to minimize variation in film properties over a wide region.
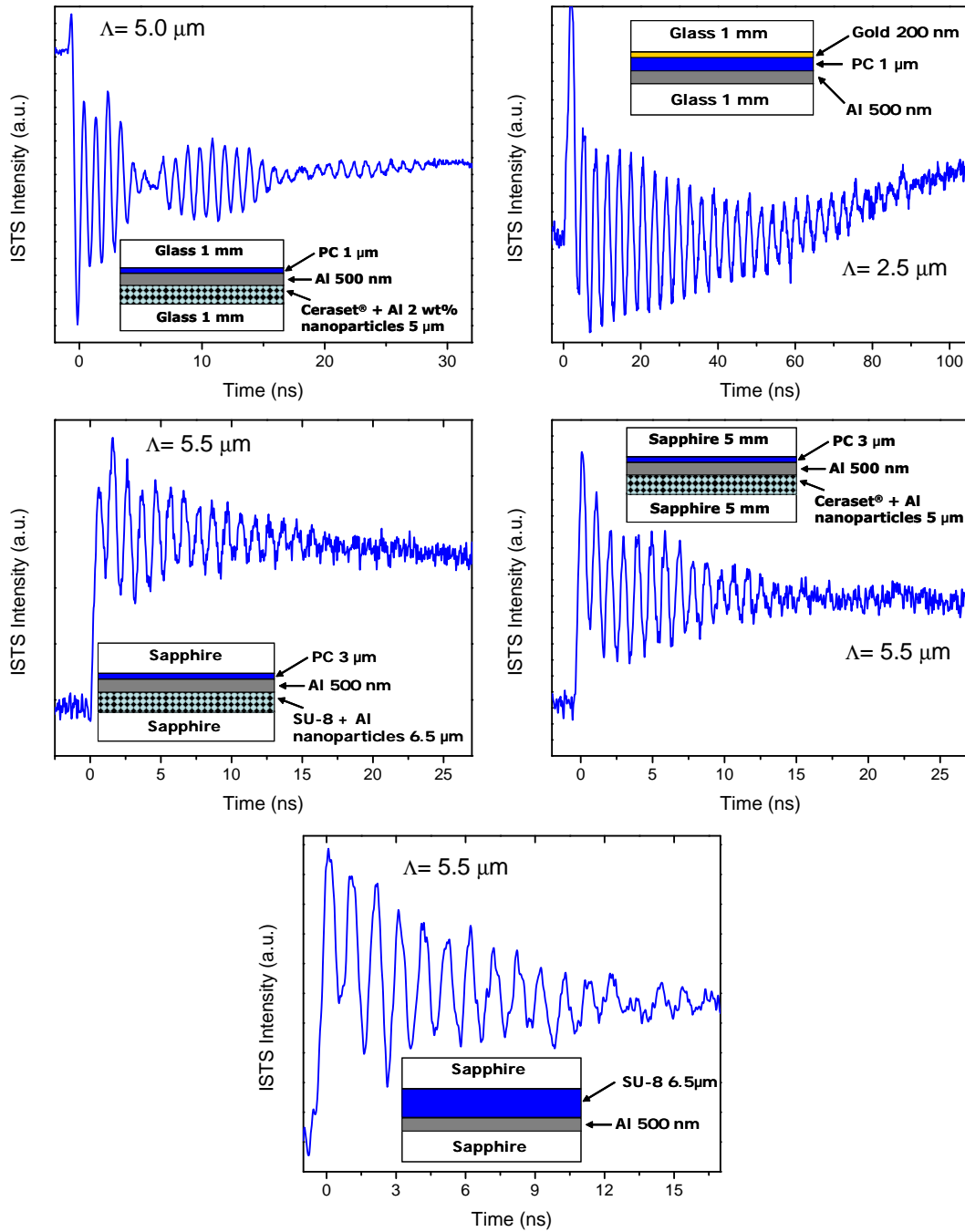
Figure 2-16: Diffracted ISTS signal from variety of polymer systems sandwiched between two thick pieces of glass or sapphire. The inset depicts the sample assembly (not to scale) and the acoustic wavelength Λ of the acoustic waves generated using ISTS pump beams. The data were recorded by moving to a new sample location for each of the 25 shots.

of compression. In the case of aluminum oxynitride, it is hypothesized that phase transition and associated compression plays a significant role under shock induced stress [51].

ISTS measurements on polymer samples yielded reliable material parameters and showed that single-shot signals can be collected from a wide range of materials and in various geometries that are relevant to shock loading measurements. Single-shot ISTS measurements will provide valuable information about the evolution of viscomechanical properties and physical state including phase transitions under extreme conditions.

Chapter 3

Shock Wave Spectroscopy

3.1 Shock Waves

Introduction

When the amplitude of stress waves greatly exceeds the dynamic flow strength of a material, we can effectively neglect the shear stresses, in comparison with the compressive hydrostatic component of the stress. This leads to a high-pressure state (or high-amplitude isentropic disturbance) traveling into a material. The disturbance front will "steepen-up"as it travels through the material because the higher amplitude regions of the front travel faster than the lower amplitude regions. This leads to a *shock wave*, which is defined, ideally, as a discontinuity in pressure, temperature (or internal energy) and density. Thus, shock waves are characterized by a sharp discontinuity in the thermodynamic variables of the material. Shock can result from impact: drop shock, ballistic shock, and automotive crashes or from explosives in the case of pyroshock and blasts. An excellent review on the fundamentals of stress wave phenomena is given by D. B. Hayes [52].

A shock pulse travels through a material at a speed (U_s) approximately equal to the sum of the particle velocity (U_p) and the medium's acoustic velocity (c), i.e., $U_s \approx U_p + c$. The particle velocity is the speed with which the material at the point of interest is moving, the velocity of material flow behind the shock front.
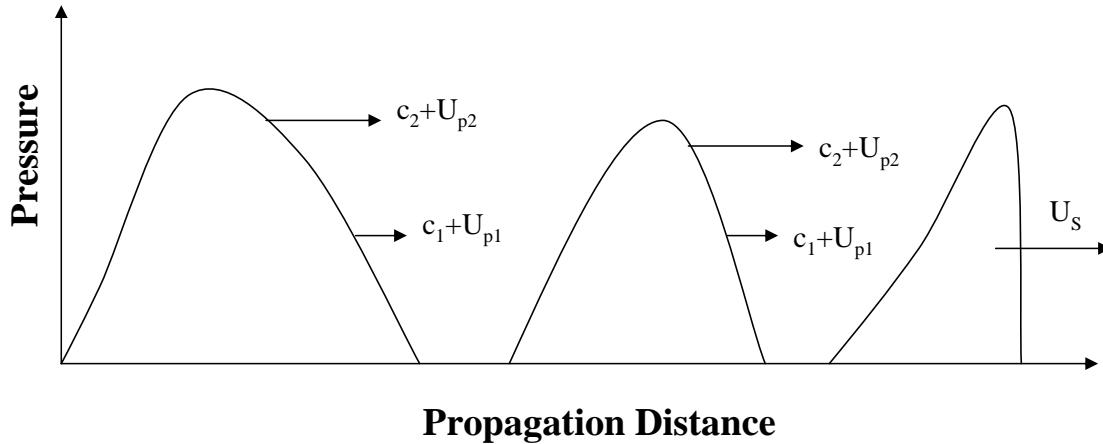
Figure 3-1: Schematic showing the formation of a shock wave in an idealized model. As the disturbance propagates from left to right, the front becomes increasingly steep, until it becomes instantaneous. This implies a discontinuous jump in pressure (and correspondingly, density), as shown to the right. U_s is the shock velocity, U_p is the material velocity and c is the acoustic velocity. Typically, U_s is on the order of several km/s. The subscript 1 and 2 refer to different position on the moving wave front[52].

Accordingly, the shocked region exhibits higher density than unshocked regions. The development of the shock results from a material's property of transmitting sound faster with increasing pressure (or density). The fundamental requirement for the establishment of a shock wave is that the velocity of the pulse (U_s) increases with increasing pressure (P). As shown in Figure 3-1, a high-pressure trailing shock edge will steepen because higher-pressure shocks travel faster. Thus a compressional wave will continue to propagate faster until its front exhibits a discontinuous jump in pressure – the formation of a shock.

The intense compression the shock induces is followed by recoil or rarefaction, which is rapid expansion of the material. Just as conventional high-rate testing techniques (e.g. split-Hopkinson pressure bar and gas gun testing), laser-induced shock loading is a thermodynamically irreversible adiabatic process because the compression is nearly instantaneous, accompanied by an entropy increase [53]. Typical shock velocities are in the range of 4 - 9 km/s. Compression can be up to 20% in some cases, with an associated temperature rise of hundreds of degrees – all within tens of picoseconds. After the shock passes, cooling occurs at a fantastic rate of few hundred
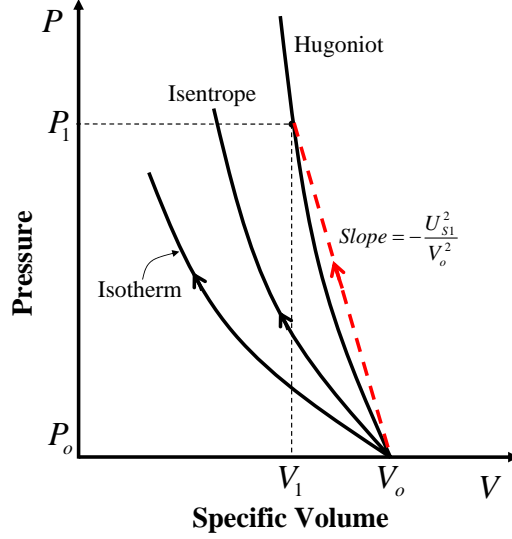
Figure 3-2: Pressure-volume compression curve for the passage of the shock wave through a material. For isentrope and isotherm, the thermodynamic path coincides with the locus of states. For shock, the thermodynamic path is a straight line, Rayleigh line (shown in dotted red color) to point (P_1, V_1) on the Hugoniot curve, which is the locus of available shock states, not a shocking path [55]. Note: $V_0 = \frac{1}{\rho_0}$ and $V_1 = \frac{1}{\rho_1}$.

billion degrees per second in the case of single-stage shock compression [54]. In a typical polymer (e.g., PMMA), shock volume compression is around 20% under peak pressure of 4.5 GPa, shock velocity is 4 km/s, and temperature rise is 125 Kelvin.

A pressure-volume (P-V) diagram is directly measured during a conventional shock experiment. A typical P-V compression curve is shown in Figure 3-2, along with the thermodynamic path for a shock. The quantitative relationship which governs the behavior of shock waves is derived by using the Rankine-Hugoniot equations. Given 1-D steady flow of a compressible, inviscid (non-viscous) fluid, the following equivalent expressions of conservation of mass, momentum, and energy all apply:

$$\rho_1 = \rho_0 \left(1 - \frac{U_p}{U_s} \right)^{-1} \tag{3.1}$$

$$P_1 - P_0 = \rho_0 \, U_s \, U_p \tag{3.2}$$

$$E_1 - E_0 = \frac{1}{2}(P_1 + P_0) \left(\frac{1}{\rho_0} - \frac{1}{\rho_1} \right) \tag{3.3}$$

where ρ is density, U is speed, P is pressure, E is internal energy per unit mass, and

the subscripts 0 and 1 indicate initial (unshocked) and final (shocked) conditions, respectively.

In the above conservation equations (3.1)–(3.3), there are five variables: pressure (P_1), particle velocity (U_p), shock velocity (U_s), density (ρ_1), and energy (E_1). Hence, an additional equation is needed if we want to determine all parameters as a function of one of them. This equation can be expressed as the relationship between shock and particle velocities, and has to be experimentally determined.

$$U_s = c + S_1 \, U_p \tag{3.4}$$

where c is the acoustic velocity in the material at zero pressure and S_1 is an empirical parameter. For most materials not undergoing phase transitions, Equation (3.4) is valid and a linear relationship describes fairly well the shock response of materials. The free-surface velocity, U_{fs}, is twice the particle velocity of the shock pulse, U_p, and can be determined by laser interferometry [56]. This allows determination of all other shock parameters.

The most extreme loads are those that are imposed by high-velocity impact, contact with a detonating explosive charge, or sudden deposition of thermal energy. The material response to these stimuli is formation and propagation of a shock wave, a disturbance that provides access to the highest obtainable rates of deformation. The nature of these loading processes is such that the load is applied only briefly, so the compression produced by the shock is relieved by a following decompression wave.

The loading event is communicated into the interior of the material by a compression pulse propagating at approximately the sound speed in the medium. As is well known, a propagating compression pulse reflects from a stress-free surface as a tensile pulse. In the absence of fracture, this tensile pulse has magnitude and duration similar to those of the incident compression pulse. Under typical experimental conditions, the peak compression stress produced by the loading event falls in the range of 0.1 to 100 GPa (or 10 kbar) and the duration of the compression pulse ranges from a few picoseconds to a few microseconds. Figure 3-3 shows a typical pressure temporal
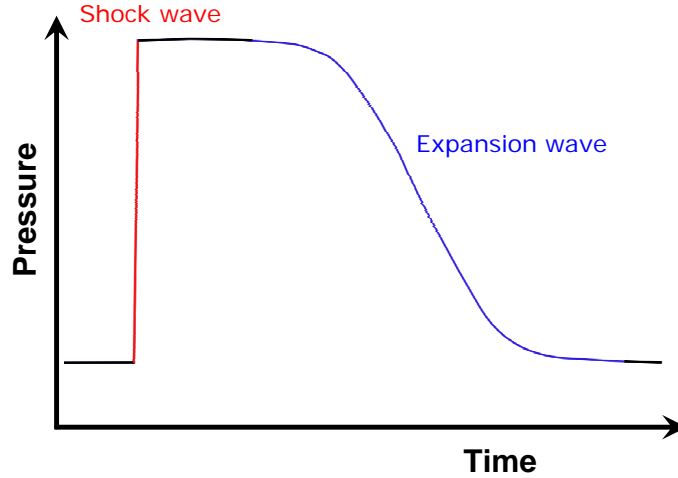
Figure 3-3: Idealized variation in pressure with time behind a shock wave followed by expansion wave. The shock wave leads to an abrupt rise in the pressure, and the duration of the compression pulse ranges from tens of picoseconds to a few nanoseconds (in laser-induced shock loading) to a few microseconds (in projectile or gas-gun generated shock).

profile for a material undergoing shock loading. Because of the very large amplitude of these pulses, the tensile stresses that arise upon reflection can easily exceed the strength of even the strongest materials. The rate at which this tension develops is dependent on both the loading conditions and the properties of the material, but it is usually higher than tensile loading rates obtainable by other means.

Zeldovich applied the theory of non-steady spherical shock waves for studying detonation waves generated during explosion of a charge [57]. As the radius R of the shock front increases, the front slows down and the pressure P drops according to the following relation:

$$R(t) = \kappa \ E^{1/5} \ t^{2/5} \tag{3.5}$$

$$P(t) = \kappa' \ E^{2/5} \ t^{-6/5} \tag{3.6}$$

where E is the fixed amount of energy released during explosion or detonation. The constants κ and κ' depend on the fraction of energy converted to work and heat and are functions of the bulk Grüneisen parameter for a condensed material.

3.2 High Strain Rate Measurements

Polymeric materials are known to exhibit strongly time-dependent mechanical be-
havior, as evidenced by rate-dependent elastic moduli, yield strengths, and post-yield
behavior. The ability to tailor molecular-level mechanics through the incorporation
of nano-scale particles offers new opportunities to design polymer-based material sys-
tems with different behaviors (elastic, yield, post-yield) in different frequency or rate
regimes.

The measurement of dynamic properties of materials under extreme ranges of test
conditions requires use of specialized and often sophisticated equipment and tech-
niques to obtain satisfactory data. A variety of test methods have been employed for
studying the strain rate behavior of polymers. Table 3.1 shows typical values of strain
rates observed under various loading conditions. The split-Hopkinson pressure bar
(SHPB) is still the primary method for testing the mechanical properties of materials
in homogeneous deformation at high rates of strain.

Table 3.1: Typical values of strain rates observed under various conditions.

Method	Strain Rate $[\mathbf{s}^{-1}]$
Instron	10^{-1}
Drop-weight	10^{2}
Split–Hopkinson pressure bar	10^{3}
Blast/Explosion	10^{5}
Gas gun/Bullet/Flyer plate	10^{6}
Laser–induced shock	10^{8}

It has been suggested that a polymer's macroscopic mechanical response to a
general loading case is governed by its ability to access various primary and secondary
molecular mobilities [58]. The primary process or α-relaxation is associated with
the cooperative segmental motion of approximately 20 to 40 monomers of the main
polymeric chain. It is also known as the glass-rubber transition temperature or simply
the glass transition (T_g). The secondary process or β-relaxation is associated with
rotation or local motion of side groups stemming from the main chain [59]. The

70
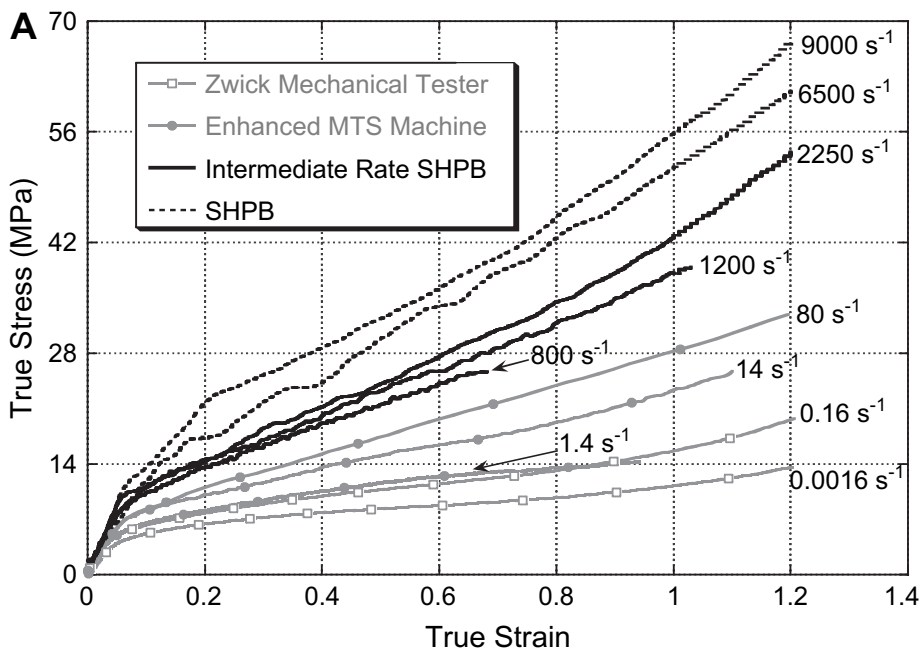
Figure 3-4: Uniaxial compression stress–strain behavior of polyurea at strain rates ranging from $10^{-3}\,\mathrm{s}^{-1}$ to 9000 s^{-1} (each split-Hopkinson pressure bar (SHPB) curve is labeled by its true strain rate at a true strain of 0.60 [60].

rotation of the entire side group about the main chain normally takes place at a higher temperature and at a slower rate (or longer relaxation timescale) than the rotation of a small side group or a portion of the group. Specifically, under conditions of high strain rate, restricted secondary molecular motions are thought to bring about enhanced stiffness and strength. The stress-strain behavior of polymers is strongly dependent upon the strain rate. As the strain rate is increased, both the initial elastic modulus and the stress level required for plastic flow increase. The true stress-true strain curves for polyurea at room temperature over seven decades of strain rate are presented in Figure 3-4 [60]. The temperature dependence of the mechanical behavior of amorphous polymers is also very closely linked to the strain rate dependence.

It is well known that the viscoelastic behavior of any glassy, amorphous polymer is governed by multiple activated processes [61]. These different activated processes generally correspond to different segmental motions of the macromolecules. When a particular segmental motion becomes restricted, the corresponding process will require stress-assisted activation, and thus the polymer's viscoelastic behavior passes

71
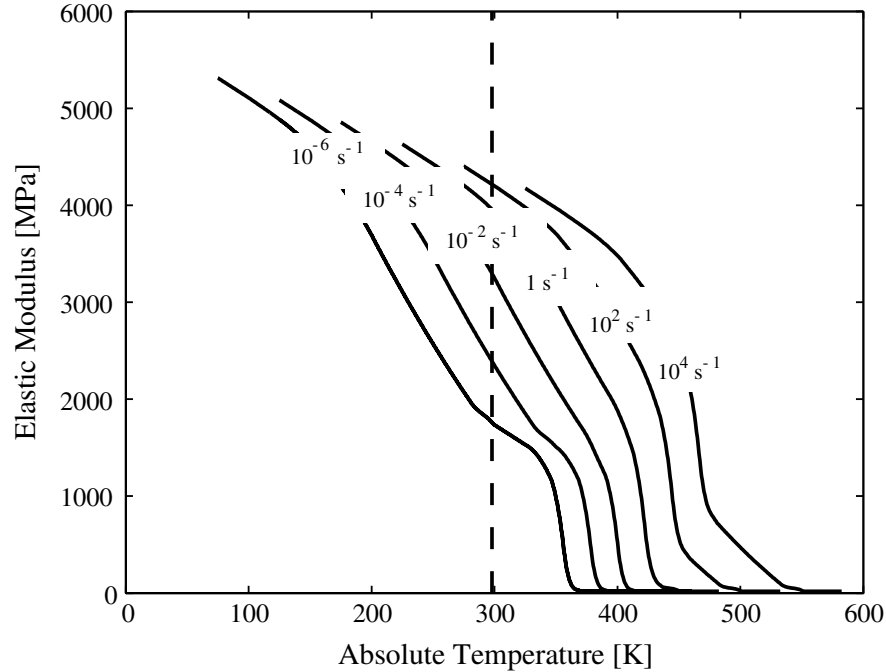
Figure 3-5: Model prediction of the PMMA elastic modulus curve at six different strain rates, ranging from $10^{-6}\,\mathrm{s}^{-1}$ to $10^4\,\mathrm{s}^{-1}$ [58]. The vertical dashed line represents room temperature (298 K).

through a transition as a function of stress. As is now understood, these restricted motions also cause transitions in the rate-dependent yield behavior of many amorphous polymers. However, in that case, it is not as easy to deconvolute the contributions from different processes.

Figure 3-5 shows the decompose–shift–reconstruct (DSR) model prediction of the PMMA elastic modulus curve at six different strain rates, ranging from $10^{-6}\,\mathrm{s}^{-1}$ to $10^4\,\mathrm{s}^{-1}$. The curve not only shifts to the right (increased temperatures) with increasing strain rate, but it also changes shape due to the different shift factors for α and β transitions [58].

3.3   Shock Wave Spectroscopy

Shock waves allow us to study fast structural evolution processes in the higher energy regions of the energy landscape difficult or impossible to access by conventional techniques. This section reviews work done on generating shock by various techniques as well as different kinds of tools being used for shock measurement. It presents studies done using a gas gun to generate shock on one hand and laser-induced shock loading on the other. Also, different measurement techniques of probing material under shock loading like Raman scattering, fluorescence spectroscopy, infrared spectroscopy, and coherent anti-Stokes Raman scattering (CARS) have been discussed.

It is convenient to classify experimental devices according to the energy source used to drive shock loads [62] -

1. Gun type launchers like powder guns, light-gas guns and ballistic shock tubes

2. Explosive systems based on powerful condensed high explosives

3. Electric and electromagnetic guns

4. Devices using radiation sources like lasers, x-rays, etc.

There are various spectroscopies being used as probes of material response to shock. The time resolution in most time-resolved spectroscopy is limited by the optical instrumentation, either the pulse or the detector. In shock wave spectroscopy, time resolution is limited by the instrumentation as well as the time needed for the shock to traverse the part of the sample that is monitored by the probe pulse, which depends on many parameters including the probe absorption strength.

The primary methods of shock generation are mechanical or projectile-impact shock loading and laser-induced shock loading [63]. The two realms of shock loading are similar in principle since laser shocking drives a thin film of aluminum serving as a battery ram. The major difference between the two approaches is the duration of the shock pulse. Laser-initiated shocks usually do not last longer than several nanoseconds, whereas mechanical shocking leaves the sample in a constant pressure steady state for microseconds. Because the ensuing stress states last for different lengths

of time in laser-induced and gas gun shocking, the timescale over which material behavior is probed is different [64].

3.3.1   Gas Gun Spectroscopy

A gas gun is a projectile-firing gun powered by compressed air. Gupta et al. have studied the impact responses of polymers such as polymethyl methacrylate (PMMA) under gas gun loading [65], measuring mechanical parameters similar to those in impulsive stimulated thermal scattering (ISTS) measurements but under shock loading. Large amplitude one-dimensional compression and shear wave measurements were made, and shear and longitudinal wave velocities were used to determine the shear modulus, bulk modulus, and mean stress-volume relations under impact loading using wave velocity analysis. The reported longitudinal particle velocities, compressional velocities and shear wave velocities on the microsecond timescale are shown in Table 3.2. Clearly, there is an increased wave propagation speed and transient density compared to the acoustically measured value of $2.83\,\mathrm{km/s}$ for unshocked PMMA [4]. These extremely difficult measurements have not been repeated on any material since this 1981 study. However, experiments have been done to probe acoustic properties using ISTS detection under gas gun shock loading in liquid benzene shocked to nearly 1 GPa [66].

Table 3.2: Experimental values for PMMA under gas gun shock loading [65].

Longitudinal Particle Velocity [km/s]	ρ_1/ρ_0	$c_{\mathrm{compression}}$ [km/s]	c_{shear} [km/s]
0.00	1.00	2.83	1.10
0.13	1.04	3.31	1.48
0.18	1.06	3.40	1.51
0.22	1.07	3.45	1.52
0.27	1.09	3.61	1.51

3.3.2 Laser Shock Spectroscopy

Laser ablation has a wide range of technological and practical applications in micro-fabrication, surface treatment of polymer thin films, vaporization of refractory or nonvolatile materials for chemical synthesis or analysis, and surgical ablation of hard and soft tissues. The broad areas for investigation include time and space-dependent optical properties of materials under intense laser irradiation, the nature of very fast decomposition reactions in complex materials such as polymers or bio-polymers; and physical properties such as viscosity, acoustic velocities, heat capacity, tensile strength, cohesion, adhesion, etc., of materials under the extreme conditions induced by ablation [67].

3.3.2.1 Laser Shock Generation

Laser generated "nanoshocks"allow controlled, high repetition rate, time-resolved examination of dynamic high-pressure physical phenomena on small spatial scales. Shock waves are generated in thin metal films using frustrated laser ablation. The sample for creating the shock waves usually consists of thin metal films deposited on dielectric substrates, most commonly aluminum on thick amorphous glass or crystalline sapphire cover slips. Typically, a femtosecond or picosecond laser pulse is focused through the dielectric substrate onto the metal film, where the laser energy heats the electrons in the skin depth of the metal, and the hot electrons travel ballistically through the cold metal lattice to approximately the electron-phonon coupling length of the metal [68]. The thermal energy in the electrons is coupled into the metal lattice via electron-phonon interactions, heating the metal lattice, which expand in response to the temperature jump to create the shock wave in the metal. The dielectric substrate act as a tamper, preventing rapid expansion of the material back toward the incident laser pulse and forcing the expansion into the metal film.

The four key steps in the frustrated laser ablation method of shock wave generation in thin metal films are -

1. Laser pulse focusing and absorbtion through a dielectric substrate onto the metal film, heating electrons in the material to a temperature of 100 - 1000 eV

creating a hot electron gas.

2. The hot electron gas traveling through the material to the electron-phonon coupling length.

3. The energy transferring from the electrons to the metal lattice.

4. A supersonic heat wave propagating in the bulk of the target material, driven by thermal conduction. The shock wave overtakes the heat wave when the conduction front has slowed down to approximately the sound velocity. In other words, the hot lattice expands to generate a shock wave in the metal film (and in the dielectric substrate).

A long duration of the laser pulse is required to generate a supported shock wave that can travel through several microns of material without being eroded by release waves from the laser heated expansion region. The compressed mechanical pulse creates a shock wave in the same way as the laser pulse; however, since the laser did not continue to drive the shock wave, a release wave is formed behind the shock. The release wave travels faster than the shock wave through the material that is compressed from the shock wave and has a higher sound speed. The release wave overtakes the shock wave, at which point shock propagation ceases.

3.3.2.2 Laser Shock Spectroscopy

Pulsed high irradiance laser induced shock waves are being used for assessing the dynamic mechanical behavior of materials at extreme conditions. There are several research groups that have investigated polymeric materials under laser-induced shock-loading with different experimental techniques. In principle many linear and nonlinear optical techniques can be used to probe the shocked sample. A discussion and brief illustration on several of the approaches used has been presented in this section.

The detailed behavior of molecules and materials under shock compression has been studied using a number of different spectroscopic techniques, including fluorescence (or photoluminescence) (Leung et al. [69]; Lu et al. [70]; Shen and Gupta [71]), absorption (Gruzdkov and Gupta [72]), Raman (Holmes et al. [73]; Kobayashi and

76

Sekine [74]; Nicol et al. [75]; Pangilinan and Gupta [76, 77]), infrared (IR) (Ren-lund et al. [78]) and coherent anti-Stokes Raman Spectroscopy (CARS) (Dlott et al. [53, 54, 79]; Franken et al. [80]; Hambir et al. [81]).

A main problem associated with probing shock fronts is that shock waves moving at a velocity of a few nm/ps are very slow compared to light moving a few hundred μm/ps. The time or spatial resolution in laser-driven shock experiments is ultimately limited by sample thickness (or configuration) or the probe light penetration depth and the laser pulse duration. The resolution cannot be achieved merely by focusing laser pulses tightly because the shock front is much smaller than a wavelength of visible light. In most shock experiments, the time resolution is generally limited by the shock transit time across the sample layer being probed, and hence, samples of nanometer thicknesses are preferred. However, the sample must also be thick enough to yield a detectable ultrafast signal with good signal-to-noise ratio, which is determined by the sensitivity of the apparatus to small signal changes and increases with sample thickness [82].

Because chemical reactions represent drastic changes in electronic structure with corresponding large spectroscopic changes, time-resolved UV-visible absorption experiments were the first to be used to probe shock-induced chemical changes. Time-resolved absorption experiments have been used to probe shock-induced chemical changes in CS_2 by Duvall and co-workers [83].

Infrared spectroscopy has been used to look at reactivity in shocked materials by probing specific vibrational modes [84]. It is sensitive to molecular configurations but provides little if any information about the electronic states of the materials. Reflectivity provides information regarding electronic structure, and the reflectivity of shocked materials has been previously measured, yielding information about the materials electronic changes [85].

Time-resolved Raman scattering has proven valuable in the microscopic character-ization of structural and symmetry changes in the shocked state [86]. Raman work on quartz has emphasized the role of non-hydrostatic stresses on compression and tension at the microscopic level. Time-resolved Raman spectroscopy studies were performed

on benzene derivatives under laser-driven shock compression up to a few GPa using a pump-probe technique, in order to investigate the effects of steric hindrance and chemical structure on the molecular dynamics of shock compression [87]. Under shock compression at 1.3 GPa, the ring-breathing mode of benzene showed a high frequency shift of 10 cm^{-1} which corresponded to a ring reduction of 0.7%. The magnitude of the frequency shift showed a systematic dependence on intermolecular distance; the ring-breathing mode is decreased, while the ring-vibrational is increased, as molecules are forced to come close together. Nanosecond time-resolved Raman spectroscopy is also used to investigate the structure and bond strength of molecules and crystals under shock compression using a pump and probe technique [88]. Polytetrafluoroethylene (PTFE) was studied under laser-driven shock compression at 2.3 GPa (laser power density of 4.0 GW/cm^2). A new vibrational line at 1900 cm^{-1} appeared only under shock compression and was assigned to C=C stretching in transient species produced by shock-induced bond scission.

Dlott et al. used coherent anti-Stokes Raman scattering (CARS) as a probe to study shock wave phenomena [89, 90]. CARS is a form of time-resolved nonlinear vibrational spectroscopy in which a pair of optical fields drives a coherent vibrational response. Shock-induced changes in the selected vibrational frequency can be measured as a function of time. Figure 3-6 shows polycrystalline anthracene CARS spectra near 1400 cm^{-1} before and after shock over a total time duration of 175 ps. The CARS spectra showed that the Raman transition blue-shifts about 16 cm^{-1} and almost doubles in width during shock loading. The shift is mainly a function of density (or pressure) and the width is a function of temperature [81, 91]. Tas et al. have characterized the nanoshock waveform by measuring the shock front rise-time, shock fall-time, peak pressure, and velocity using CARS [92].

Lagutchev et al. have used laser-driven shock waves close to 1 GPa to dynamically compress self-assembled monolayers (SAMs) [93]. They have shown evidence of a complicated viscoelastic response of the materials under shock loading and that the SAM response to shock is dependent on both the molecular structure and on the lattice structure as determined by the metal substrate. In viscoelastic shock compres-
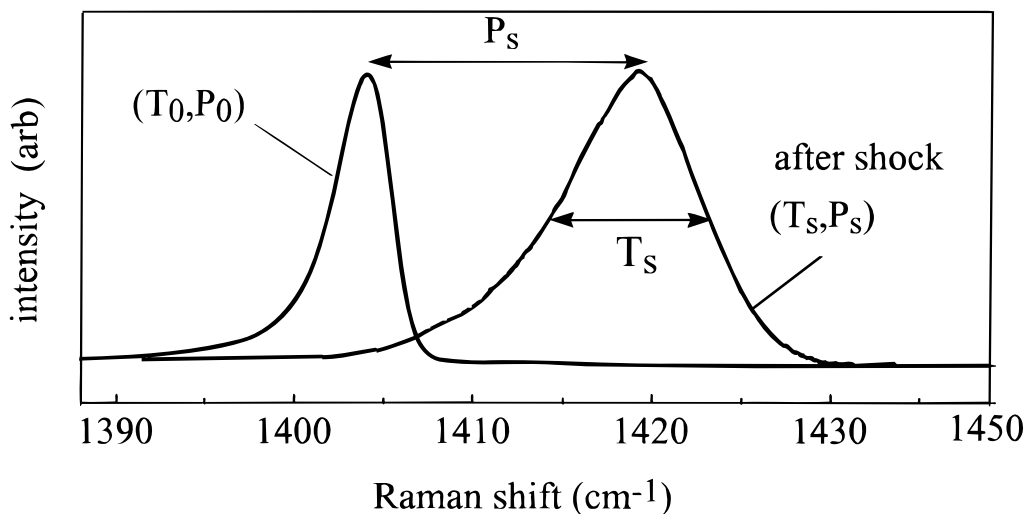
Figure 3-6: Coherent anti-Stokes Raman scattering (CARS) spectrum of a 700-nm layer of polycrystalline anthracene in a micro-fabricated shock target array (optical nanogauge) near 1400 cm^{-1} transition [79, 81]. The frequency shift which happens over a time duration of 175 ps can be used to estimate the shock pressure P_s and the spectral width can be used to estimate the shock temperature T_s ($P_s \approx 4.2$ GPa and $T_s \approx 350\,°C$).

sion the shock front consists of two parts, a faster elastic part and a slower plastic deformation part. As the front propagates, the elastic part moves ahead and disperses whereas the plastic part lags behind and remains steep. The time lag is a measure of the rate of mechanical deformation or shape change at high strain rates.

Ultrafast laser-driven shock waves generating 5 GPa pressure were used to study molecular orientational processes occurring in a thin layer of polycrystalline energetic material [94]. It was observed that there is an orientational sensitivity of energetic materials to the direction of shock front propagation.

Recovery experiments, where the shocked material sample is examined after the shock, are ordinarily limited to refractory materials, which can withstand high pressure conditions. It is difficult to recover molecular energetic materials at substantial shock loads, since long-duration shocks usually explode the energetic material. The nanoshock technique is uniquely suited for recovery measurements of high explosives where the duration of the shock pulse is short enough (few nanoseconds) that there is little time for thermochemical decomposition reactions to take place [80].

79

3.4 Shock Interferometry

3.4.1 Introduction

As mentioned earlier, shock waves in materials are characterized by a sharp discontinuity in the thermodynamic variables of the state. A well-characterized shock is desired, with a steeply rising planar shock front running at a constant velocity. Typically, a shock wave propagating through a material at a velocity around 6 km/s causes particles in the material to jump to a velocity of 1 or 2 km/s. There are many diagnostics available to probe shock induced material dynamics. The most common methods used to determine shock rise times measure the free surface particle velocity as a shock wave exits a target material.

The ablation-induced shock wave pressure is related to the laser pulse intensity and can be calculated by hydrodynamics codes or analytical models [95, 96]. However, laser interferometry is a more accurate and frequently used way of estimating shock pressure.

Conventional shock experiments typically involve high-speed projectile impact, producing step-function shock compression which can be probed by a fast strain-gauge or by fast streak cameras. Various forms of interferometry (e.g., velocity interferometer system for any reflector (VISAR), Fabry-Perot, and optically recording velocity interferometer system (ORVIS)) with time resolutions from a few nanoseconds down to a few picoseconds have been used, depending on the system dynamics. The interferometric techniques help to clarify the mechanistic details that lead to the formation of shock waves, band structure collapse, and phase transitions in shock-loaded or laser-heated materials.

The most commonly used diagnostic in shock physics is VISAR, which uses fiber-coupled continuous-wave laser light to measure the velocity of a free or windowed surface of a shocked material [97]. The probe light is reflected from a sample at normal incidence to the sample surface and then recombined with light that has been optically delayed. The oscillations in the intensity of the superposed signal provide a measurement of the velocity of the sample surface. Recently, photon Doppler ve-

locimetry (PDV) has been developed, a technique that also probes the sample surface at normal incidence (most frequently) to extract velocities [98]. These diagnostics are unable to discriminate between shock induced optical refractive index changes and material motion. Changes in the optical properties of the shocked material can impact the measured velocity as shock compression causes an increase in the refractive index, which changes the optical path length.

Although velocity is the most common property measured during a shock experiment, x-ray diffraction (XRD) has been used to probe both shock compression [99, 100] and shock-induced phase changes [101, 102]. Its sensitivity to nuclear position provides important and definitive information about lattice structure, but its use has been limited to materials with simple crystal structures, with readily available single crystals, and with low x-ray absorption cross-sections. Despite the definitive nature of XRD data, it cannot be used alone as a shock diagnostic because velocity information is still required to relate the XRD data to a shock pressure.

More recent spectroscopic method, frequency-domain interferometry, promises sub-picosecond time resolution [103, 104]. Evans et al. have employed this method to measure the average shock velocity and final free surface velocity of aluminum films for laser-driven Mbar shocks [105]. Fourier domain interferometry [106, 107] has produced both space and time resolved measurements of materials subjected to laser driven shocks and plasmas [108, 109].

Ultrafast time-resolved interferometry has been used to measure shock wave breakout and is a powerful means of investigating shock dynamics in a variety of materials. It provides detailed information about the dynamic optical properties and pressure profile of laser-generated shocks propagating in materials [110, 111, 112].

Interferometric data have been well-modeled using bulk Hugoniots, and the use of direct laser drive does not lead to a thermodynamic state significantly different from the Hugoniot, allowing us to make the assumption that on these timescales (hundreds of picoseconds), the states are well-approximated as the same states obtained with gas-gun systems [113]. Moreoever, interferometric results as a function of shock strength suggest that sub-micron films have essentially the same material response

to shock loading as macroscopic samples [114, 115] and the Hugoniot (locus of final states reachable in a single shock) of the thin film material is indistinguishable from that of bulk material. The similarity of the thin film and bulk Hugoniots supports the use of thin film shock dynamics measurements, which allow the temporal and spatial resolution necessary to characterize molecular properties, to contribute to a detailed understanding of larger-scale shock phenomena [116].

3.4.2   Types of Shock Interferometry

The time profile of the shock breakout event is built up from many repeated single shot interferometry measurements on different nearby sample regions, over a range of time delays between the shock generating pulse and the probe pulses. Two types of femtosecond time-resolved interferometry are used to characterize the shock. Both utilize a modified Mach-Zehnder interferometer with the sample in one arm and a time delay in the reference arm. The optical synchronicity is simply obtained by changing the optical path lengths with translation stages, and the time resolution results from the pulse duration which gives the duration of the frames that are recorded as a function of delay.

In spectral interferometry or frequency domain interferometry, the reference arm is slightly longer than the sample arm and the beams are recombined collinearly and focused into a spectrometer, as shown schematically in Figure 3-7. The two probe pulses are stretched in time by the spectrograph, so that they overlap in time and space at a charge-coupled-device (CCD) and produce an interference pattern along the wavelength axis. The resulting CCD image for each experiment is analyzed using Fourier transform methods to extract the difference in phase between the two probe pulses caused by changes in the film surface position or the optical properties of the sample [117].

Geindre et al. determined the relative phase shift between the probe pulses caused by motion of the free surface and/or transient changes in the optical properties of the surface during shock breakout, by performing an inverse fast-Fourier transform on the spectral intensity interferogram recorded on the spectrograph CCD [103]. If the
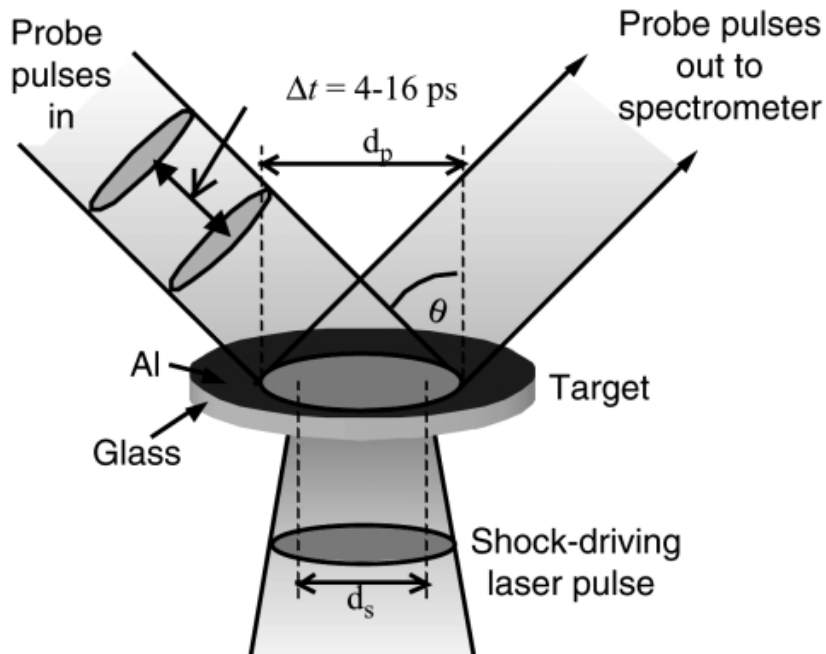
Figure 3-7: Schematic diagram of the femtosecond laser-driven shock frequency domain interferometric experiment [113].

shock arrives at the metal surface after both probe pulses, the surface is essentially unchanged, giving zero phase shift. If the shock arrives between the two probe pulses, the measured phase shift is proportional to the fraction of the time between probe pulses that the surface is moving. If the shock arrives before both probe pulses, a maximum phase shift is reached [118].

In femtosecond time-resolved two-dimensional spatial interferometry, the reference and sample arms of the interferometer are made the same length to adjust the temporal overlap between the two arms and maximize fringe contrast and the beams are combined non-collinearly, so that an interference pattern is produced at the CCD (no spectrograph is used). Two dimensional spatial information about material motion and/or sample optical properties is obtained from the interference patterns using 2-D Fourier transform methods [116]. Gahagan, Funk and Moore have demonstrated 2-D spatial interferometry, using thin metal films (250 nm to 2 μm nominal thickness) vapor deposited onto thick glass as target samples [119, 120]. The experimental arrangement is shown schematically in Figure 3-8.
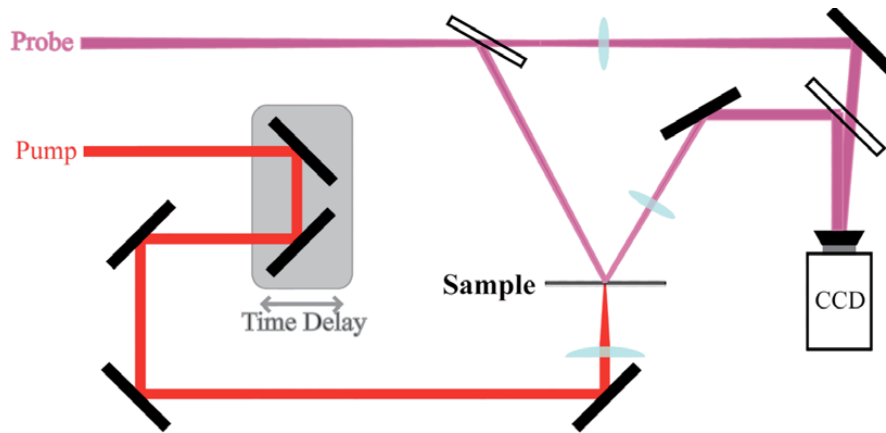
Figure 3-8: Schematic diagram of laser shock generation as probed using spatial interferometry to measure the motion of the metal at the free surface. The probe pulse shown above was variably delayed with respect to the pump pulse and was sent into a Mach-Zehnder interferometer that probed the free surface of the sample. The two legs of the interferometer were recombined at a small angle on a CCD camera, which recorded interferograms before, during, and after each event [68].

More recently, ultrafast dynamic ellipsometry (UDE) has been developed which is sensitive to changes in the electronic structure as manifested through changes in the material's index of refraction, and may be used in some cases as a non-invasive probe of the phase of a material or its chemical reactivity [121]. UDE measures the space and time resolved phase shift and reflectivity of laser light incident at two different angles to the shocked surface, to extract the relative contributions of the shock-induced optical and material motion effects.

3.4.3   Experimental Methodology

Laser System

A Ti:sapphire femtosecond laser oscillator (Kapteyn-Murnane Laboratories) produces the seed pulse that is centered at 800 nm with a bandwidth full width at half maximum

(FWHM) of 10 nm. A femtosecond Ti:sapphire amplifier (Titan Quantronix) utilizes a grating based pulse stretcher and compressor, with a regenerative and multipass amplifier, to produce up to 4 mJ per pulse at 1 kHz repetition rate and down to 100 fs pulse duration. Typically, the laser system is run at 60 Hz repetition rate and 250 fs pulse duration (FWHM). Femtosecond pulses can generate shock waves in bare aluminum thin films that exhibit sustained pressures from hundreds of femtoseconds to a few hundred picoseconds. The pressure is easily tunable by altering the energy of the laser pulse.

Material System

The targets used in experiments are polycrystalline aluminum films of 200 nm thickness produced by vapor deposition onto 250 ± 20 μm thick BK-7 microscope cover slips (Fisher Scientific) and PMMA substrates (GE Plastics). The samples are examined both with a spectroscopic ellipsometer (M-2000D, J. A. Woollam Co., Inc.) and an atomic force microscope. The best films produced have metal layer thickness variations of 1% across most of a 1-inch diameter sample.

Optical Technique & Setup

Sagnac Interferometry – Sagnac interferometry is used for monitoring ultrafast phase changes that are due to surface displacement and for the shock pressure characterization. The particular advantages of this interferometer are its simple "common-path"design and operation at normal incidence. The common-path design obviates the need for active stabilization and renders the interferometer less sensitive to parasitic fluctuations from thermal and acoustic fields.

The Sagnac interferometer, as shown in Figure 3-9, relies on the interference between a signal pulse (that arrives at the sample after a pump pulse) and a reference pulse (that arrives before). A nonpolarizing beam splitter (NPBS) samples a portion of this beam for differential detection. The remaining half of the input beam is split into vertical and horizontal polarizations, the signal and the reference beams, respectively, by the first polarizing beam splitter (PBS). The beams are recombined
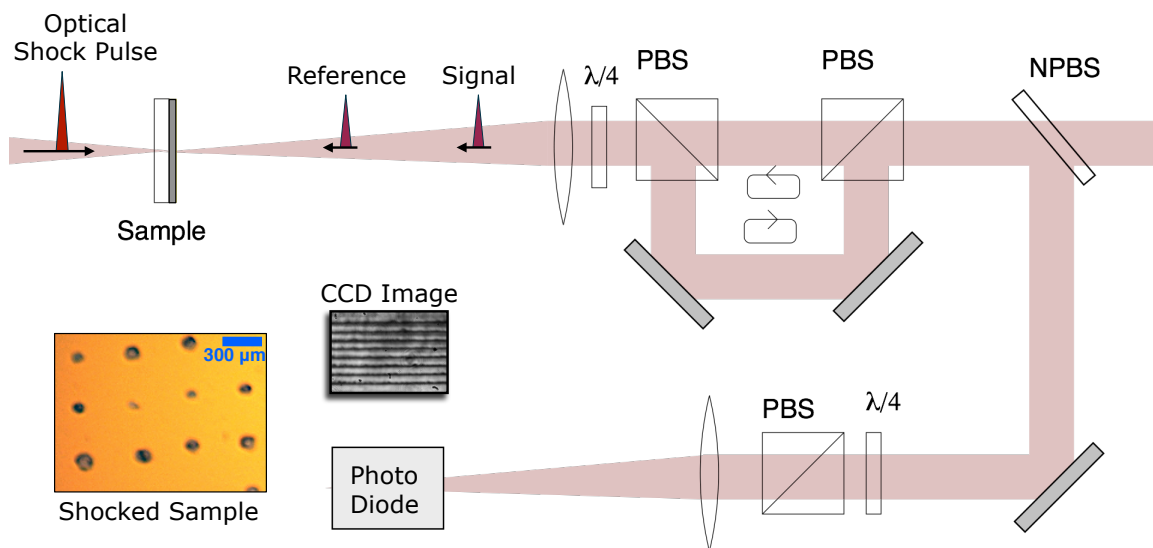
Figure 3-9: Optical design of the Sagnac interferometer. PBS, NPBS and $\lambda/4$ stand for polarizing beam splitter, non-polarizing beam splitter, and quarter-wave plate respectively. The detection is done interferometically by probe beams (signal beam and reference beam) of wavelength 800 nm, generated by using PBS and temporally separated by 1 ns from one another. The two probe beams are focused at normal incidence through an achomatic converging lens onto the front surface of the film and are counter-propagating (travel in opposite directions inside the interferometer), but cover the same total optical path. The signal and reference beams are superposed collinearly on either a CCD (not shown in the schematic) or a photodiode. The inset at the lower left corner shows the optical microscope image of a 200 nm aluminum layered sample that is vapor deposited on a 250 μm glass substrate. The holes in the metal film are generated by laser shock pulses of varying energy which are used to tune shock pressure. The CCD image shows an interferogram of the surface of the sample during shock breakout. The pump and probe wavelength are 800 nm. By changing the optical path of the pump beam with an optical delay line, I can obtain a scanning time range of 0 - 1 ns and femtosecond temporal resolution (determined by the optical pulse duration).

at the second PBS, pass through a $\lambda/4$ plate (oriented at 45°), and are focused at normal incidence onto the sample using an achromatic convex lens. When they are reflected the beams reverse paths and are combined at the first PBS, and half the interferometric beam is reflected by the NPBS. The two probe pulses travel in opposite directions inside the interferometer, but cover the same total optical path termed "common-path", and so the interferometer is relatively insensitive to alignment error and mechanical vibration. At this point the probe and the reference beams have perpendicular polarizations and are made to interfere with the aid of a second $\lambda/4$ plate and a PBS with the transmission axis aligned at 45°. The $\lambda/4$ plate and PBS combination are used to achieve maximum phase sensitivity and this also makes it possible to obtain the optical phase change signal directly.

Experiment − The pump and probe pulse trains are derived from the same seeded amplified Ti:sapphire femtosecond laser system. The shock generating pump pulse (0.1 - 4.0 mJ) is passed through a time delay and then focused through a borosilicate glass or PMMA substrate onto the glass/Al or PMMA/Al interface respectively to a diameter of 100 μm (backside of the target). After the shock drive pulse strikes the substrate/metal film interface, laser ablation processes launch a shock, which travels through the metal film and arrives at the free metal surface. The shock wave produced in this manner has been shown to have a nearly planar spatial profile instead of Gaussian due to optical limiting and self-focusing Kerr effect in the substrate [122].

A small portion of the main laser pulse ($\sim 30\ \mu$J) reflected from a beam splitter is passed through the Sagnac interferometer, generating two probe beams - signal pulse and reference pulse. The full temporal window of measurement is tuned to 1 ns by adjusting the interferometer "common-path" length. Thus, two probe pulses (temporally separated by 1 ns from one another) are focused onto the frontside of the target (the aluminum/air interface) at normal incidence. An imaging lens is used either to image the surface onto a CCD camera (Cohu, Inc.) or to collect integrated interference signal through a photodiode. The probe pulses arrive at some time near when the shock arrives. Each pulse effectively probes the outward surface displacement of the sample and I obtain a signal proportional to the out-of-plane

surface velocity of the sample at the probed point.

In a typical measurement, a time history of the shock breakout event is built up from many repeated measurements, while precisely adjusting the optical time delay (or optical path) between the shock generating pulse and the probe pulses through an optical delay line. The signal from the photodiode or the interferogram from the CCD is transferred to and stored on a computer, and all signals or interferograms from a time series, built up by adjusting the time delay in the excitation (or pump) laser arm. In all experiments, the target is mounted on a GPIB computer-controlled x-y translation stage (where z is the normal to the target surface). The target is rastered $400\,\mu$m between pump pulse shots (conducted at 1 Hz using an optical shutter to block unwanted laser pulses) so that each 'experiment' involves undisturbed material.

The experiment reported here measures the relative phase shift between a pair of probe pulses initially produced by the Sagnac interferometer. Reflection of these pulses from an accelerating metallic surface (due to the emerging shock wave) will yield a phase shift that depends on time and the relative positions of the probe beams with respect to the onset of acceleration. Very small changes in phase (10^{-3} rad) can be measured using the Sagnac interferometer. From the onset of the phase shift and a good knowledge of the time zero, which is obtained with a very thin tracer (10 nm) layer on each target, it is also possible to measure the shock transit time across the aluminum layer very accurately.

3.4.4   Data Analysis

Figure 3-10 shows the relative phase shift as a function of delay time between the shock generation pump pulse (130 μJ) and the probe pulses measured using Sagnac interferometry in 200 nm thick samples of aluminum over glass and PMMA substrates. The slope of the best fit linear curve for data points between 0 ps to 110 ps is identical for both glass and PMMA substrates (as depicted in red and blue dotted lines respectively). Thus, it is clearly evident that there is no inherent effect of the substrate properties (density or refractive index) on the shock generation mechanism (or pressure profile) and the shock dynamics. Furthermore, the shock rise time is less
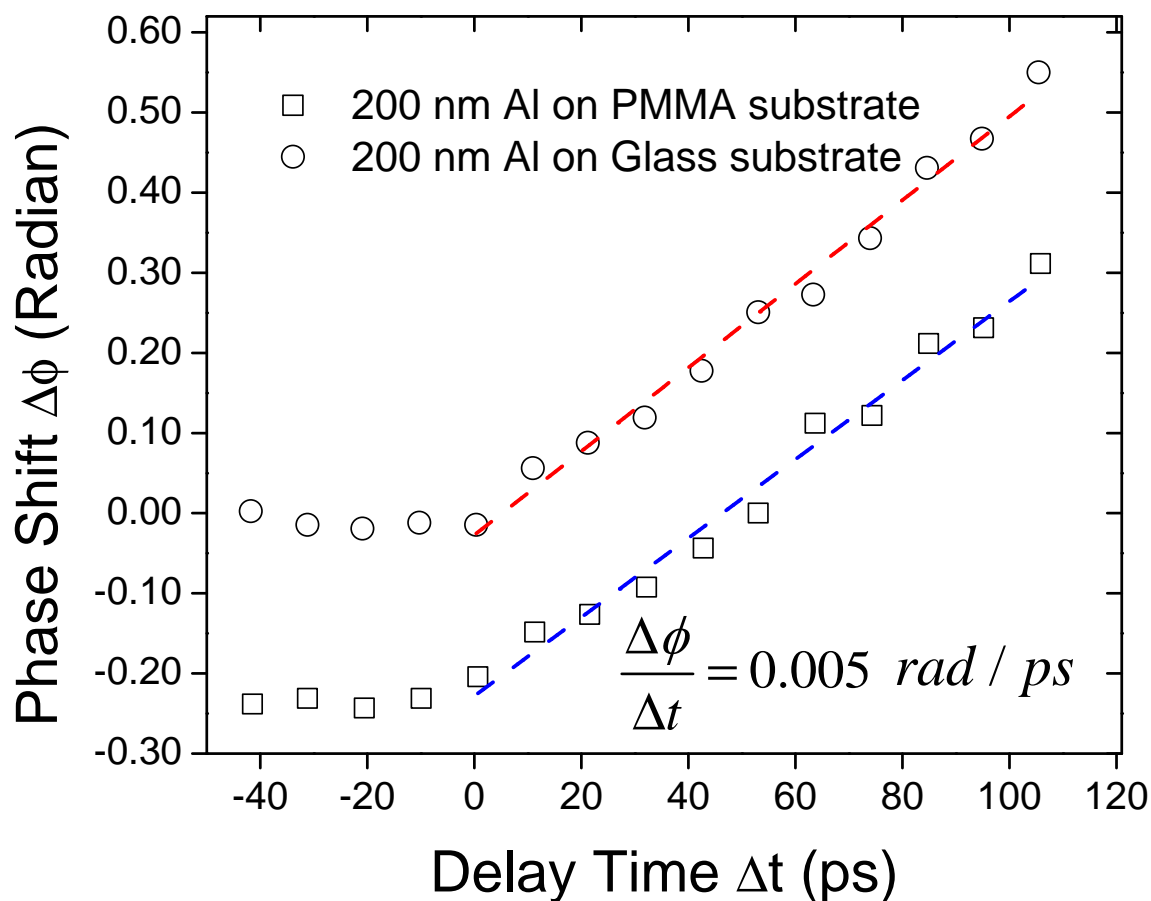
Figure 3-10: Phase shift measured by the Sagnac interferometry as the shock wave exits the free surface of a 200 nm thick aluminum layer on glass and PMMA substrates. The vertical axis represents the phase difference (that is, signal beam phase minus reference beam phase) between the two optical pulses reflected from the film surface at different moments in time. The phase shift is due to movement of the aluminum free surface, generated by focusing a 130 μJ pump pulse to a spot size of 100 μm (incident laser fluence is 1.65 J/cm^2). The probe used is 800 nm, derived from a seeded, mode-locked, amplified Ti:sapphire femtosecond laser system. The red and blue dotted lines are the best-fit linear curves for phase shift data points measured for glass and PMMA substrates respectively. The slope of the linear fit is identical for both substrates (0.005 rad/ps) and hence so is the time-dependent pressure profile. Using the phase shift versus time to find the free surface velocity, the pressure is calculated to be 2.5 GPa.

than 10 ps as the curve becomes linear afterwards suggesting constant pressure for the rest of the time history.

There are sources of noise caused by shot-to-shot beam pointing instability, intensity, and air density fluctuations along with the instrumental function of the interferometer setup that also introduce some background noise.

Shock Pressure Characterization

The final pressure achieved in the aluminum is determined from the corresponding shock and particle velocities in the bulk film derived from the free surface velocity measurements.

A measurement of the reflected light from a bare Al surface as a shock wave emerges yields a phase shift that is primarily a result of the movement of the free surface. Funk et al. measured phase shifts due to Al optical properties at the peak of the pressure wave in Al, but they are orders of magnitude smaller than the phase shifts due to surface motion discussed here [110].

The one-dimensional surface displacement, $\Delta\delta$, is related to the phase shift, $\Delta\phi$, geometrically by the equation

$$\Delta\delta = \frac{\lambda}{4\pi cos\theta}\ \Delta\phi \tag{3.7}$$

where λ is the probe wavelength and θ is the angle of incidence.

The free surface velocity, U_{fs}, is calculated using the change in the phase shift, $\Delta\phi$, and the change in time, Δt, as given by

$$U_{fs} = \frac{\lambda}{4\pi cos\theta}\ \frac{\Delta\phi}{\Delta t} \tag{3.8}$$

The slope of phase shift versus time, $\Delta\phi/\Delta t$, in Figure 3-10, as measured by Sagnac interferometer, is 0.005 rad/sec, λ is 800 nm and θ is 0°. Thus, U_{fs}, calculated using equation 3.8, is 0.32 nm/ps (or 320 m/s).

For a free surface at low shock pressures, the particle velocity, U_p, is well approximated as half of the free surface velocity [1]. In other words, $U_p \approx U_{fs}/2$ is 0.16 nm/ps in our experiments. The shock speed U_s and pressure P in the initially unshocked aluminum can be determined from U_p, the aluminum Hugoniot (experimental U_s versus U_p relation), and the Hugoniot-Rankine equations that account for conservation of mass, energy, and momentum across a shock discontinuity [123]. A more extensive discussion of free surface velocity measurements in thin metal films is available from Gahagan et al. [106].

The shock speed, U_s, is calculated from the aluminum Hugoniot [56]

$$U_s = 1.34 \, U_p + c \tag{3.9}$$

where c = 5.38 nm/ps, approximately the longitudinal sound speed.

Shock Pressure, P_1 is calculated using the relation

$$P_1 = P_0 + \rho_0 \, U_p \, U_s \tag{3.10}$$

where P_0 is the initial pressure and ρ_0 is density of unshocked aluminum, 2.712 g/cm^3. U_s and P_1 for the aluminum shock shown in Figure 3-10, calculated using equations 3.9 and 3.10, are 5.6 nm/ps and 2.5 GPa respectively.

On the timescale of this experiment, the acceleration of the material at the shock front is not instantaneous. This acceleration has been studied in aluminum and other metals [124], in which the free surface position of the metal fit very well to a function of the form

$$x(t) = \int \frac{1}{2} \left[1 + tanh \left(\frac{t - t_0}{\tau_{fs}} \right) \right] U_{fs} \, dt \tag{3.11}$$

where x is the surface position, t is time, t_0 is the time of maximum material acceleration, and τ_{fs} is the time constant of the rise. Here, t_0 and τ_{fs} are fitting parameters characterizing the free surface velocity profile.

To obtain a particle velocity and shock wave rise time, I assume a hyperbolic tan-

gent form for the free surface velocity as given in equation 3.11. The final free surface velocity is taken to be twice the final particle velocity of the shock state, and assumes a reflected Hugoniot or Walsh equation of state for the rarefaction wave. Thus, the free surface velocity, particle velocity and shock velocity are all characterized by the single time constant τ_{fs}. Defining the shock wave rise time as the $10\text{-}90\%$ width of the hyperbolic tangent rise gives $\tau_{sh} = 2.3\,\tau_{fs}$. The pressure rise time of less than 10 ps is determined by fitting free surface velocity to the hyperbolic tangent function.

3.4.5 Results and Discussion

Sagnac interferometry has been shown to provide detailed information about the dynamic properties and pressure profile of laser-generated shocks propagating in metal thin films. No effect of the substrate on the shock pressure has been observed. The peak pressure is 2.5 GPa for a 250 fs 130 μJ pulse focused to a 100 μm spot (incident laser fluence 1.65 J/cm^2), and the pressure is easily tunable by altering the energy of the laser pulse. The rise time is less than 10 ps and a constant sustained pressure is maintained for a few hundred picoseconds. Sagnac interferometry allows characterization of laser driven shock waves in a more elegant and precise manner than other interferometric methods. The stability, sensitivity and data collection time in the Sagnac interferometer are better than Michelson, Mach-Zehnder and other interferometers, especially for laser shock experiments.

Chapter 4

Single-shot ISTS-Shock Studies

4.1 Introduction

Shock compression of soft condensed matter represents an area of considerable scientific interest because the data from shock loading experiments provide a real-time probe of physical and chemical changes at extreme conditions [125, 126]. This chapter involves design of a unique experiment to probe the change in mechanical properties of a thin film subject to laser-induced shock-loading. The technique combines two proven methods, ISTS and conventional laser of a shock wave that propagates through the plane of a thin sample, and is capable of optical shock generation and optical detection of acoustic waveguide modes in the sample at high repetition rates. The data obtained from this experiment are intended to be complementary to results of conventional dynamic mechanical characterization, imposing large compressive strains at very fast loading rates. The response of the sample after as well as during the initial shock loading is probed, permitting assessment of complex structural evolution under highly non-equilibrium conditions.

This chapter describes an early attempt at ISTS measurements on samples under laser-induced shock loading, using ISTS as a technique for monitoring the dynamically evolving physical properties of shocked materials. It demonstrates that material can be probed on a single shot basis under laser shock loading, which has never been achieved in the past. ISTS measurements go beyond measurements like Hopkinson bar
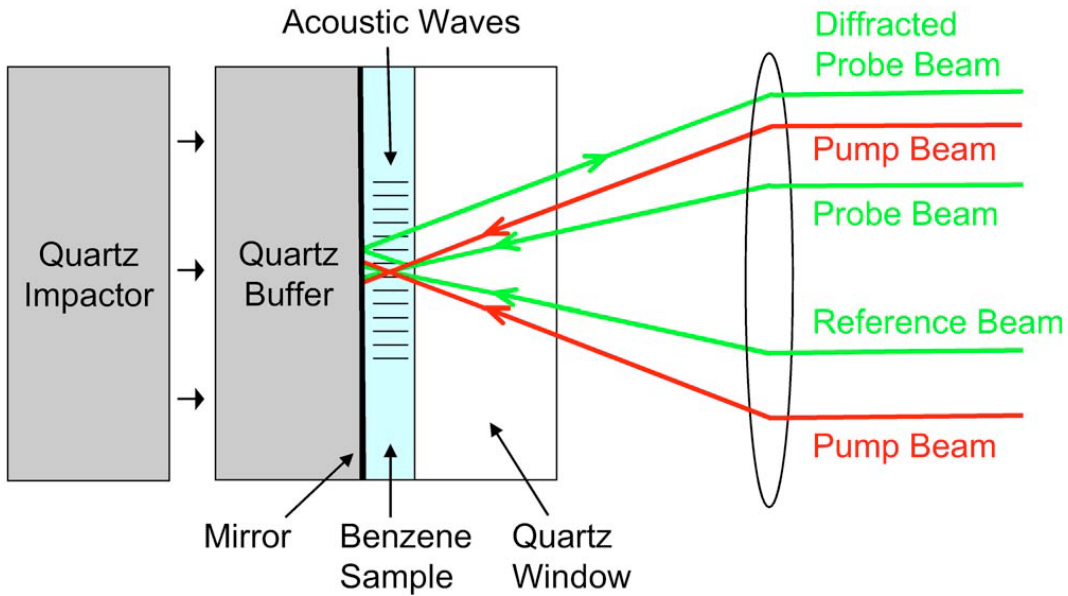
Figure 4-1: Experimental configuration for single-shot ISTS measurements under shock wave compression. The projectile is incident from left, precluding the placement of optics on that side of the sample. A mirror incorporated as part of the sample cell serves to return the beams to the same side from which they are delivered [66].

or shock interferometry because they permit monitoring of the sample as a function of time following shock loading, not just measurement of the shock speed as the wave is passing through. Moreover, the portion of the phase diagram reached through shock loading is generally inaccessible by other means, due to its unique combination of density, stress, and temperature. Due to the rapid and destructive nature of these conditions, direct real-time measurements of time-evolving physical properties during the response to shock is almost never attempted.

4.2   Previous Studies

Experiments have been done to probe material properties using ISTS detection under gas gun shock loading in liquid benzene shocked to nearly 1 GPa [66]. The setup used for this experiment is shown in Figure 4-1 where ISTS measurements from the shocked benzene are obtained using a four beam pump-probe configuration. A transient thermal and acoustic grating (24 μm acoustic wavelength) is formed in the

530 μm thick benzene sample using the interference pattern from two crossed pump beams. Figure 4-2 shows distinct, large changes in acoustic frequency under shock loading. The peaks at 91 MHz and 108 MHz are from the shocked benzene behind the shock wave and correspond to reported sound speeds of 2165 m/s and 2607 m/s at 0.42 GPa and 0.85 GPa shock pressure, respectively. The measured ambient sound speed for benzene is 1306 m/s. It is also observed that benzene appears to not undergo a transition into crystalline or even glassy state for a considerable time after the shock passes through, even though under the same static pressure it would do so. So far, this is the only experimental data in the literature concerning ISTS measurements during shock conditions. The conventional gas gun destroyed the entire sample and the mounting and focusing optics around it each time a measurement was made, i.e. each laser shot. The repetition rate of the measurement was never greater than two shots per week.

4.3   Simulations

Simulations were done to predict the shift in acoustic frequency for a polymer film undergoing laser-induced shock loading. The results are shown in Figure 4-3, where shock waves were assumed to cause 10% variation in density and bulk acoustic longitudinal and shear acoustic velocities of a 1 μm thick PMMA polymer film. The pressure in the shocked state is less than 1.5 GPa, calculated using the Hugoniot data for PMMA generated using static-loading conditions through mechanical impact. The result was that the lowest-order acoustic waveguide mode velocity in the film is 10% higher. There is a clear cut difference in the acoustic frequency throughout the whole range of wavevectors, suggesting the usefulness of ISTS under these conditions to obtain real-time experimental data.
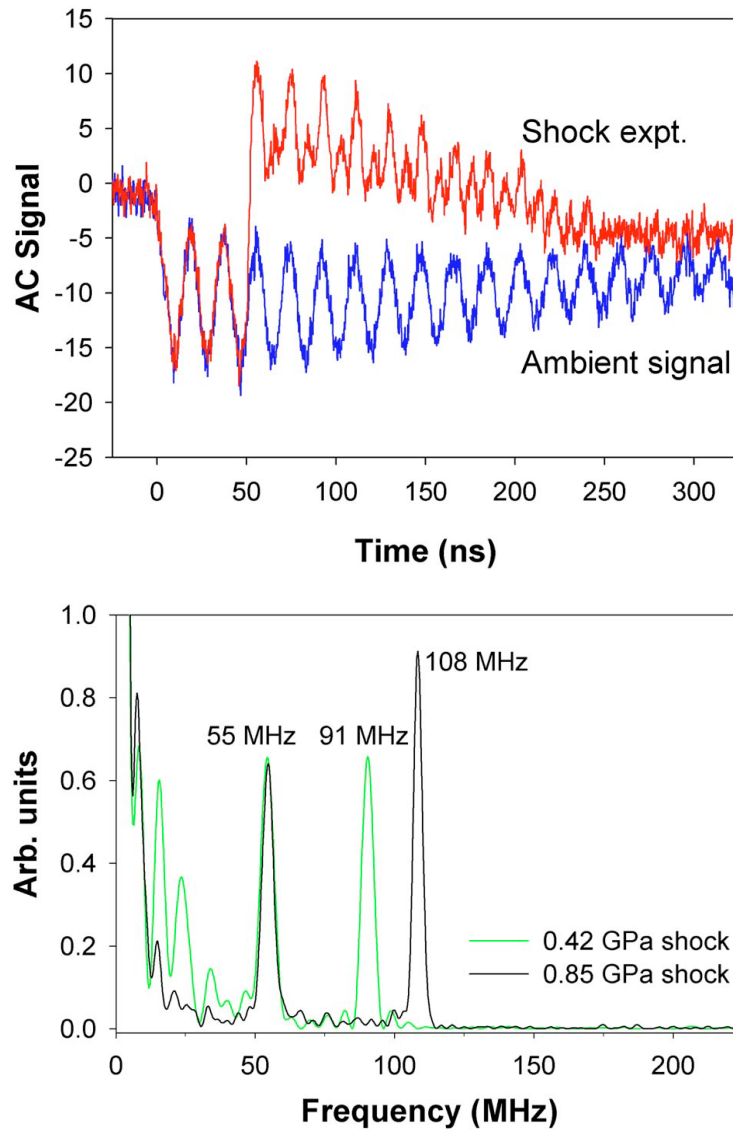
Figure 4-2: Top: ISTS signal in benzene under gas gun shock loading at 0.85 GPa at 24 μm acoustic wavelength. The blue trace is from the unshocked/ambient sample, and the red trace is the one taken during a shock experiment. At 0 ns, the laser pump pulses arrived at the benzene sample. The shock wave arrived at the front of the benzene sample at 60 ns. After the arrival of the impactor, there is a jump in the signal, likely due to a change in alignment. The liquid gradually shifts from unshocked to shocked as the shock front progresses through the sample. This is made evident by the diminishing of the original signal frequency and the growing in of the shocked signal frequency. Bottom: Fourier transform of signal from shocked benzene at 0.42 GPa and 0.85 GPa. In both instances, there are two distinct frequencies that appear in the shock experiment. The lower (at 55 MHz) is due to the signal at ambient conditions, while the higher ones (91 MHz and 108 MHz) are in the shocked state [66].
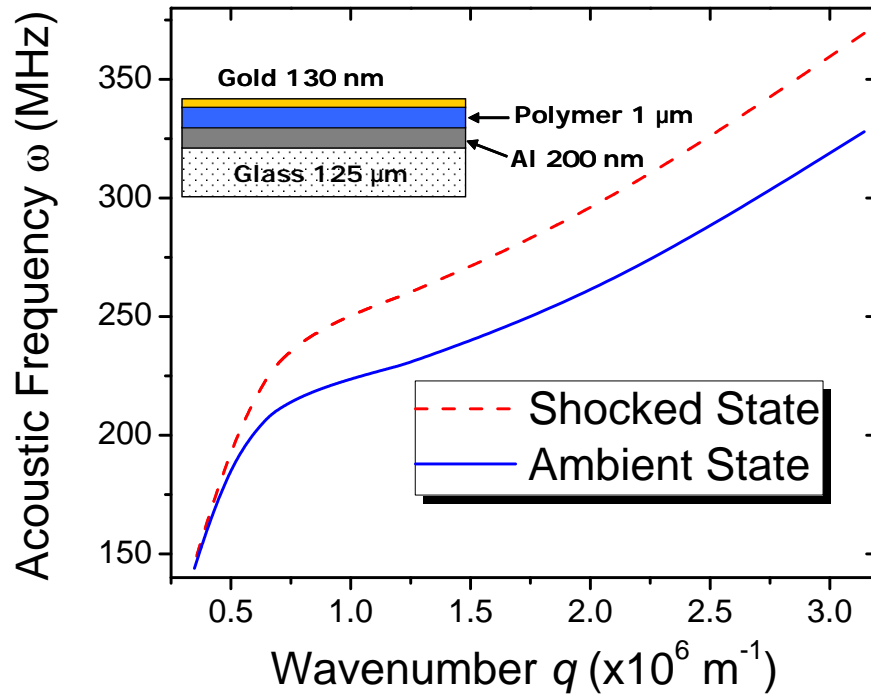
Figure 4-3: Simulations showing acoustic dispersion curve for a typical polymer film (e.g., PMMA) of a 1 μm thickness through ISTS measurements under ambient (unshocked) and shock wave compression. The shock waves are assumed to cause 10% variation in density and acoustic velocities of the unshocked material. The solid blue curve represents material behavior in the unshocked state and the dotted red curve is the response of the same material under moderate shock loading of less than 1.5 GPa (easily achievable with our femtosecond laser system). Notice the clear cut difference in the acoustic frequency at higher wavevectors. The inset shows the sample configuration with underlying layers of aluminum (200 nm) for laser shock generation, borosilicate glass substrate (125 μm) and an overlayer of 130 nm gold for good signal-to-noise ratio in the reflection mode geometry.

4.4 Experimental Studies

Until now, ISTS measurements and shock generation have been discussed separately. This section presents their integration and shows a first attempt at measurements on samples under laser-induced shock loading using ISTS as a monitoring technique.

4.4.1 Material System

The materials studied are mostly amorphous polymer systems, with a few samples consisting of multi-domain systems such as block copolymers and nanocomposites. Studies were conducted to probe the effects of varying shock pressure and sample geometries.

The materials of initial interest are ones which can sustain shock pressure for sufficiently long times that their compressed states can be probed using ISTS measurements, which require sufficient time for at least a few acoustic oscillations to be observed. Conventional laser shock generation begins with ablation of a thin metal layer, launching a shock wave that is relatively short in duration. Its duration may be lengthened by propagation into a material with a slow sound speed. Therefore, materials having slow acoustic speeds are the best candidates for such measurements. However, slow sound speeds allow longer times for acoustic damping, and hence, materials with good ISTS signal to noise ratio are needed. Most polymers like PDMS, PC, PMMA, SU-8 (epoxy-based photoresist), polyimides, polyurethanes, etc. are good candidates for such measurements.

Recent research interest has also included the use of nanomaterials to further explore and enlarge the property space of polymers. The incorporation of nanoparticles into the polymer matrix can potentially alter the local microscopic and mesoscopic structure and thus offers an opportunity to tailor the rate-dependent mechanical deformation and failure behavior of the polymer [127]. Nanomaterials can be introduced into a polymer system by blending or chemical attachment. Blending is simple and can be done by physical means, but there may be solubility limits resulting in phase separation. Polymeric samples doped with aluminum nanoparticles (~ 100 nm dia-

meter) are also investigated, where the nanoparticles are used for creating miniature blasts in the bulk of the sample and launching shock waves in their vicinity. The incorporation of nanoparticles into the polymer has another advantage of maintaining the shock pressure in the polymer for longer (i.e. a couple of nanoseconds), and this gives us enough time window to probe the dynamic material response under shock loading using the ISTS technique. A more detailed discussion on the use of nanoparticles in shock generation is presented in the next chapter.

4.4.2 Sample Fabrication and Characterization

Sample design and fabrication is a big challenge for an experiment done on a single-shot basis and requiring sustainance of shock pressure for long time intervals. Typically, the sample is a multilayer structure with a substrate, either glass or sapphire, and other material layers fabricated as per need using spin-coating (for polymeric materials) and e-beam deposition for metals like aluminum and gold. The thicknesses and uniformity of the multilayers are characterized using ellipsometry, profilometry and AFM. Some samples can be scanned under SEM or TEM, where a multilayer film cross section is prepared by a focused ion beam (FIB).

4.4.3 Optical Set-up

The two main components of the experiment are laser shock generation, achieved through intense pulsed ablation of a metal film at the backside of the sample, and ISTS photoacoustic measurement of mechanical properties, achieved through mild spatially periodic heating and time-resolved observation of acoustic waves at the front side of the sample. Figure 4-4 shows a schematic illustration of the ISTS measurement with the excitation and probe beams and the signal on one side of a sample (right-hand side excitation pulses, probe, and diffracted signal) and laser shock generation at the opposite side (left-hand side shock pulse). The sample of interest is typically a polymer layer surrounded by metal layers that are irradiated for shock generation (aluminum layer) and for acoustic wave generation and probing (gold layer). The

time-dependent acoustic response yields the sample dynamic mechanical properties before, during, and after shock loading.

In our case intense shock generation pulse (800 nm, ~ 1 ps, 0.1 - 5.0 mJ focused to 100 μm spot diameter) strikes an aluminum film and creates a plasma. The expansion of the aluminum film drives a mechanical shock wave into the adjacent polymer layer [128]. For laser generated planar shock waves, the diameter of the spot must be at least ten times the run distance [129].

The excitation and probe laser light used for the ISTS measurement strike a gold film on the opposite side of the sample. Although the light pulses do not penetrate the top gold film layer, the acoustic response that they generate persists throughout this layer and the sample of interest beneath it, and the acoustic properties therefore reveal the mechanical properties of the sample. If a shock wave is launched, then changes in the acoustic behavior may be observed as the sample undergoes time-dependent changes due to shock loading. The entire time-dependent signal can be recorded in a single laser shot, so even if the sample is damaged permanently by shock, data can be collected reliably.

Laser-driven shocks are generated at a rate of 1 shot/sec, and the sample is rastered in the plane to ensure that an undamaged region is irradiated each time. In a sample of 1-inch diameter, over a thousand shots can be conducted in a few minutes. This presents a huge advantage over ISTS measurements on samples under gas gun shock loading, in which the entire sample, not just a small region, is destroyed in a single shot and at most a few shots per week are practical. Moreover, the parameters of the laser pulse used to launch the shock wave, including beam size and shape, pulse duration, and intensity, are fully controllable, yielding considerable control over the shock wave that is generated.

Each of the ISTS traces recorded from a single shot contains the entire time-dependent response, typically showing acoustic oscillations that continue for several tens of nanoseconds. A translation of a phase mask changes the acoustic wave vector, enabling the acoustic dispersion relation to be determined.
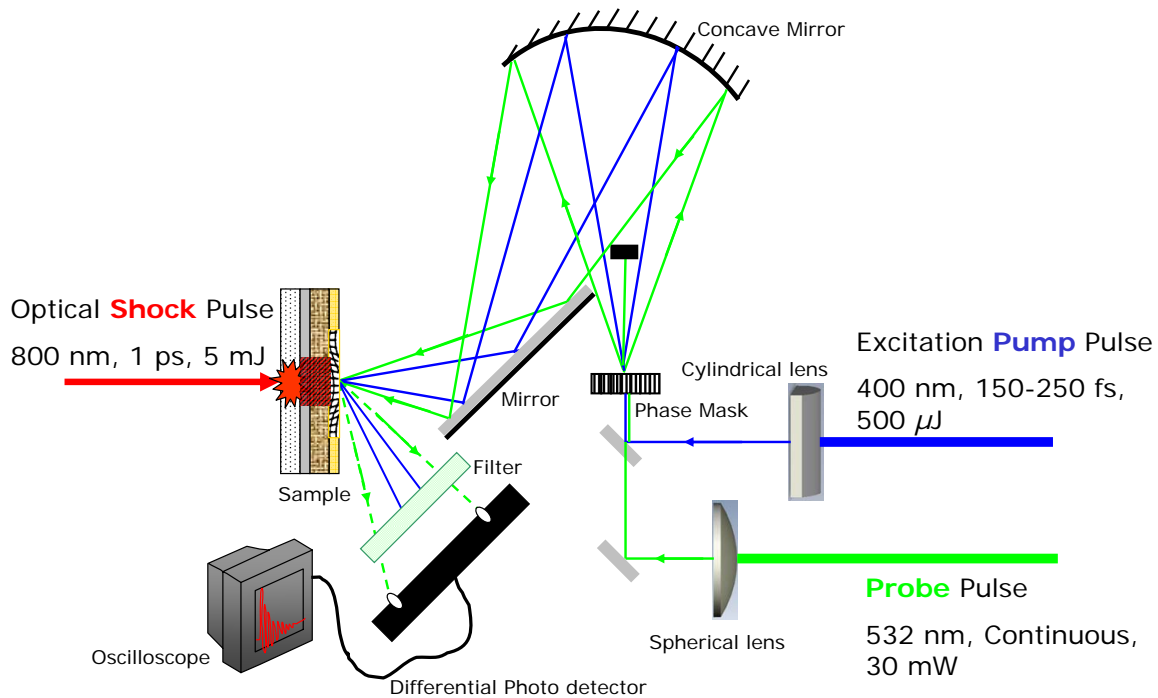
Figure 4-4: Schematic illustration of the ISTS-Shock experiment in reflection mode using conventional "front-back" approach. The schematic shows the sample assembly, shock laser pulse and shocked region, ISTS pump and probe beams and ISTS measurement region. An intense laser 'shock' pulse (shown by red arrow) irradiates a thin layer at the back of the sample assembly to generate a shock wave that propagates into the polymer sample layer of interest (shown in red square). The shock response is probed from the front through ISTS measurements, in which crossed excitation pump pulses (shown in blue color) generate an acoustic response in the sample and probe laser light (shown in green color) is diffracted by the acoustic wave to reveal time-dependent acoustic oscillations and damping. The acoustic wave is generated by ISTS in the top layer but extends throughout the multilayer sample into the material of interest, whose time-dependent response to the shock can therefore be monitored.
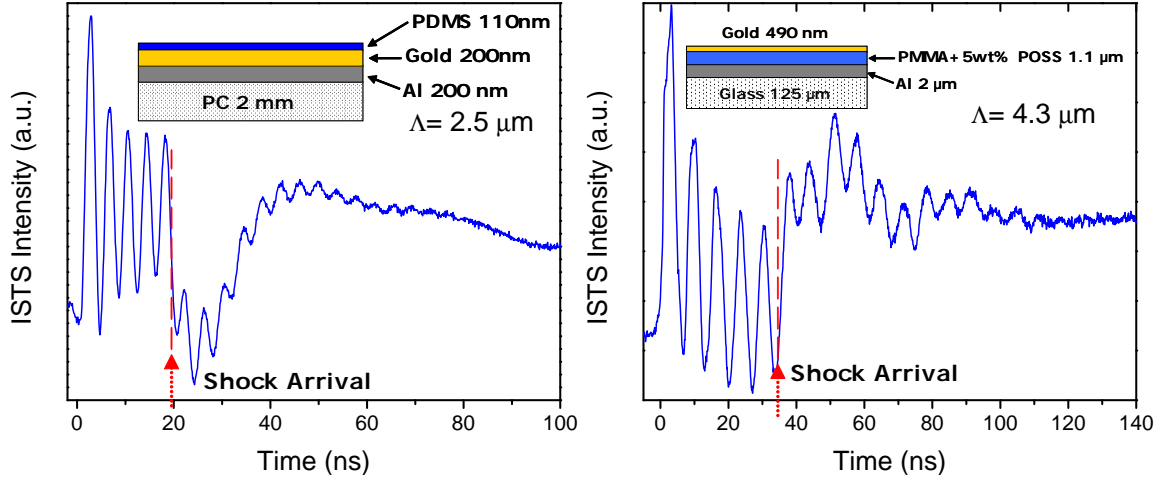
Figure 4-5: ISTS signal from samples during shock propagation. The sample configuration and ISTS acoustic wavelength Λ are shown in the inset of each figure. The data are recorded on a single-shot basis from different shocked regions of the sample since each sample region that is irradiated by the laser shock pulse is permanently damaged. The data shown are obtained by averaging of signals from 25 single shots. The arrival of the shock front is marked by red dotted line and an arrow on the time axis. There is no marked change in the acoustic frequency before and during shock loading.

4.5 Data Analysis and Results

The first ISTS measurements on polymer samples subjected to laser shock loading have been conducted. The samples studied were polymer (PMMA or PDMS) layers that were spin-coated onto a glass substrate. The optical shock pulse was focused to a 100 μm spot size and the ISTS acoustic wavelength was either 2.5 μm or 4.3 μm. Figure 4-5 shows data recorded from the samples during shock loading (generated using 700 μJ laser pulse energy). The ISTS measurement was made on a single-shot basis and the data shown are averages of 25 measurements. Since the sample region that is irradiated by the shock pulse is destroyed, the measurements of shocked material were made at different sample locations. The results are sufficiently reproducible to permit effective signal averaging. There was no substantial effect of the shock pressure on the acoustic frequency, clearly revealing that the material is under small-amplitude shock loading and below the single-shot threshold for irreversible sample damage.

102

Similar measurements done at high laser fluence results in no measurable time-domain signal during shock loading. Many different sample configurations and material systems (as shown in Figures 2-15 and 2-16) have been tried, but with no success.

The "front-back" approach – shock initiation at the back of the sample and measurement of the shock wave and its effects at the front – poses key limitations that have frustrated direct ISTS characterization of sample responses to shock. First, the duration of the shock pressure is typically short (subnanosecond) compared to the acoustic oscillation period (typically > 1 ns) observed in ISTS measurements, so the acoustic frequency of the sample can be determined after but not during elevated shock pressure. Second, the violent destruction of the shock layer that lies directly behind the sample layer of interest causes distortion of the ISTS measurement setup including movement of the signal beam. Strategies have been developed to circumvent these limitations, but ISTS measurements of shocked sample responses remain difficult in the "front-back" configuration.

4.6 Concluding Remarks

Single-shot ISTS measurements were successfully carried on polymer samples that underwent significant perturbations resulting from laser shock excitation behind the samples. However, the short duration of the shock pulse and the violent disturbance of the shock layer behind the polymer sample layer frustrate ISTS characterization of shocked samples in the "front-back" sample configuration. The limitations of this approach motivated the developments discussed in the following chapters of this thesis.

Chapter 5

Converging Shock Waves

5.1 Introduction

Cylindrically or spherically converging shock waves have been an attractive topic of research in the field of applied physics and engineering for the past several decades. Applications include hypervelocity launchers, behavior of materials under extreme conditions, synthesis of materials, and the production of high-temperature and high-density plasma fields [130, 131]. Furthermore, applications in the field of nuclear engineering (controlled thermonuclear fusion), cavitation and blast waves have been also considered [132].

Shock wave research was traditionally developed as an element of high-speed gas dynamics supporting supersonic flights and atmospheric re-entry of space vehicles as well as applications to planetary physics [133]. Recently shock wave dynamics have been used for various state of-the-art scientific and engineering interdisciplinary studies in the fields of geophysics and medicine. Many aspects of explosive volcanic eruptions, asteroid impact events, underwater shock waves, and tsunami waves in oceans are closely related to shock wave phenomena. Shock waves have been successfully applied to medical therapy including lithotripsy (non-invasive removal of urinary tract stones by use of micro-explosives), destruction of kidney stones, revascularization of cerebral embolism, drug delivery, and various other interesting therapeutic methods [134].

Many theoretical and experimental studies have been performed on converging cylindrical shock waves to produce an extreme condition of ultra-high pressure, temperature and density [135, 136]. Guderley was the first to analytically investigate the convergence of cylindrical shock waves using a similarity power law assumption for the radius of the converging shock as a function of time [137]. Time-space relations of shock propagation obtained through numerical methods are represented in equations 5.1 - 5.3.

$$\frac{R_s}{R_0} = \left(1 - \frac{t}{t_c}\right)^{\alpha} \tag{5.1}$$

where R_0 is the radius of the initial excitation ring, R_s is the position of the shock front, t_c is the time when the converging shock arrives at the center and α is the similarity exponent. Lower values of the similarity exponent give higher values of the shock acceleration and thus higher velocity as the shock approaches the center of convergence. Numerical calculations indicate that the most favorable shape in terms of shock velocity and acceleration is the circular one. The value of α depends on the ratio of specific heats γ and the shock propagation geometry. Numerical integration as well as experimental analysis have found that α for air (where γ is 1.4) is 0.834 for cylindrical shocks [137, 138].

Alternatively, dimensionless time τ and coordinates ξ are defined as

$$\tau = \frac{a_0 t}{R_0} \quad \& \quad \xi = \frac{R_0 - R_s}{R_0} \tag{5.2}$$

where t is the time (taken as zero at the instant of collapse and negative in the process of convergence) and a_0 is the sound speed in the undisturbed fluid. $\xi = 1$ represents the center of implosion. The trajectories of the converging cylindrical shock waves are then given by

$$\xi = 1 - A\left(-\tau\right)^{\alpha} \tag{5.3}$$

where A is a constant and α is the similarity exponent (as described above).

These theoretical classical self-similar type solutions for the propagation of converging cylindrical shock waves are only valid for the final phases of collapse, where the shock front can be assumed to be of infinite strength. Matsuo obtained a global solution, that is a solution which describes the whole history of the fluid motion from the initial stage near the wall to the convergence near the axis [139]. Perry and Kantrowitz were the first to experimentally produce a converging cylindrical shock generated in shock tube [138]. It has been observed that there is considerable luminescence during the final stages of the shock collapse when moderate strength shock waves with Mach number $M = 1.7$ (Mach number is the ratio of shock velocity to velocity of sound in the undisturbed fluid ahead of the shock) converge at the center. Various methods of producing converging shock waves were proposed and measurements of propagation of shock fronts, pressure and temperature were performed [140].

Takayama and Watanabe also studied the convergence of cylindrical shock waves in shock tubes with an annular section [141, 142]. Typical images are shown in Figure 5-1 for convergence of strong cylindrical shocks with Mach number $M = 2.3$. It was concluded that the converging cylindrical shock waves are always unstable and sensitive to the structure of the annular shock tube [143]. It was also found that for stronger shock waves, the instability pattern became catastrophic at the center of convergence [144]. Some attempts were made to treat the stability of converging shock waves by Fong and Ahlborn [145], Wang [146], and Lazarus [147]. Stability of converging cylindrical shock waves is still one of the unsolved problems of shock wave dynamics associated with shock wave focusing.

Experimental studies have shown that cylindrical converging shock waves first decelerate until they arrive at an intermediate point between the origin and the center of convergence, from that point on they begin to accelerate, and finally, in the very vicinity of the center of convergence, they increase in strength without limit [139, 149]. Numerical simulations have been performed for cylindrical focusing of shock waves by Kelly and Matsuo [150, 151, 152].

Recently, studies on converging shock waves have been revived in order to interpret the shock implosion phenomenon applied to the laser fusion technique. Converging
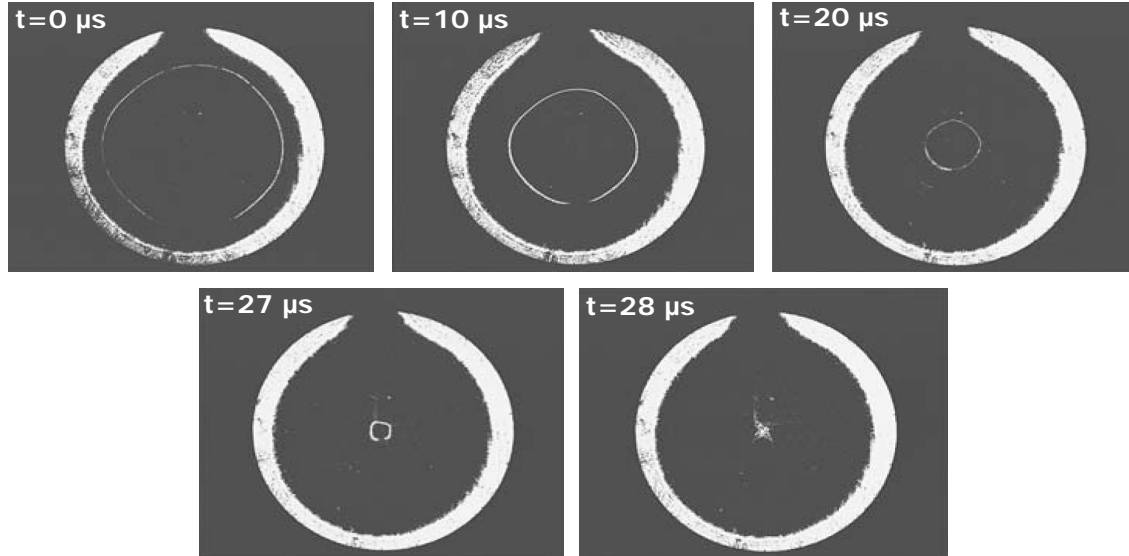
Figure 5-1: Shock wave images (with CCD camera) at different time instants in a gas-filled circular shock tube, depicting the focusing of strong cylindrical shocks with Mach number $M = 2.3$. The visualized area is 70 mm in diameter, and each image is of a different shock wave [148].

cylindrical and spherical shock waves can produce high temperatures, pressures and densities at the center of convergence [153]. This feature in connection with various technological applications mentioned at the beginning of this section is one of the main reasons for continuing interest in the problem of shock focusing. The highly nonlinear nature of the process still presents a major challenge to its study.

The application of a laser to excite shock waves has considerably widened the possibilities to study dynamic properties of materials. It is necessary to obtain real-time information of matter under shock compression in order to understand shock-induced phenomena. I have developed a novel method for direct, real-time optical measurement of mechanical responses to shock loading. The method may be applied to individual material components of complex assemblies to assess their intrinsic behavior under extreme conditions and to study the assemblies themselves in order to assess their collective performance. This chapter presents a unique technique to generate laser-induced in-plane shock waves (or cylindrical shock waves) without any instability. The method is a step forward to understand the nonlinear propagation of converging and focusing shock waves. This all-optical characterization uniquely

extracts relevant information during the time materials are subjected to an ultrafast shock at hyperballistic strain rates.

5.2 Experimental Approach

An entirely new approach to optical shock generation and observation has been developed and demonstrated successfully, that alleviates the problems associated with "front-back"configuration as mentioned in the previous chapter. There are three main components – a "sandwich"sample structure (to launch in-plane propagating shock waves), an axicon-lens optical arrangement (to generate cylindrical geometry), and the use of nanoparticles (to create miniature explosions) in the sample. Each of these will be discussed in detail in this section.

5.2.1 The Sandwich Structure - Planar Shock Propagation

In almost all laser shock research conducted to date, an intense laser pulse irradiates a thin layer of material (typically aluminum) which, through ablation or chemical decomposition, acts like a shock transducer and launches a shock pulse into an underlying material layer or substrate that includes the sample of interest [53]. The shocked sample is typically probed optically from the opposite side as shown in Figure 5-2 (A). In most cases, interferometric measurements are performed to characterize the time-dependent shock amplitude profile, from which the shock pressure can be inferred. This "front-back"approach - shock initiation at the back of the sample and measurement of the shock wave and its effects at the front - poses key limitations that have limited direct spectroscopic characterization of sample responses to laser-induced shock loading [124].

A novel approach has been devised that addresses the problems associated with the "front-back"configuration for spectroscopic measurements of shocked samples. The new approach also opens up new possibilities for control over the shock parameters and for a wide range of additional measurements of shock propagation and sample responses to it. In this approach, the shock wave propagates laterally in the plane
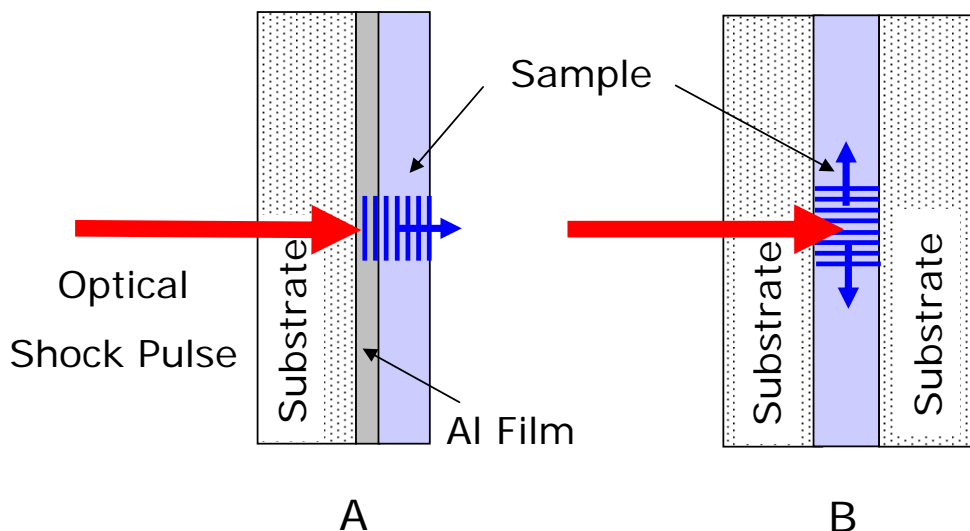
Figure 5-2: (A) Laser shock measurement using conventional **"front-back"** approach. An intense laser "shock"pulse (shown with red arrow) irradiates a thin layer at the back of the sample assembly to generate a shock wave (shown with blue arrow) that propagates through-plane into the polymer sample layer of interest. The shock response is probed from the front, typically through interferometric measurements. (B) Novel method of laser shock generation using a **"sandwich"** approach. The impedance mismatch between the stiff substrates and the thin sample layer confines a shock wave laterally in-plane of the sample (perpendicular to the direction of the optical beam). This approach opens up new possibilities for controlling the shock parameters and for a wide range of spectroscopic measurements of shock propagation and sample response.

of the sample (perpendicular to the direction of the optical shock pulse) rather than through the sample plane (parallel to the direction of the optical shock pulse), as shown in Figure 5-2 (B). The sample assembly includes the liquid or polymer sample layer sandwiched between two transparent glass or sapphire windows, with no need for an opaque shock layer or other components. The shock wave is generated directly within the liquid or polymer sample layer. In our case, the intense shock pulse is focused into a ring pattern (using an axicon-lens arrangement, as discussed in the next section) at the sample, where it is absorbed by aluminum or carbon nanoparticles that are dispersed within the irradiated region of the liquid or polymer sample layer. This interaction results in the rapid heating and explosion of the nanoparticles, launching a shock wave that propagates laterally away from the irradiated region and toward a well defined region where the measurements are made.

Shock-induced changes in the acoustic properties can reveal the time-dependent mechanical and viscoelastic responses of the sample to shock loading. In the new geometry, the measurement is not disrupted by the destruction of the sample region that is irradiated by the shock pulse. The shock wave duration is given by the temporal and spatial characteristics of the shock excitation process, and can easily be extended to many nanoseconds so that real-time measurements including visible, infrared (IR), and terahertz (THz) spectroscopy of sample electronic and vibrational modes can be conducted to determine both molecular and collective material responses to shock. The shock profile can be visualized interferometrically to characterize shock propagation as well as shock-induced sample responses. The optical configuration and sample geometry make shock wave formation and propagation directly accessible to optical imaging and spectroscopic probes with wavelengths ranging from the UV to far-IR.

5.2.2 The Axicon-Lens Arrangement - Ring Shock

Traditionally, a converging wave is generated either by a spherical piston moving into a gas, imparting to it a certain amount of energy, or by an instantaneous release of energy (explosive) on a rigid cylindrical wall, respectively. For laser generation of cylindrical converging shock waves, an axicon and a lens can be combined to form an optical system producing a ring-shaped pattern [154, 155].

The propagation of a collimated beam through a lens-axicon doublet is depicted in Figure 5-3. The radius of the focal ring R and the width of the ring pattern Δ are given by the equations

$$R = (n-1)\alpha F \tag{5.4}$$

$$\Delta = 3.3 \frac{\lambda F}{2\pi a} \tag{5.5}$$

where F is the focal length of the lens, α is the angle of the axicon, n is the refractive index of the axicon, a is the FWHM radius of the input beam (or spot size) and λ is the wavelength of the laser pulse.
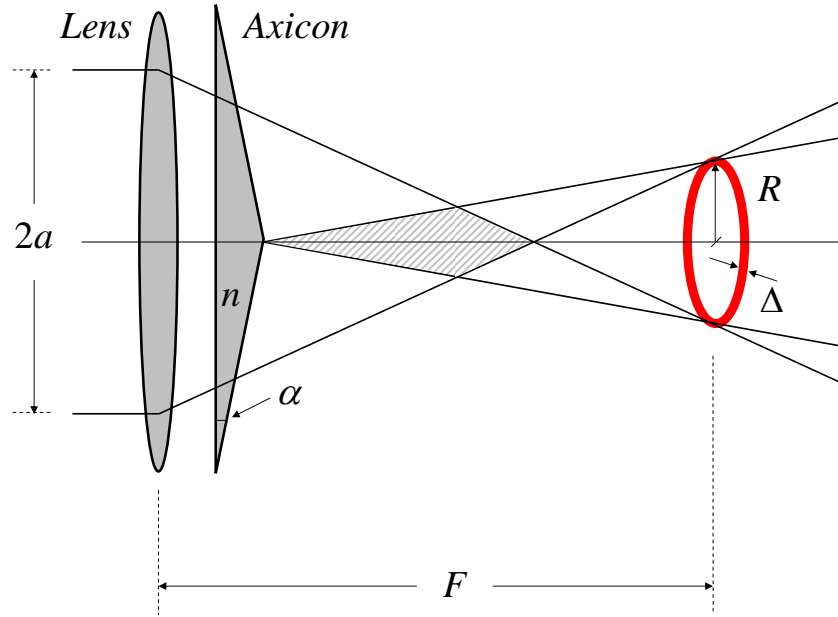
Figure 5-3: Path of the collimated light beam for a lens-axicon (convergent) combination with angle α and refractive index n to form a ring-shaped pattern (shown in red color). The values of R and Δ are calculated using equations 5.4 and 5.5. The shaded region between the axicon and focal ring pattern is a dark region.

5.2.3 The Laser Shock Generation - Use of Nanoparticles

Nanomaterials offer the possibility of faster energy release, more complete combustion and greater control over performance than organic dyes or other nonreactive materials that absorb the pump laser light. The nanoparticle absorption is generally similar to the spectra of bulk materials, but the absorption strength is size-dependent and the response can be up to ten times more intense [156]. Nanoparticles including carbon black and nanometric aluminum can be heated almost adiabatically with shorter duration (< 1 ns) laser pulses, allowing nanoparticles to temporarily become much hotter than their surroundings [157, 158]. These nanometer hot spots (10^4 - 10^6 K) can result in efficient ablation as a result of the combined action of a large number of tiny powerful nanoexplosions.

Mechanism of Shock Generation in Nanoparticles

Typically, nanoparticles are chosen to absorb significant amounts of energy from the laser pulse, while the matrix material is transparent to the excitation wavelength. The

laser heats each nanoparticle uniformly throughout its bulk because the optical penetration depth exceeds the particle size and in any event thermal conduction within the nanoparticle is faster than the laser pulse duration [159]. Thus, the nanoparticles are flash heated past their vaporization temperature almost adiabatically and isochorically by the picosecond laser pulse. The energy in the hot vapor (hydrodynamic expansion) includes a thermochemical contribution from the energy released by ultrafast oxidation and creates a hot spot of high pressure gas that drives a spherically expanding shock wave through the surrounding medium. This combination of laser and chemical energy fuels the expansion of a spherical shock front into the surrounding medium [160]. For picosecond time-scale heating, the optical pulse duration is shorter than the characteristic time for material pressure relaxation, producing a sudden jump in both temperature and pressure. The mechanism of pressure generation is a temporary frustration of thermal expansion, termed thermophysical pressure generation [161].

5.3 Material System

This work will mainly focus on the study of converging shock waves in colloidal solutions of carbon nanoparticles in water (Ink). The commercial brand of ink used is Encre de Chine (China Black Ink, Majuscule). The ink is diluted 10 times with distilled water so that nanoparticle loading is around 2 wt% and the acoustic properties of the system are close to those of pure water.

There are a number of studies on shock wave propagation in water and so its properties are well documented [162]. Water has several exceptional physical properties. It has a large slope in its shock velocity-particle velocity (U_s-U_p) Hugoniot curve, indicating a very strong nonlinearity in its mechanical properties with increasing amplitude of the shock wave pressure [163]. Shockwave behavior as well as the acoustical properties of water have long been studied by various researchers [164, 165]. Moreover, properties of biological tissues are commonly assumed to have a close resemblance to those of water. Water is also known to undergo various phase transformations un-

der compression even at low pressure, around 2 GPa [166]. Measurement of shock velocity in water is of prime importance for determining scaling laws of underwater explosions, the shock wave attenuation in water, the equation of state of water under dynamic loading, and the yields of both nuclear as well as chemical explosions.

The near-IR pulse is absorbed only by carbon nanoparticles because water is transparent in this regime. There are three distinct time scales for heat flow: the time for heat to spread uniformly throughout the nanoparticle (100 ps), the time for heat to spread through the water (a few microseconds), and the time for heat to escape into the glass substrate (70 μs). Thus a 300 ps laser pulse heats the nanoparticles almost uniformly [161].

5.3.1 Characterization of Nanoparticle Solution

Determination of the optical properties of ink is an important task [167, 168, 169]. The amount of energy absorbed by nanoparticle solutions is described by the absorption coefficient α as determined by UV-VIS spectra shown in Figure 5-4. The spectrum was collected using a Cary 6000i UV-VIS-NIR Spectrophotometer (Varian Inc.). The solution was optically thin with nanoparticle loading around 2 wt%, thus Beer's law was obeyed. The absorption coefficient α at the excitation wavelength (800 nm) is 0.176 μm^{-1} and hence, 90% of the incident fluence is absorbed by a 5 μm thick sample layer.

The cluster size (or aggregation) and size distribution of the ink particles was determined by electron microscopy and zeta potential respectively. A typical SEM image of the carbon nanoparticles is presented in Figure 5-5. For SEM imaging, each dispersed sample was deposited onto a silicon wafer and coated with less than 3 nm of sputtered gold-palladium. A JSM-6700F Field Emission Scanning Electron Microscope (JEOL Ltd.) was used for imaging in secondary electron mode. A Zeta potential analyzer (Zeta PALS, Brookhaven Instruments Corporation), which is based on the principle of dynamic light scattering, was used to extract the size distribution of the particles in solution/suspension which ranges from 45 to 75 nm (with mean particle size around 55 nm) as shown in Figure 5-4. No significant variation in particle
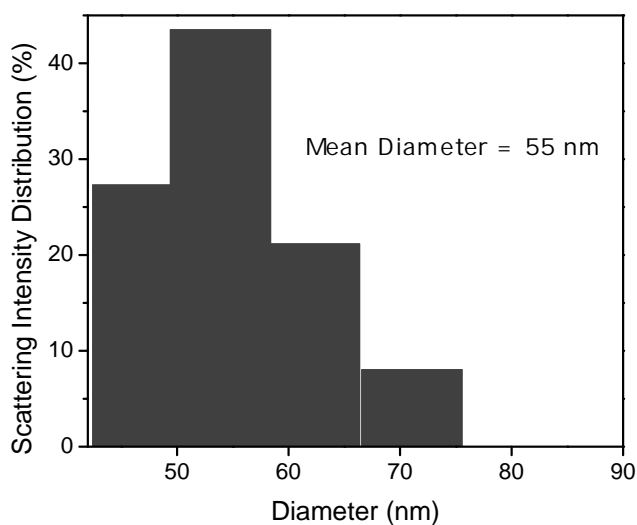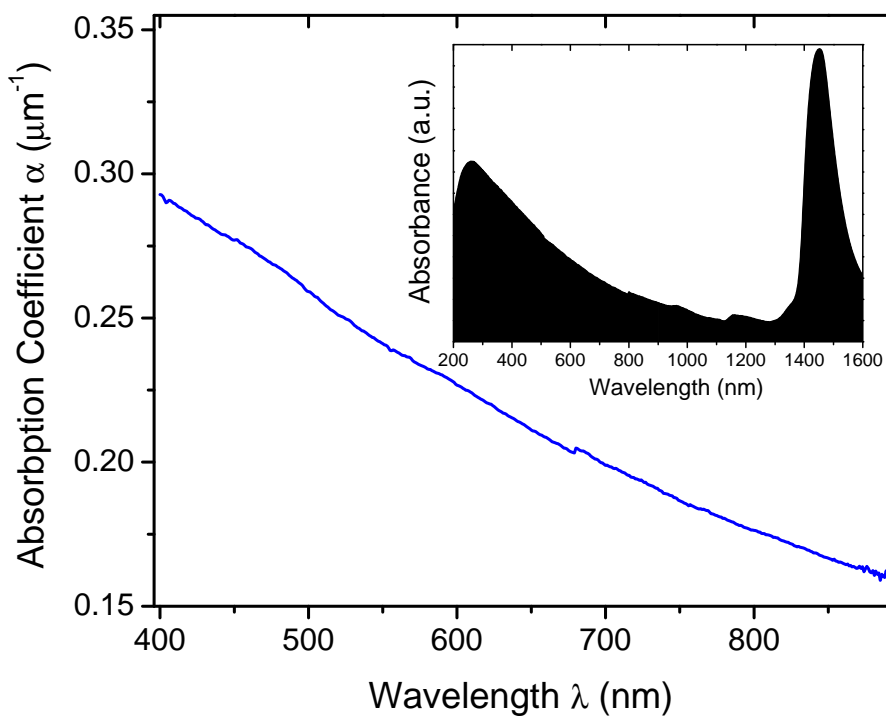
Figure 5-4: (Top) Visible absorption spectra of carbon nanoparticles in water under normal conditions. The inset shows UV-VIS-NIR absorbance spectra of the diluted solution in the wavelength range from 200 to 1600 nm. The peak at 1450 nm is due to molecular vibrations of water. (Bottom) Zeta potential analysis of carbon nanoparticles dispersion in water to determine particle size distribution. The vertical axis represents scattering intensity distribution (or frequency distribution of nanoparticles in percentage). The mean size of particles is determined by number average methodology.
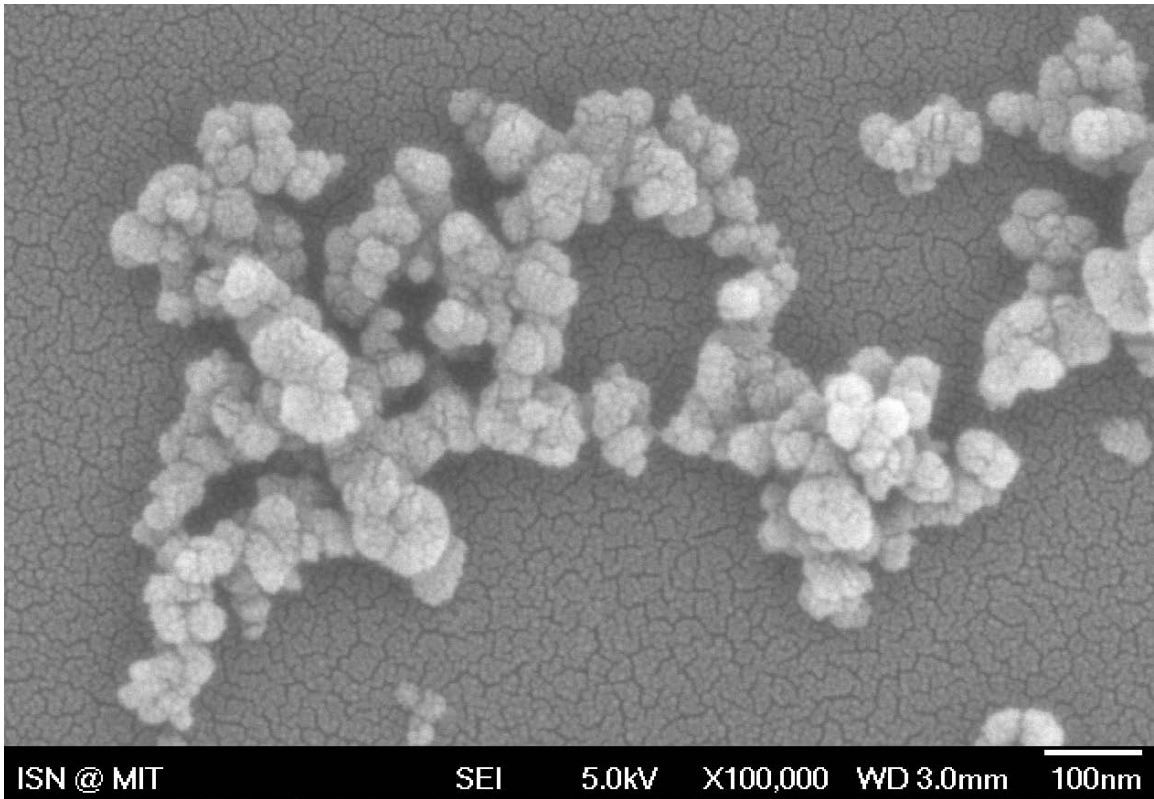
Figure 5-5: SEM image of carbon nanoparticles from a diluted dispersion in water. SEM imaging of carbon nanoparticles deposited from aqueous dispersions provided information about particle and cluster size. The background represents polycrystalline gold-palladium sputtered on a silicon wafer, used for preparing the SEM sample.

dispersion has been observed over a period of several weeks for a given ink solution.

5.4 Experimental Apparatus

5.4.1 Sample Configuration

The sample consisted of a 5 μm thick water layer with embedded carbon nanoparticles that was sandwiched between two 100 μm glass substrates using a polymer spacer, as shown in Figure 5-6. The shock pulse was focused to make a 200 μm diameter ring pattern using a lens and axicon arrangement. The shock rise time and duration were given by the spatial distribution of shock pulse light. A sharp edge (several microns) will yield a fairly sudden rise (about 1 ns) while a broad width yields a total shock duration of tens of nanoseconds. The Gaussian spatial profile of optical shock

pulse can be converted to the temporal profile through the speed of sound in water (~ 1.45 km/s). For example, a 10 μm FWHM spatial distribution will give around 7 ns FWHM temporal profile. The total shock duration depends on the sharpness of edge as well as the spatial profile. Each irradiated sample volume of 10^4 μm^3 (typically 200 μm ring diameter, 10 μm width and 5 μm thickness) contains many nanoparticles. Each particle sends a shock wave radiating outward spherically, but the large number of particles in the irradiated region ensures that the overall (far field) shock wave follows the geometric pattern of the pump light.

5.4.2   Optical Setup

An uncompressed output of an amplified femtosecond Quantronix laser with 800 nm wavelength, varying pulse energies ranging from 0 - 4 mJ and 300 ps pulse duration is directed onto an axicon (Doric Lenses Inc., $\alpha = 0.5°$) and then focused by a lens with a focal length F of 3 cm into a ring (or circle) between the sandwich structure, inside the liquid layer. Using equations 5.4 and 5.5 and considering refraction phenomena (beam has to go through 100 μm glass before making ring-pattern), the lens-axicon arrangement provided the ring in the liquid layer with a 200 μm diameter and a width of ~ 10 μm. The actual size and width of the ring was confirmed using a laser beam profiler (LBP-2-USB, Newport Corporation). A typical result is shown in inset of Figure 5-7.

A variety of techniques such as high-speed framing, streak cameras, shadowgraphs and Schlieren photographs can used to image the propagation of shock waves in various media. A charge-coupled device (CCD) camera has been used for shock wave imaging in the current experiments. The CCD camera (Cohu Inc., 7700 Series Progressive Scan Camera, 10 - bit, 1004 × 1004 pixels, pixel size: 7.4 μm × 7.4 μm) is placed so as to image the sample plane using a conventional two lens imaging system. A femtosecond laser operated on a single shot basis, with fundamental wavelength of 800 nm and 200 fs long light pulses was used as the light source for the imaging optics. This beam was frequency doubled with a 500 μm thick BBO crystal to produce a 400 nm beam to be used a probe. The camera was triggered by the same signal
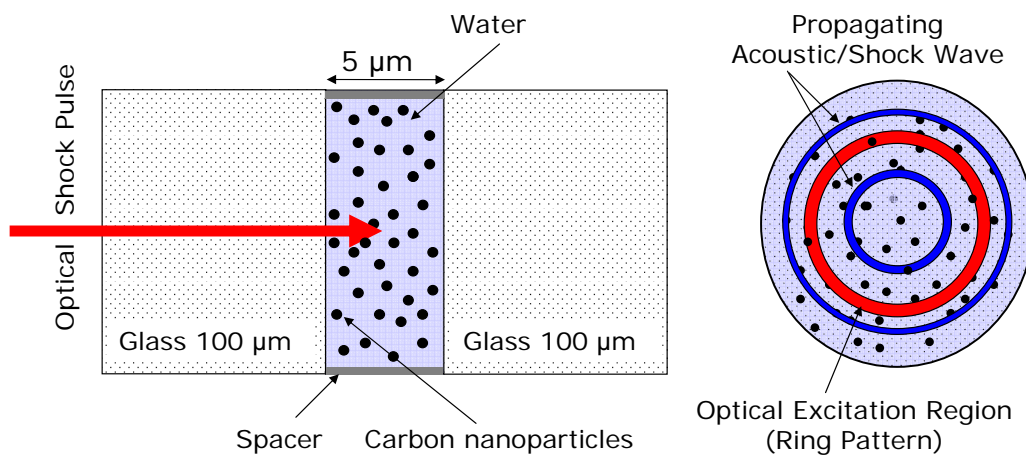
Figure 5-6: Schematic illustration of the sample geometry showing side view (Left) and cross-sectional view (Right) where the shock wave propagates laterally in the plane of the sample (not to scale). The shock wave is generated directly in the water layer in the form of the ring pattern using a lens and an axicon arrangement. The ring irradiation pattern (as shown in red) launches a response that propagates laterally within the water layer both inwards and outwards (as shown in blue rings). The outward propagating ring diverges and there is a decrease in its amplitude. The inward propagating ring converges and creates a shock of higher amplitude at the center of the ring. Many types of real-time measurements of the shock wave and the sample responses to it are possible since shock generation and propagation and the sample responses to shock are in direct view at all times.

as the optical shock pulse. A signal generator (Stanford Research System, Model DG535) was used to control the shutter for optical pulses (both excitation and probe beams) and the CCD camera to enable exposure of the shock wave at a predetermined time in the test specimen. The optical path of the probe beam was varied using an optical delay so that the time history of the shock event could be created. Shock imaging could be realized by the change in optical path length at the propagating shock wave due to the change in the refractive index induced in the sample with shock pressure.

Figure 5-7 illustrates the complete experimental set-up detailing the focusing shock generation and imaging. An imaging pulse with 400 nm wavelength was used to build a **Mach-Zehnder interferometer** (imaging and reference pulses make an optical interference pattern) so that the shock phenomena could be imaged on a CCD. The positions of lenses were optimized for sharp imaging of both converging and diverging shock waves. A 400 nm bandpass filter together with some neutral density filters was used to block the residual or scattered 800 nm light in the probe beam and the fluorescence and white light generated during the pumping from entering the CCD camera. The images were recorded at different times by varying the time delay between the arrival of the optical shock pulse and the imaging pulse at the sample as shown in Figures 5-8, 5-9, and 5-10.

5.5 Results & Image Analysis

5.5.1 Shock Visualization

The first measurements of liquid water samples under shock loading (converging in-plane shock propagation) were successfully conducted in the new experimental configuration as shown in Figure 5-7. The present imaging setup allows one exposure at each time delay, thus a time history is builtup by single exposures taken at different time delays. For each experiment times t_1 and t_2 when the shock wave and imaging pulse arrives at the sample respectively are recorded using a photodiode.
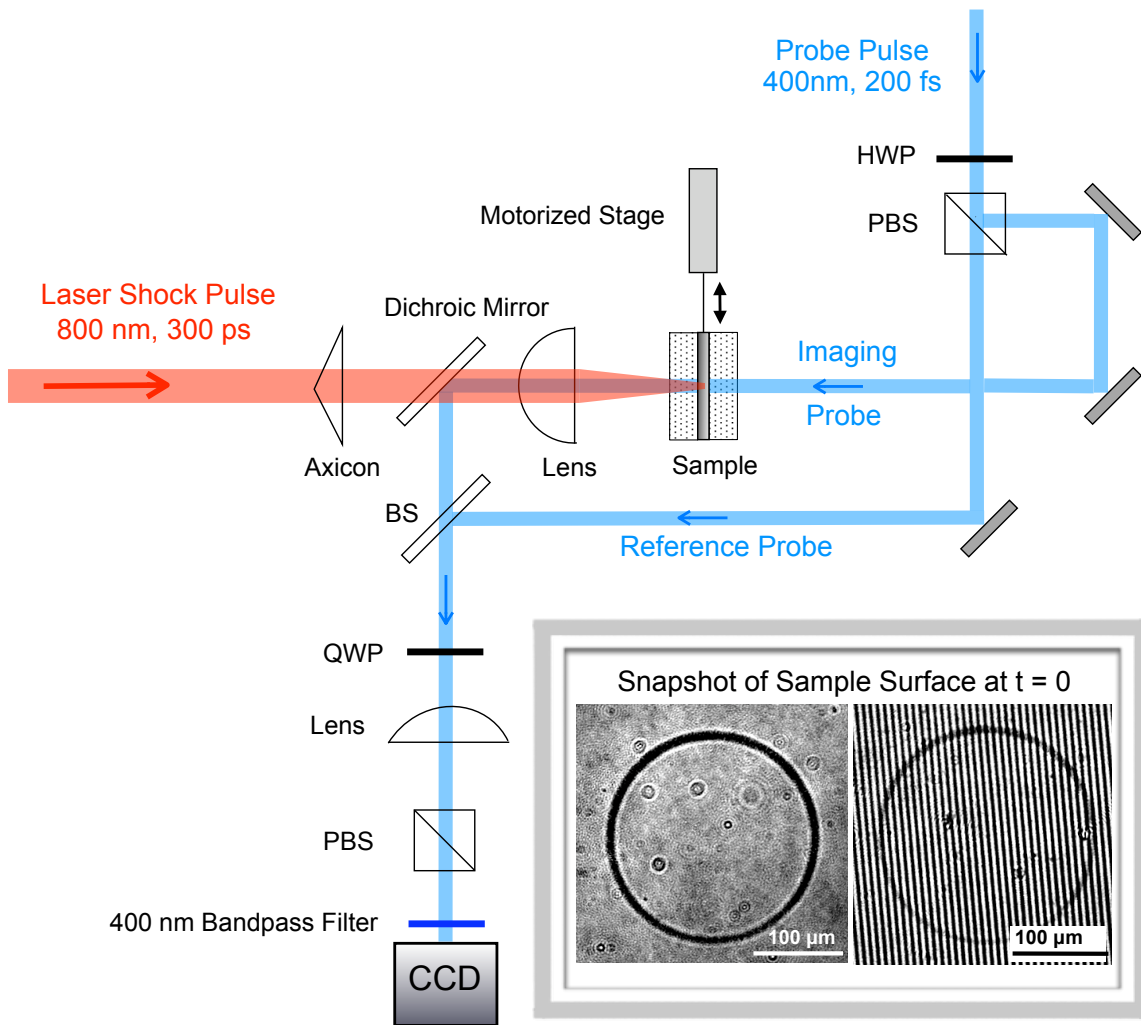
Figure 5-7: Schematic illustration of the experimental set-up showing focusing shock generation and imaging. PBS, QWP, HWP and BS stand for polarizing beamsplitter cube, quarter-wave plate, half-wave plate, and plate beamsplitter respectively. The shock wave generated directly in the sample layer propagates laterally within the sample layer, and the Mach-Zehnder interferometer is used as a probing tool to record images on the CCD. The shock position is evaluated from CCD images which are produced through illumination by the frequency-doubled laser pulse. The optical shock pulse (wavelength 800 nm) is shown in red and the imaging pulse (wavelength 400 nm) is shown in blue color. The inset shows both normal and interferometric images of ringpatterns generated within a 5 μm water layer (with carbon nanoparticles) sandwiched between two 100 μm thick glass substrates. The incidence energy of the optical laser shock pulse can be tuned from 0-4 mJ. After each CCD image is recorded at a specific time delay, the target is shifted to a new position with a fresh area before the next image is taken. By changing the optical path of the probe beam with an optical delay, I can create a time history from 0 to 65 ns.

The recorded images can be used to extract propagation distance and together with time delay $\Delta t = (t_2 - t_1)$, I can easily determine the shock speed U_s. Figure 5-8 shows a typical sequence of time-resolved CCD images of shock wave propagation after a 300 ps laser pulse irradiates the sample layer.

These measurements have a high repeatability, giving a low uncertainty level for the extracted shock speeds (i.e. less than 2.5%). To estimate the uncertainty in the shock wave position, the time delay was set to $\Delta t = 25.3$ ns and a series of runs were performed for the same sample at different locations. The possible sources of errors include fluctuations in the density of nanoparticles and variations in the light pulse energy from the laser.

The CCD images in Figures 5-8 and 5-9 clearly demonstrate how the waves propagate in the inner and outer rings as a function of time in the linear acoustic response limit when very low input laser pulse energy (0.08 mJ) is imparted. Figure 5-10 shows the time history of wave propagation in the shock regime with the input energy increased to 0.33 mJ. The inner ring reaches the center of convergence in less than 40 ns as compared to around 65 ns in the acoustic limit.
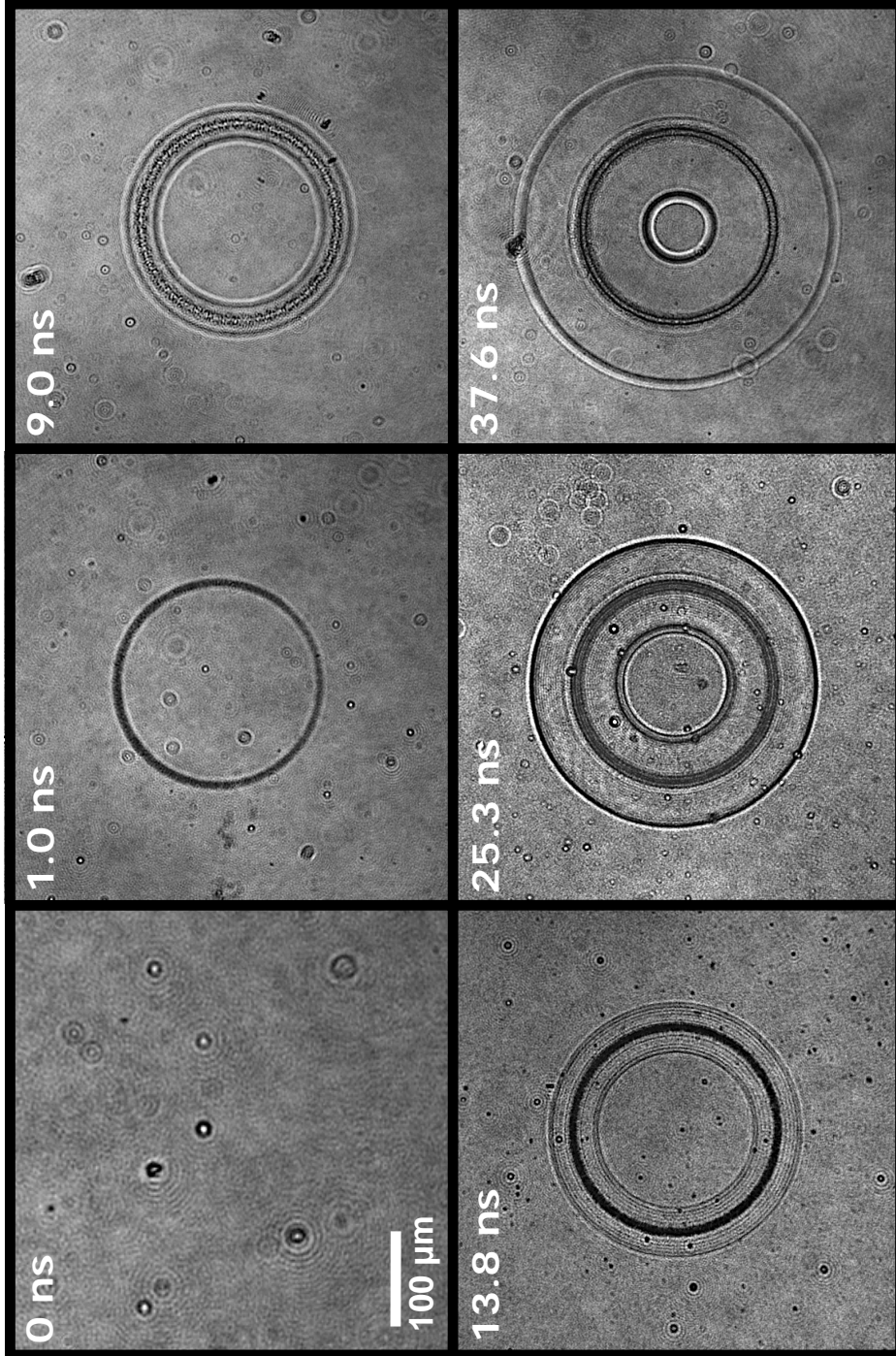
Figure 5-8: Time-resolved CCD images after target was irradiated by an optical shock pulse. Raw images recorded on the CCD showing the time history at the indicated time delays - 0 ns, 1.0 ns, 9.0 ns, 13.8 ns, 25.3 ns, and 37.6 ns during which acoustic wave propagation occurred in the water layer. The images were recorded on a single-shot basis from different shocked regions of the sample since each sample region that was irradiated by laser shock pulse was permanently damaged. The input optical shock pulse energy was 0.08 mJ.
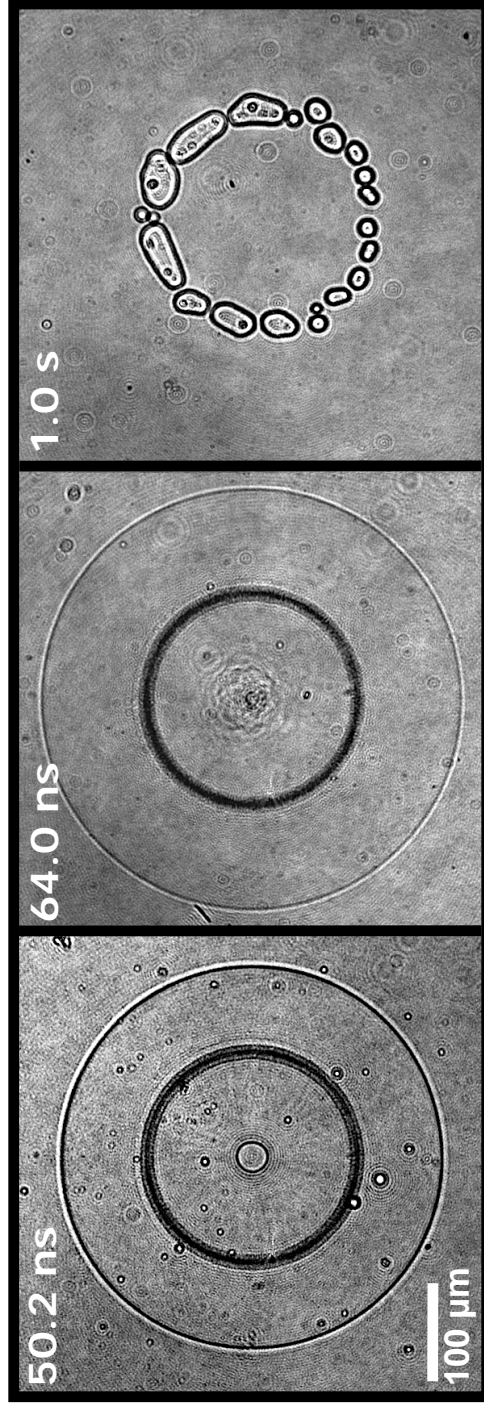
Figure 5-9: Raw images recorded on the CCD showing the time history at 50.2 ns, 64.0 ns, and 1.0 s after initiation of converging acoustic wave propagation in the water layer. It is clearly evident that the inward propagating wave converges at the center. The input optical shock pulse energy was 0.08 mJ.
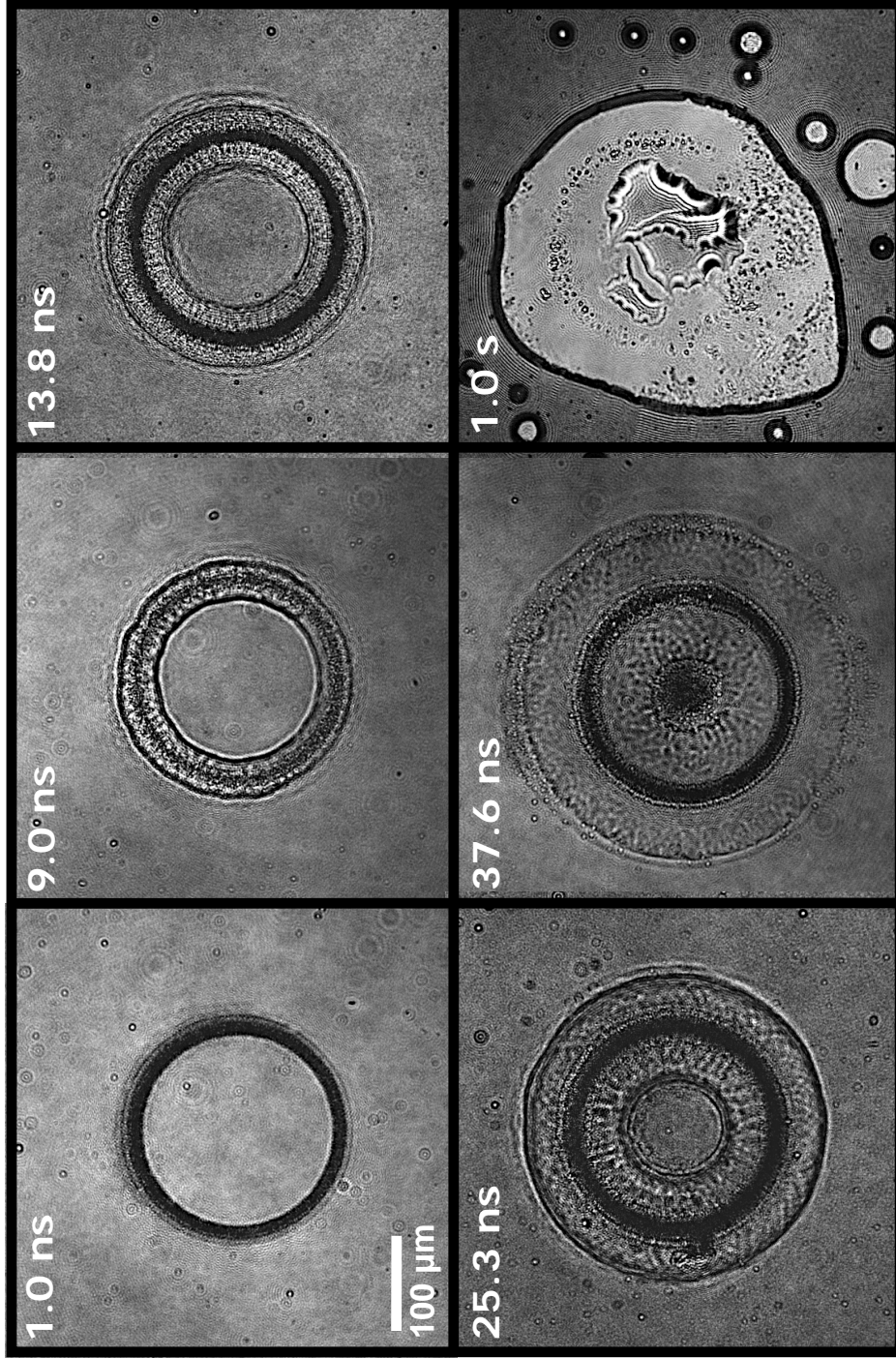
Figure 5-10: Raw images recorded on the CCD showing the time history at 1.0 ns, 9.0 ns, 13.8 ns, 25.3 ns, 37.6 ns, and 1.0 s after initiation of ring shock propagation in the water layer. The input optical shock pulse energy was 0.33 mJ. There is bubble formation both at the shocked region and center of convergence as clearly seen in the CCD image taken at 1.0 s.

5.5.2 Interferometric Shock Visualization

Interferometric images are better for quantitative data analysis as I can accurately measure the inner and outer shock wave positions through the induced phase shifts. Figure 5-11 shows a typical set of interferometric images for two different time delays of 13.8 ns and 25.3 ns at two different input energies of 0.08 mJ and 0.33 mJ for the optical shock pulse in liquid water. There is a clear difference in the distance propagated by the inner ring for the two different energies because the shock wave velocity increases with increasing shock pressure. The distances traveled by the inner and outer rings versus the time delay at two different input optical pulse energies (i.e. 0.08 mJ and 0.33 mJ) are plotted in Figure 5-12. It is evident that the inner ring is propagating greater distances with increasing shock laser pulse energy at any selected time delay (i.e. shock velocity is increasing). On the other hand, the outer ring propagates the same distance at different time delays irrespective of the input pulse energy.

CCD images at different time delays after a 300 ps laser pulse irradiated the sample layer were recorded with a time-resolved Mach-Zehnder interferometer. It was convenient to study the pressure-dependent variation of shock wave velocity in water by recording interferometric CCD images for a fixed time delay with different input pulse energies. Figure 5-13 shows the effect of input optical shock pulse energy at a fixed time delay of 25.3 ns. The inner ring gets smaller in diameter with increasing shock pulse energy. In other words, the inner ring is propagating at faster speeds with increased shock pulse energies from 0.33 mJ to 2.0 mJ.

The results for calculated shock wave velocity as a function of input laser pulse energy are depicted in Figure 5-14. The plot shows the average energy calculated as the total distance traveled divided by the time of travel at the latest time measured, neglecting the increase in speed during convergence. There is clear indication that the inner ring is propagating at a much faster speed than the outer ring at all energy settings. It can also be seen that the inner ring propagates at a faster speed as the input pulse energy increases, which is in good agreement with the images shown
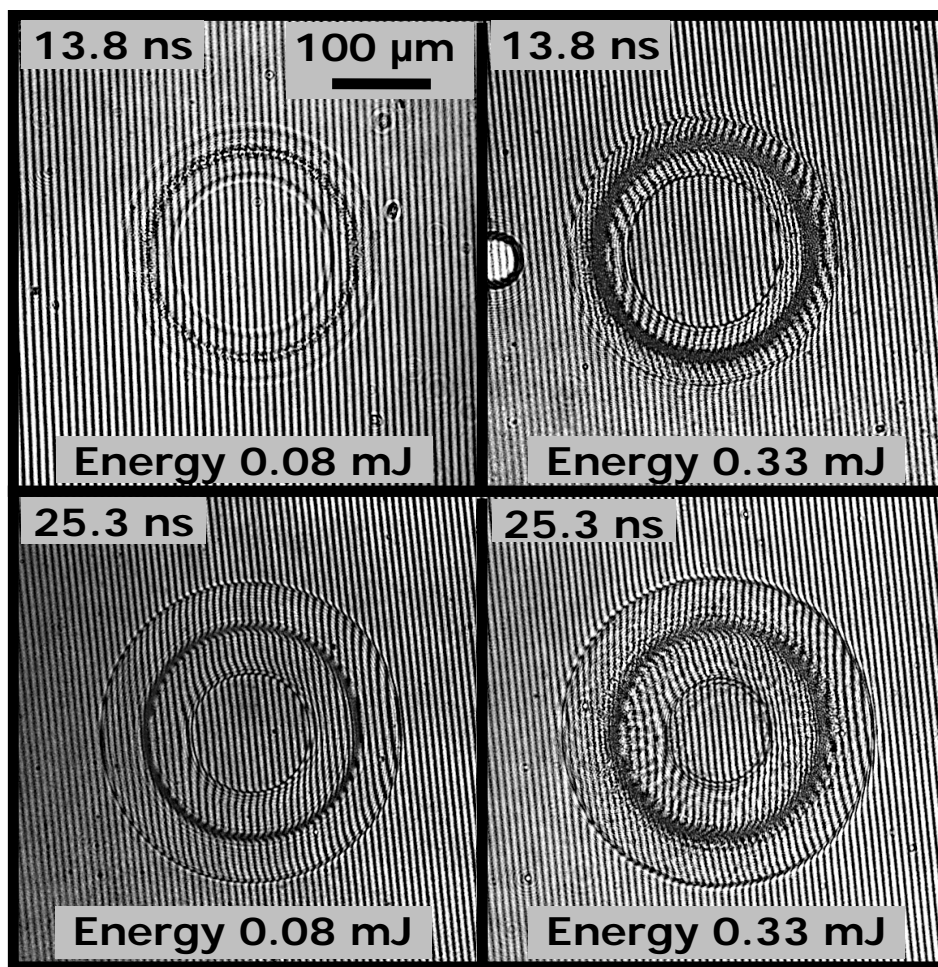
Figure 5-11: Interferometric images showing two different time delays of 13.8 ns and 25.3 ns at two different input energies of 0.08 mJ and 0.33 mJ for the optical shock pulse in liquid water. There is a clear difference in the distance propagated by the inner ring for the two different energies because the shock wave velocity increases with increasing shock pressure.
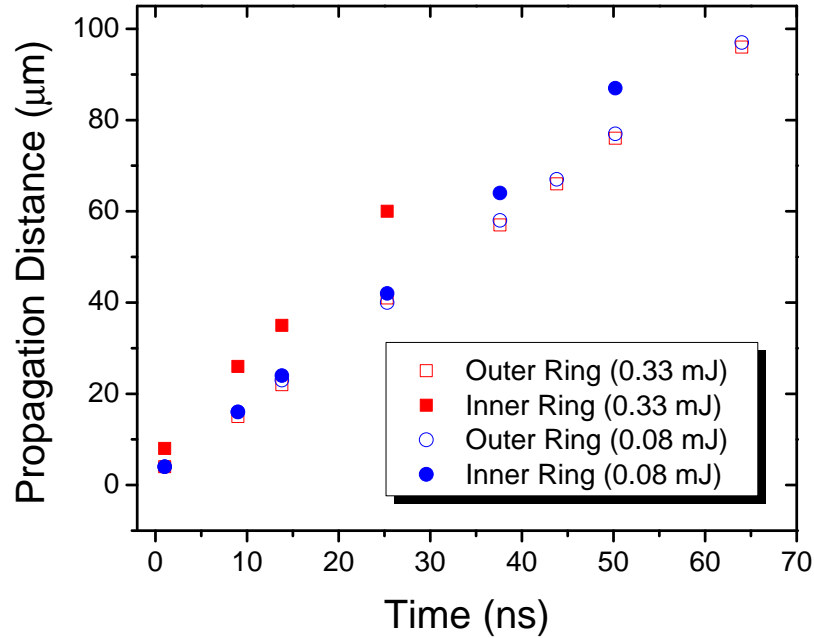
Figure 5-12: Plot of distances traveled by the inner and outer rings as a function of time. It is evident that for any selected delay time, the inner ring that is launched by the higher laser pulse energy propagates farther because of its higher shock pressure.

in Figures 5-11 and 5-13. The plot in Figure 5-15 shows the empirical Hugoniot relationship between shock wave velocity and shock wave pressure in liquid water [170]. For a shock laser pulse energy of 2.0 mJ, the shock pressure of the inner ring at 25.3 ns time delay is around 1.5 GPa. After the high-pressure shock wave in water is generated, the refractive index of the shocked water also increases due to a density increase by shock compression, studied quantitatively through phase analysis of interferometric images.
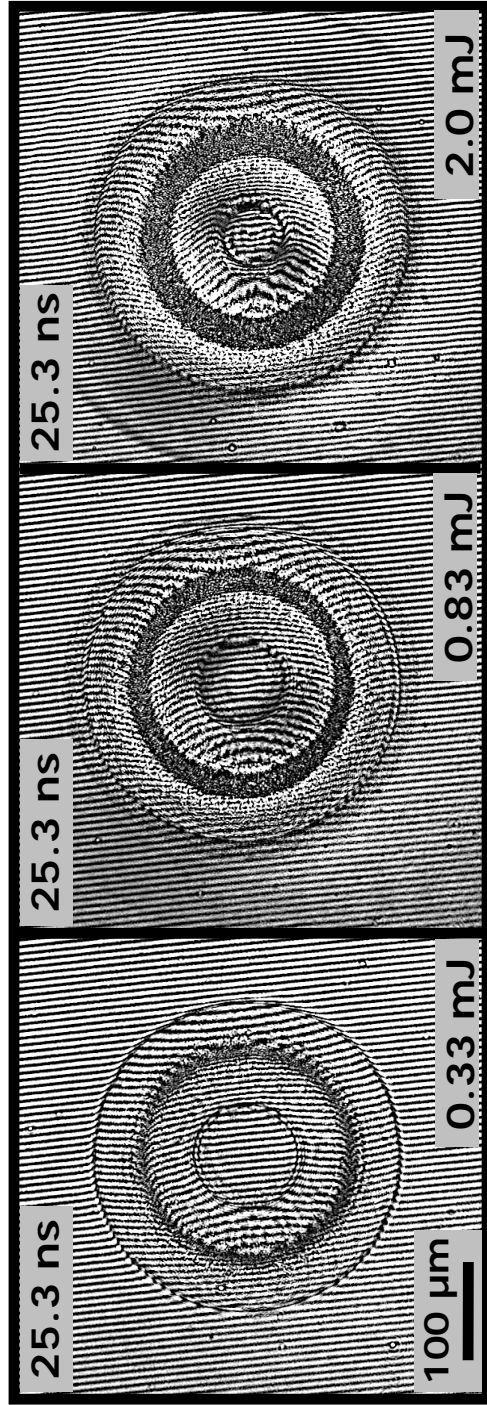
Figure 5-13: Interferometric images showing the effect of input optical shock pulse energy at a fixed time delay of 25.3 ns in liquid water. The inner responses launched by higher-energy pulses have propagated farther toward the center of the ring because they have higher shock pressures and therefore higher speeds.
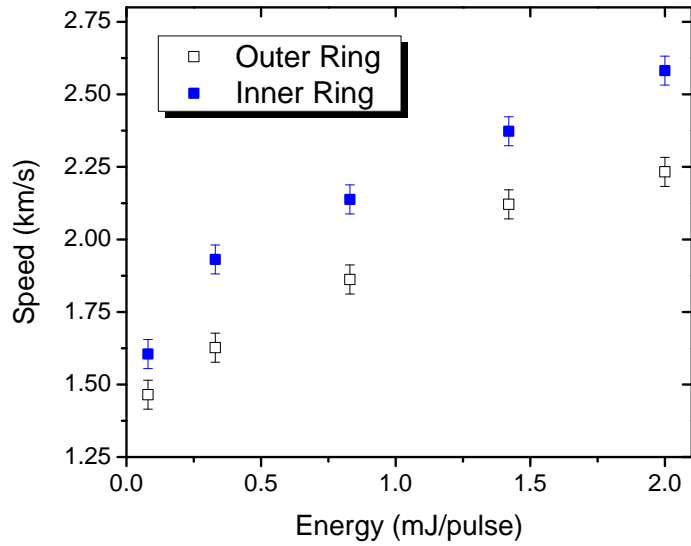
Figure 5-14: Plot of average shock speed in water of the inner and outer rings as a function of input optical pulse energy. There is clear indication that the inner ring is propagating at a much faster speed than the outer ring at all energy settings.

$$P = \rho_0 U_S \frac{U_S - 1.45}{1.99}$$

2mJ, 25.3 ns
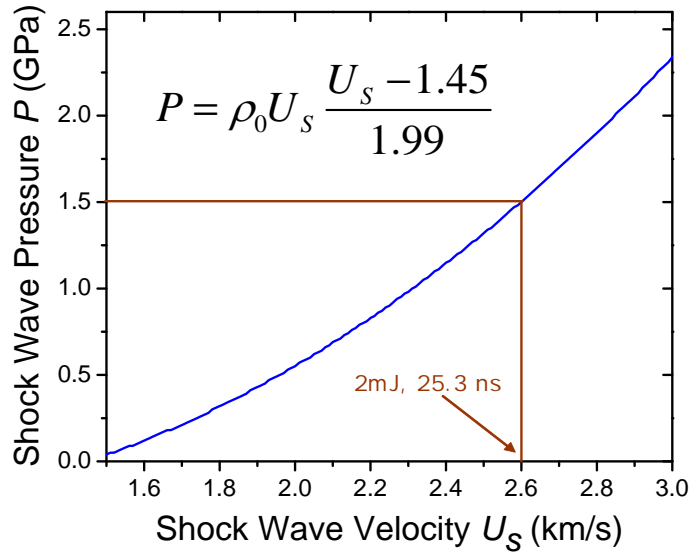
Figure 5-15: Estimate of shock wave pressure in water as a function of shock wave velocity using the empirical Hugoniot relationship relating shock wave speed (U_s in km/s) and shock pressure (P in GPa). ρ_0 is the density of unshocked water (1.00 g/cm^3). The pressure reached for 2.0 mJ pulse energy at a delay of 25.3 ns is around 1.5 GPa. The pressure at the center of the ring will be greater than this value.

The interferograms were analyzed with a 2 D fast Fourier transform (FFT) method as described by Takeda et al. [171]. Figure 5-16 shows the phase shift profile for an interferometric image recorded at 25.3 ns and 0.83 mJ input laser pulse energy (as shown in Figure 5-13). The phase shift was used for measurement of the change in refractive index of water given by

$$\Delta\phi = \frac{2\pi}{\lambda} \ d \ \Delta n \tag{5.6}$$

where ϕ is phase in radians, λ is probe wavelength in microns, d is liquid thickness in microns and n is the refractive index of the liquid layer.

The Gladstone-Dale relation has been used to describe the change in refractive index with the change in density due to shock compression for many materials. The Gladstone-Dale relation [172] can be simply stated as

$$\frac{n-1}{\rho} = constant \tag{5.7}$$

where ρ is density and n is refractive index of the material.

For water, the Gladstone-Dale relationship [173] is given by

$$n = 1.332 + 0.322 \ (\rho - 1) \tag{5.8}$$

Using equations 5.6 and 5.8, change in density can be related to phase shift. In our experiments, $\lambda = 0.4$ μm and $d = 5$ μm, thus for a phase shift of 5 radians (calculated for the inner converging ring from Figure 5-16), the change in refractive index is 0.064 and the change in density is 0.20 g/cm^3. The shock pressure calculated using the Hugoniot curve for water (shown in Figure 5-17) is 0.77 GPa. On the other hand, the pressure reached for 0.83 mJ input laser pulse energy at a delay of 25.3 ns using speed analysis through CCD images (calculated from Figures 5-14 and 5-15) was around 0.73 GPa. The phase analysis yielded pressures in good agreement with those calculated from the shock velocities and the Hugoniot curve.

CCD images were also recorded after the sample was damaged by the convergence
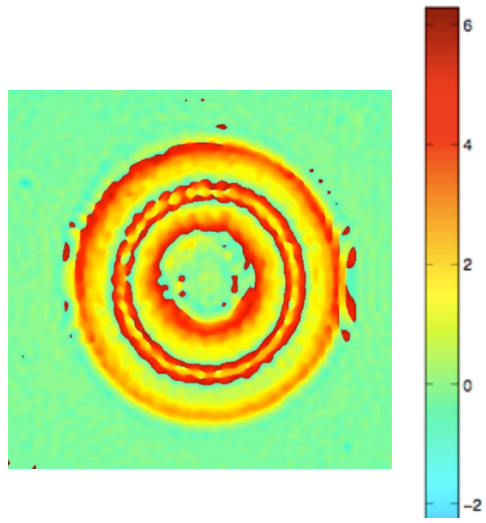
Figure 5-16: Optical phase shift profile calculated from interferogram shown in Figure 5-13 recorded at 25.3 ns and 0.83 mJ input laser pulse energy.
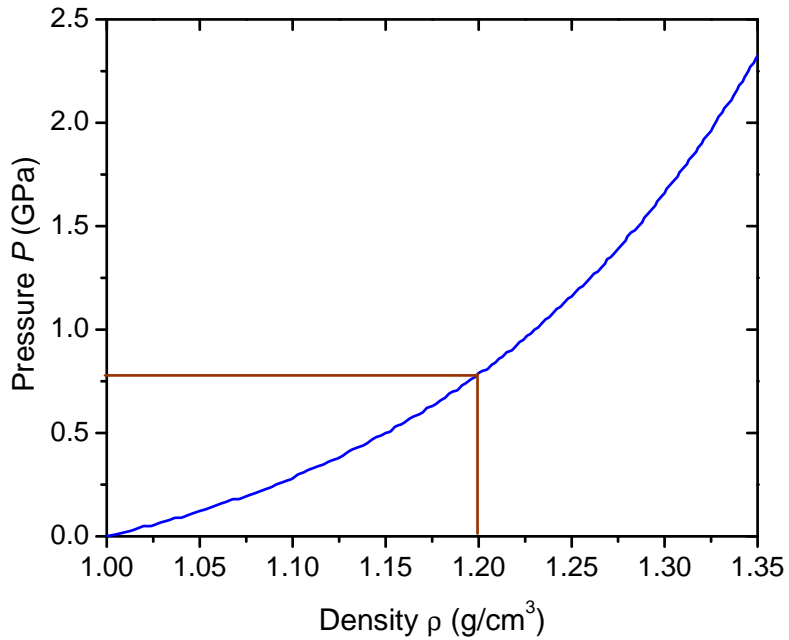
Figure 5-17: Estimate of shock wave pressure (P in GPa) in water as a function of density (ρ in gm/cm^3) using the empirical Hugoniot relationship. The pressure reached for 20% change in density is 0.77 GPa.

of the cylindrical shock shock waves. A typical set of images is shown in Figure 5-18 for the input optical shock pulse energy of 1.5 mJ. There are clear signs of visible damage at the center of convergence and crack formation in the glass substrates.

There are still some phenomena which are not fully understood in the present experiment. A theoretical collaboration with the group of Prof. R. Radovitzky at MIT has begun in order to provide further insight. At high input optical shock pulse energy, Scholte waves [174] at the solid-liquid interface and bulk waves in the glass substrates are experimentally observed, signifying additional components of nonlinear propagation and evolution of shock. The right-most CCD image at input optical shock pulse energy of at 2.0 mJ in Figure 5-13 clearly shows these phenomena. There is a wave propagating outward with a speed higher than 6 km/s indicating bulk wave propagation in glass. There is possibility of mode coupling between Scholte wave and bulk wave in the liquid due to the short shock formation distance and large coherence length of their interaction in our experimental configuration. The role of acoustically induced turbulence in the liquid is also an important factor to consider. It has been reported that focused waves experience some phase change between the waves going into and moving away from the focus. Jen et al. studied the phase variation of focused surface acoustic waves which can provide insight to the shock wave propagation phenomena, especially useful for numerical modeling [175]. The shock waves going toward the focus have a unipolar pulse shape, and waves having passed through the focus and diverging have a bipolar shape with equal positive and negative displacements. Our images do not show clear signatures of shock or acoustic waves emerging from the center, perhaps due to turbulence in the region of convergence.
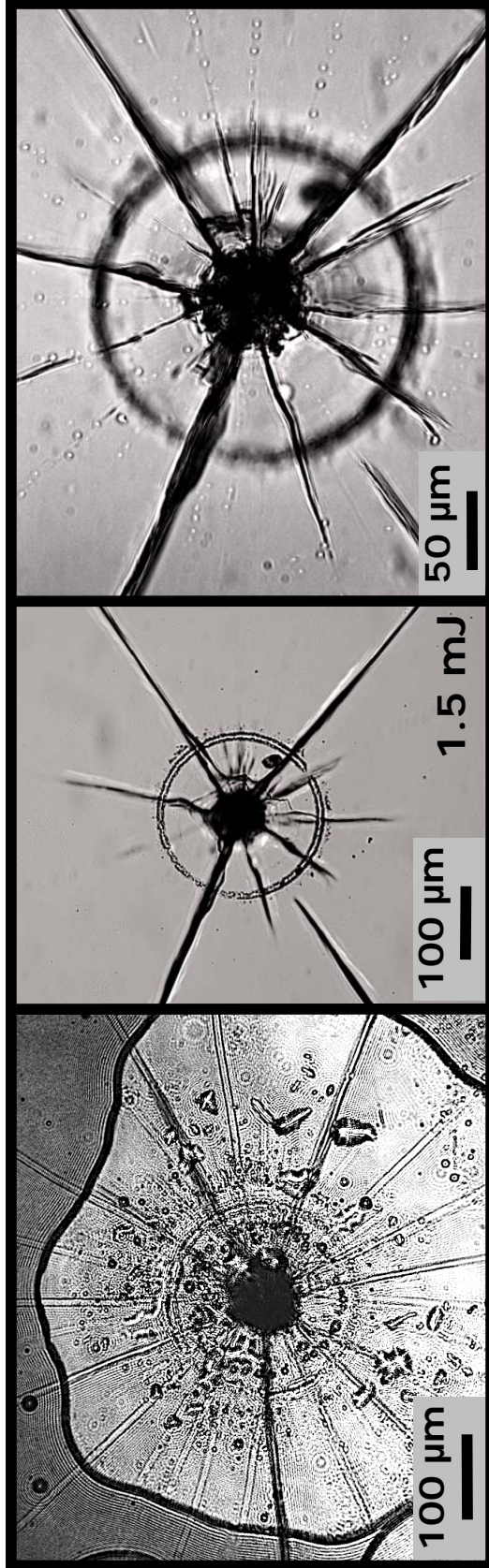
Figure 5-18: Images of shocked regions long after the convergence of cylindrically propagating shock waves has done significant damage at the center of convergence. Cracks are clearly visible and run 500 - 700 μm in length in radial directions. The left image is a CCD image, while the two right-most images are taken using an optical microscope at different magnifications. The input optical shock pulse energy was 1.5 mJ.

5.5.3 Preliminary Study of Complex Samples

The validation of the experimental approach demonstrated here opens the door to study of complex materials and structures. In this section I present preliminary observations of lateral shock propagation in several polymeric and metallic samples. Continued study of complex samples will be the next phase of our ongoing research on shock effects and mitigation. Preliminary observations are presented here in order to illustrate the range of sample possibilities.

5.5.3.1 Shock Studies in Epoxy Nanoframe System[*]

Periodic nanostructures fabricated by interference lithography can be precisely designed to have a specific cell geometry, topology and porosity in contrast to typical stochastic cellular materials.

A relatively new class of cellular materials, holographically defined nanoframes, have been fabricated by light-induced crosslinking of photoresists using a 3D pattern of light intensity produced by the interference of multiple laser beams (interference lithography) [176, 177]. The nanoframe structures show large mechanical energy dissipation/volume (up to 4.5 MJ/m^3), comparable to the highest values achieved in conventional polymer foams but at a far smaller strain. Counter-intuitively, a nanoframe of smaller relative density can dissipate more energy per volume because the geometry of the nanoframe evolves during deformation to engage more of the material in plastic deformation [178].

Thus, nanoframes made by interference lithography may lead to improved mechanical properties beyond specific stiffness including enhanced energy absorption and fracture toughness, both of which are properties in demand to develop smart structures for response to specific stress conditions (e.g. advanced personnel protection armor).

A photo-crosslinkable epoxy resin (SU-8, Microchem) is chosen to fabricate epoxy nanoframes using multiple beam interference lithography [179] because SU-8 allows

---

[*]Done collaboratively with Jae-Hwang Lee in the group of Prof. Edwin L. Thomas
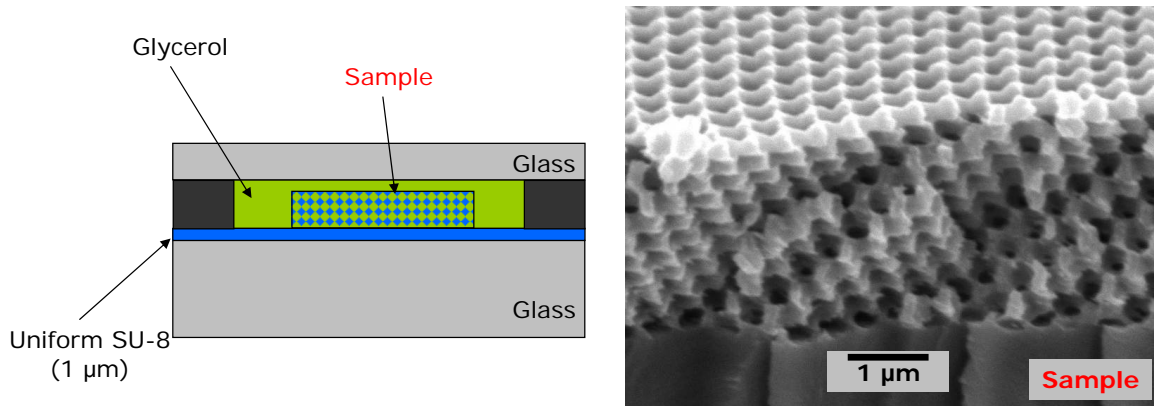
Figure 5-19: (Left) Schematic illustration of the nanoframe structure fabricated by interference lithography to study shock mitigation. A SU-8 monomer is spin-coated onto a pre-crosslinked SU-8 buffer layer film supported by a glass substrate. A 3D latent chemical image is then formed within the top SU-8 layer by interference lithography using four ultraviolet (UV) laser beams ($\lambda = 355$ nm) from a frequency-tripled Nd:YAG laser (Quanta Ray Lab 150, Spectra-Physics). The nanoframe structure is infiltrated with glycerol doped with 2 wt% IR-140 dye so as to absorb the optical excitation energy. (Right) A cross-sectional SEM image of the SU-8 nanoframe structure on a glass substrate.

for a relatively uniform dose to be delivered throughout a relatively thick film due to its very low absorption in the near-UV range. Figure 5-19 shows a schematic of the nanoframe structure with the sample geometry used in the laser shock experiment to investigate the enhanced energy absorption and dissipation effects of the nanostructured material. Preliminary results from the shock experiments are shown in Figures 5-20 and 5-21. Figure 5-21 shows an SEM image of a destroyed nanoframe structure which clearly depicts the extent of damage induced by propagating shock waves as well as the effects of the nanoframe structure in shock mitigation.
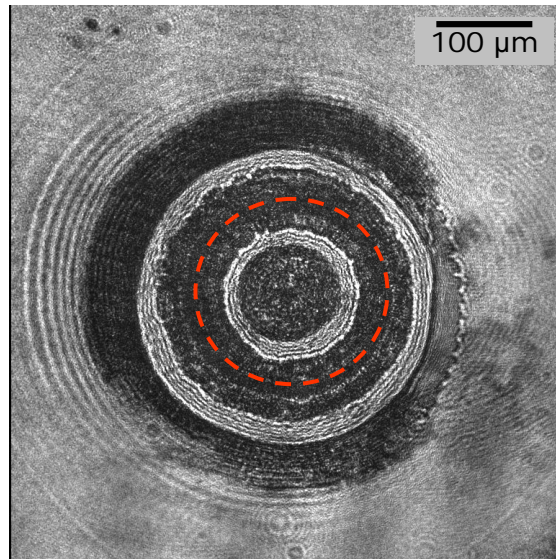
Figure 5-20: CCD image of shock-wave propagation through a glycerol-nanoframe composite at time delay of 40 ns. The dotted red circle marks shock origin. There are several interesting points in the image - a dark band behind the shock-front for glycerol-epoxy nanoframe, brighter rings following the dark band, which are symmetrically observed inside of the shock origin, and disappearance of the dark bands.
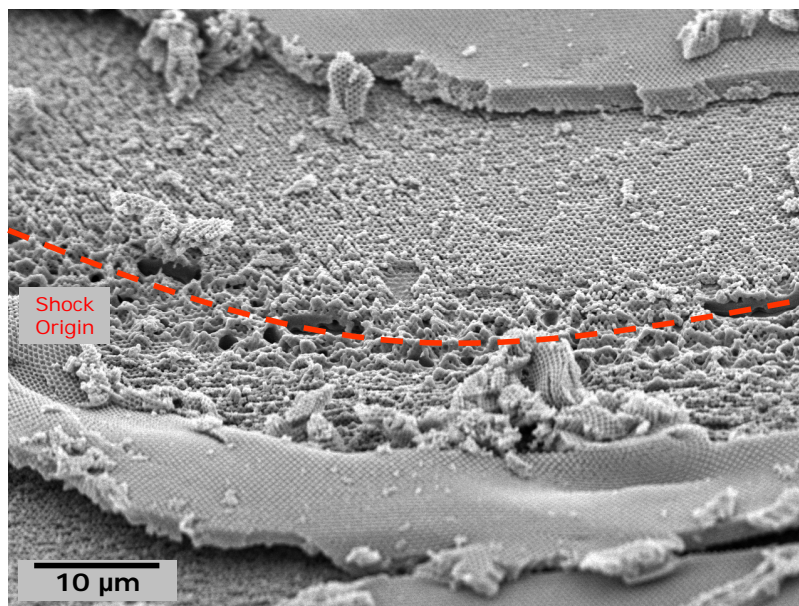
Figure 5-21: SEM image of the nanoframe structure destroyed by laser shock. The dotted red line marks initial excitation by the laser in the form of a ring using an experimental setup consisting of an axicon and a lens. The post-mortem analysis through SEM clearly depicts effects of the nanoframe structure in shock mitigation.

5.5.3.2 Shock Studies in Gold

Shock measurements were performed on a 25 nm thick gold layer sandwiched between two 100 μm thick glass substrates in the sample configuration similar to the one shown in Figure 5-6 with the current optical setup. The CCD images are shown in Figure 5-22 for different time delays varying from 2 ns up to 9 ns for an input laser pulse energy of 0.50 mJ. The average shock wave speed in gold extracted from these images is in the range 5.0 - 5.5 km/s (Note that longitudinal acoustic speed in gold is around 3.2 km/s).
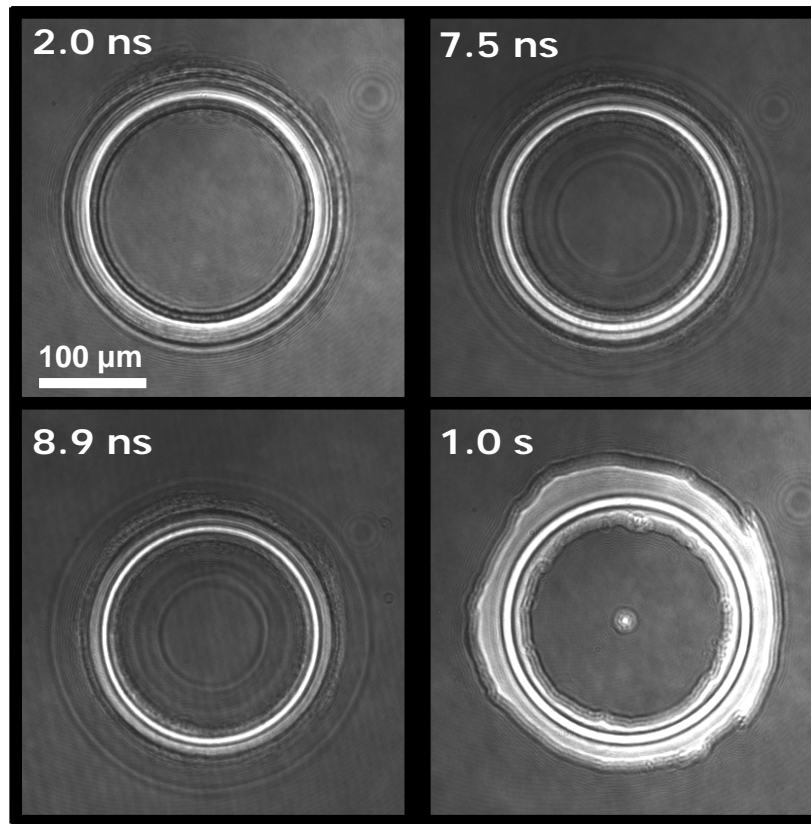
Figure 5-22: Time-resolved CCD images after target (25 nm thick gold layer sandwiched between two 100 μm thick glass substrates) was irradiated by an optical shock pulse. Raw images recorded on the CCD showing the time history at the indicated time delays - 2.0 ns, 7.5 ns, 8.9 ns during which shock wave propagation occurred in the gold layer, and 1.0 s. The images were recorded on a single-shot basis from different shocked regions of the sample since each sample region that was irradiated by the laser shock pulse was permanently damaged. The input optical shock pulse energy was 0.50 mJ.

5.6 Conclusion

A new method has been developed for direct observation of shock generation, propagation, and convergence in a sample. The method has been validated through measurements of shock propagation in liquid water. This unique technique enables rapid and direct measurement of the dynamic shock responses of advanced materials and structures. The CCD images recorded provide for the first time a direct dynamic picture of cylindrical shock convergence within the nanosecond time window. Since the shock is delivered to a submillimeter target spot by a high-power ultrafast laser pulse, novel sample designs can be quickly and effectively surveyed to diagnose and subsequently optimize their readiness in mitigating blast threats. This can be done with extremely small volumes ($<< 1$ mm^3) of material, long before high-volume processing is undertaken.

Our approach opens up new possibilities for controlling shock parameters and for a wide range of spectroscopic measurements of shock propagation and sample response. The optical configuration and sample geometry make shock wave formation and propagation directly accessible to optical imaging and spectroscopic probes with wavelengths ranging from UV to far-IR. For example, IR spectroscopy of sample vibrational modes can be conducted to determine both molecular and collective material responses to shock.

One of the main limitations of this technique is that it is not feasible to continue the study of the converging shock as it approached the center of the ring due to increased turbulence. This is unsatisfactory since the main nonlinear focusing effects become more pronounced as the strength of the shock increases in the vicinity of the center.

Chapter 6

Single-shot Streak Camera Measurements of Laser-Driven Lateral Shock Propagation

6.1   Introduction

Researchers have investigated many different optical methods for the characterization of shock waves [180]. These include, but are not limited to, methods based on the use of interferometers such as the Mach-Zehnder and the Michelson interferometers [181, 182, 183]; digital holographic methods based on capturing shock phenomena with a photoelectric camera (for example, a charge coupled device, CCD) and subsequent image processing [184]; speckle photography based on tracking the movement of speckle patterns, recorded on photographic plates [185] or a CCD [186]; shadowgraphy based on deflection of light due to gradients in the refractive index of a material, leading to pattern with characteristic bright and dark zones which can be recorded photographically [187]; and schlieren photography based on the use of an image forming system with a spatial filter at its Fourier plane to detect the change of direction of rays due to phase disturbances [188]. Some less common techniques include Talbot and Moiré methods [189], the probe beam deflection method [190], combined methods

[191] and optical sensors [192] employed to study shock wave dynamics.

Photography has been used widely for shock wave research [193, 194]. For recording fast phenomena, photographic plates combined with short pulse laser beams, streak cameras and fast CCD cameras have been used.

Pecha et al. used a streak camera with high spatial and temporal resolution for imaging the dynamics of the violent collapse in single-bubble sonoluminescence [195]. The signal-to-noise ratio was increased by integrating over about 10^5 streak images. The sonoluminescence pulse initially appears as a dark spot. Before the sonoluminescence pulse was emitted, the radius and thereby the scattered light from the collapsing bubble decrease rapidly, leading to a single line in the streak image with fast intensity decay. The two outer lines were caused by the outgoing shock wave which is emitted simultaneously with the sonoluminescence pulse from the bubble. Most of the light seen in top image of Figure 6-1 was scattered at the strong gradient of the refractive index at the shock front. The curvature of the outer lines clearly demonstrated the strongly nonlinear propagation at the beginning of the emission.

The distance of the shock front from the collapse center was determined from the streak image at different times, forming the complete trajectory of shock propagation. The shock velocity was determined from the derivative of the fitted curve. The bottom image of Figure 6-1 depicts the trajectory and the velocity in the full time frame. At the beginning, the shock wave propagated with a velocity of almost 1.43 km/s and ended up with a velocity of 6.0 km/s. The increased shock front velocity was modeled by the non-linear equation of state of water which was used to estimate the shock wave amplitude or pressure.

In the previous chapter I demonstrated an optical method for spatially and temporally resolved shock-wave velocity and pressure measurements. Cylindrically converging shock waves are produced by laser-induced irradiation in a sandwich sample configuration using an axicon-lens combination. While interferometric imaging using a CCD provides comprehensive information at selected time instants. The time period of many nanoseconds makes it impractical to record 2D CCD images on a near-continuous basis. However, once it is established that the response is cylindri-
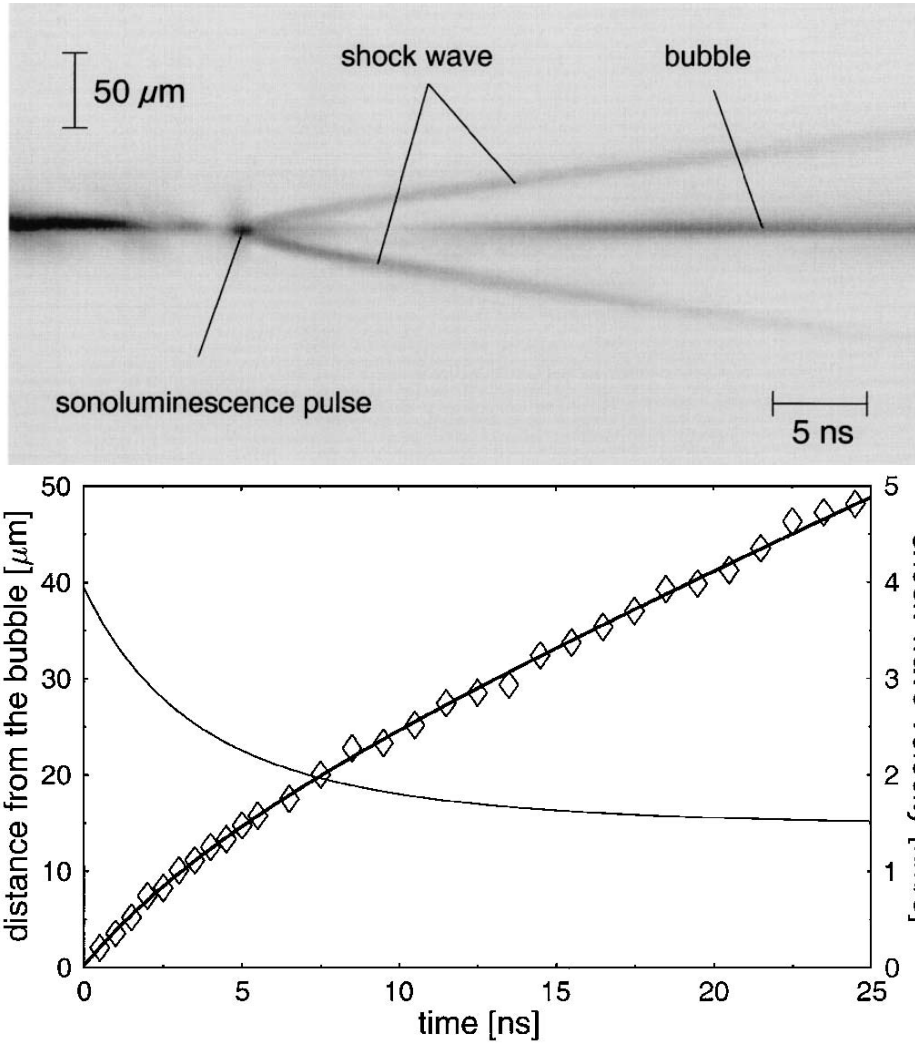
Figure 6-1: (Top) Streak image of an outgoing spherical shock wave emitted by a sonoluminescence bubble into water. Laser light is scattered at the bubble as well as at the emitted shock wave. The spatial and temporal resolution are 2 μm and 500 ps respectively. The dark parts of the image correspond to high light intensity. (Bottom) Distance of the shock wave from the bubble is determined from the streak image (open symbols) and corresponding fit (solid line). The shock wave velocity shown with smooth curve, is the derivative of the fit.

cally symmetric, a single spatial dimension is sufficient and the second dimension can be used for time in a streak camera recording, as in the example presented above from a three-dimensional rather than planar propagating disturbance. The streak camera recording provides a continuous time-resolved picture of the entire shock event.

This chapter will present single-shot time-resolved characterization of laser-induced shock waves in water using streak camera imaging, as well as numerical simulations to estimate the shock pressure.

6.2   Experimental Setup

The time-resolved responses were observed by a Hamamatsu C5680-21 streak camera with a N5716 (S-20) streak tube, M5677 slow sweep unit, A1976-01 input optics, A2886-06 output lens assembly, A1471-14 CCD mount adapter and C4742-95-12NR digital CCD camera (Orca 100). The typical time resolution of a streak camera is better than 150 ps in the 50 ns time window, limited mainly by the slit width of the streak camera and the camera pixel size. The streak camera was triggered by a pattern generator (Stanford DG535) and all electronics were controlled by a computer via GPIB (IEEE-488).

Figure 6-2 shows a schematic illustration of the target assembly for the shock parameter measurement in water together with the focusing shock generation and the streak camera recording system. The experimental setup consists of two parts: the first part is used to generate the shock, whereas the second part is used to measure the speed of the shock waves emitted by streak camera. For shock generation, laser pulses with 300 ps duration emitted from a Ti:sapphire laser and amplifier (Quantronix Titan, $\lambda = 800$ nm, emitting pulse duration of 300 ps) are focused through an axicon and a lens to form a ring pattern inside the liquid layer sandwiched between two $100\ \mu$m thick optical glass windows. The liquid layer has two flat windows of high optical quality on opposite sides to enable undisturbed imaging of the ring. The setup is identical to the one used previously to investigate shock-wave phenomena by CCD imaging. The pulse energies delivered into the sample can be varied up to 4.0 mJ.
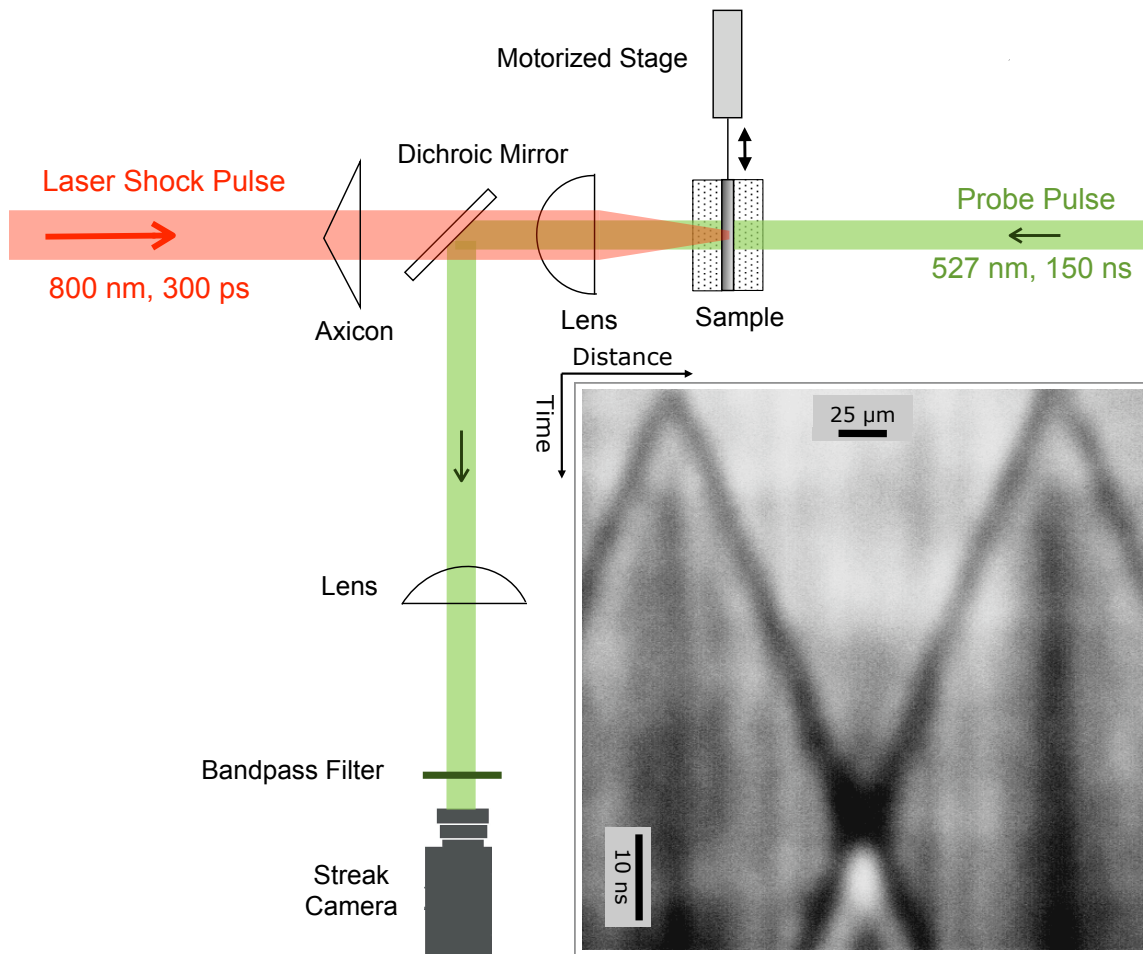
Figure 6-2: Schematic illustration of the experimental set-up showing focusing shock generation and streak camera imaging. The shock wave generated directly in the sample propagates laterally within the sample layer and the streak camera is used as a probing tool to record images. The complete time history of the shock propagation is observed by the high-speed streak camera in a single shot. The use of a Q-switched second harmonic Nd:YLF green laser provides bright homogeneous illumination over the entire streak window. The optical shock pulse (wavelength 800 nm) is shown in red and the imaging pulse (wavelength 527 nm) is shown in green color. The inset shows a single shot streak image of a converging shock wave generated within a 5 μm water layer (with carbon nanoparticles) sandwiched between two 100 μm thick glass substrates for input pulse energy of 0.15 mJ, where the horizonal axis is distance (μm) and the vertical axis is time (ns). The shock wave appears as a dark line in the streak images, illustrated further in the top image of Figure 6-3. The incident energy of the optical laser shock pulse can be tuned from 0 to 4 mJ.

Earlier investigations found significant deviations of the shock-wave velocity from the acoustic velocity during the last few tens of microns close to center of convergence of the shock wave [195]. The time window of the streak camera must therefore cover this time regime, requiring very intense illumination with nearly constant brightness for the entire period of time. This is achieved by the use of a Falcon 527 Series Q-switched green laser (Quantronix Falcon-527 series, high-power second harmonic Nd:YLF laser, $\lambda = 527$ nm) emitting pulses with a duration of 150 ns. Light from the Q-switched green laser is scattered by the propagating shock wave and is then focused onto the entrance slit of the streak camera with a two-lens imaging system. A bandpass filter (centered at 527 nm, $\Delta\lambda = 10$ nm) is placed before the slit of the streak camera to eliminate any stray light. The spatial resolution is 1 μm, limited mainly by the aberrations of the optical system and by instabilities of the propagating shock itself.

6.3   Image Analysis

In all the streak images, two distinct dark crossing lines with gradually increasing slopes can be observed. These lines correspond to the shock wave. At the shock front the refractive-index gradient is large and this leads to a deflection of the illuminating light from the imaging aperture, resulting in the dark appearance of the shock waves. The straight lines at the edges appear dark due to the sample response to initial excitation rather than wave propagation. The exploded nanoparticles might result in changed optical absorption at the probe wavelength. Basically the probe light is either absorbed or refracted differently (there is a change in the imaginary or real part of the refractive index). For the shock wave, it's a change in refraction.

The streak images are processed using ImageJ and the image processing toolbox in MATLAB to extract the shock-wave trajectories. On the streak images, the shock wave appears as a dark shadow on a bright background with an abrupt transition between bright and dark. Detecting the shock front is thus equivalent to finding the location of the sharp initial intensity transition between the bright background and

the dark shock-wave image. The shock position $r(t)$ as a function of time t is extracted from the streak images. The resulting $r(t)$ curves are differentiated with respect to time to yield shock-wave velocities that are then converted to shock pressures with the aid of the equation of state of water.

The exact functional relationship of the increase in velocity (or pressure) with respect to time or radial distance is not known. For any sample, it will be influenced by the dependence of both attenuation and velocity on shock pressure, which changes as the shock wave converges. Attempts were made to fit the experimental data for the converging cylindrical shock wave radius (i.e., shock-wave position $r(t)$ as a function of time t) obtained from the streak camera recording to a power and a nonlinear polynomial trajectory through the least square fit method. Figures 6-3, 6-4, 6-5, and 6-6 show streak images at 0.15, 0.65, 1.25, and 2.50 mJ input excitation energies respectively as well as the corresponding trajectories extracted through image analysis.

6.4   Results & Discussion

6.4.1   Accuracy and Reproducibility

The shock wave peak pressure is determined from the shock-wave speed, which is obtained as the temporal derivative of the shock-wave position. Therefore high accuracy in shock position detection is essential for accurate measurements of shock peak pressure. The measurement accuracy of the method presented depends on the spatial and the temporal resolution obtained in the images, the accuracy of the shock-wave extraction during image analysis, and the accuracy of the analytic fit through the extracted data.

The uncertainty in determination of the shock front position was estimated to be around 1 μm and was limited primarily by the spatial resolution of the streak camera and the width of the propagating shock wave front. The temporal resolution was determined by the streak rate (or time window) and the width of the slit image on

Figure 6-3: (Top) Single-shot streak image of a cylindrically focusing shock wave propagating in water at an input laser energy of 0.15 mJ. (Bottom) Shock wave trajectory of the converging waves extracted from the streak image by a best fit polynomial equation showing nearly a linear speed of 1.8 km/s (blue dotted line) until the center of convergence and a speed of 1.4 km/s (red dotted line) after passing through the center of convergence, which is equal to the acoustic speed in water. The radial distance on the vertical axis is measured from the center of convergence and extends on both sides for the two propagating right and left lobes at any given instant of time. Both right and left lobes have similar trajectories showing symmetry and identical shock propagation speed.
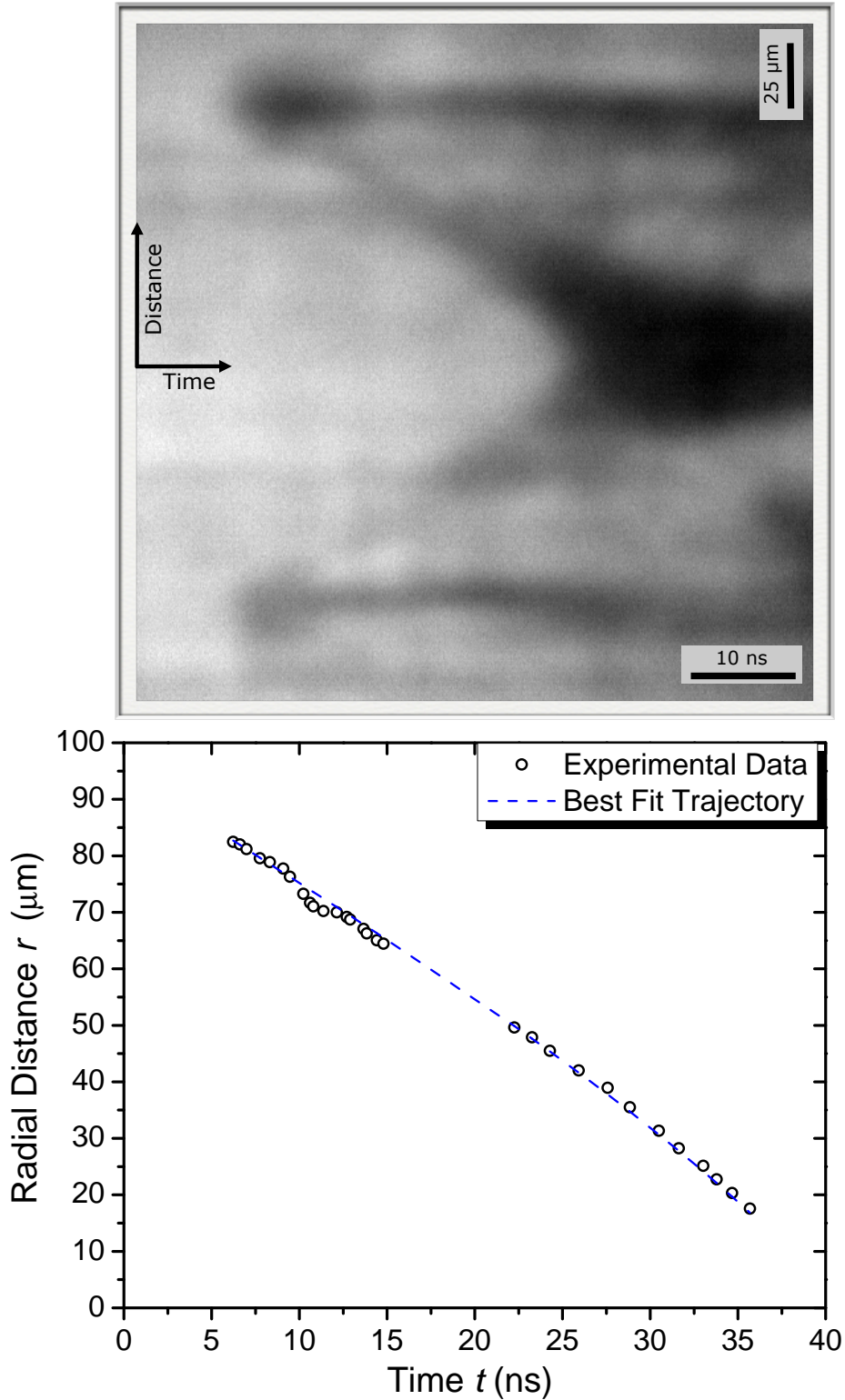
Figure 6-4: (Top) Single-shot streak image of a cylindrically focusing shock wave propagating in water at an input laser energy of 0.65 mJ. (Bottom) Shock wave trajectory (shown in the blue dotted line) extracted from the streak image by nonlinear polynomial least squares fit to the experimental data.
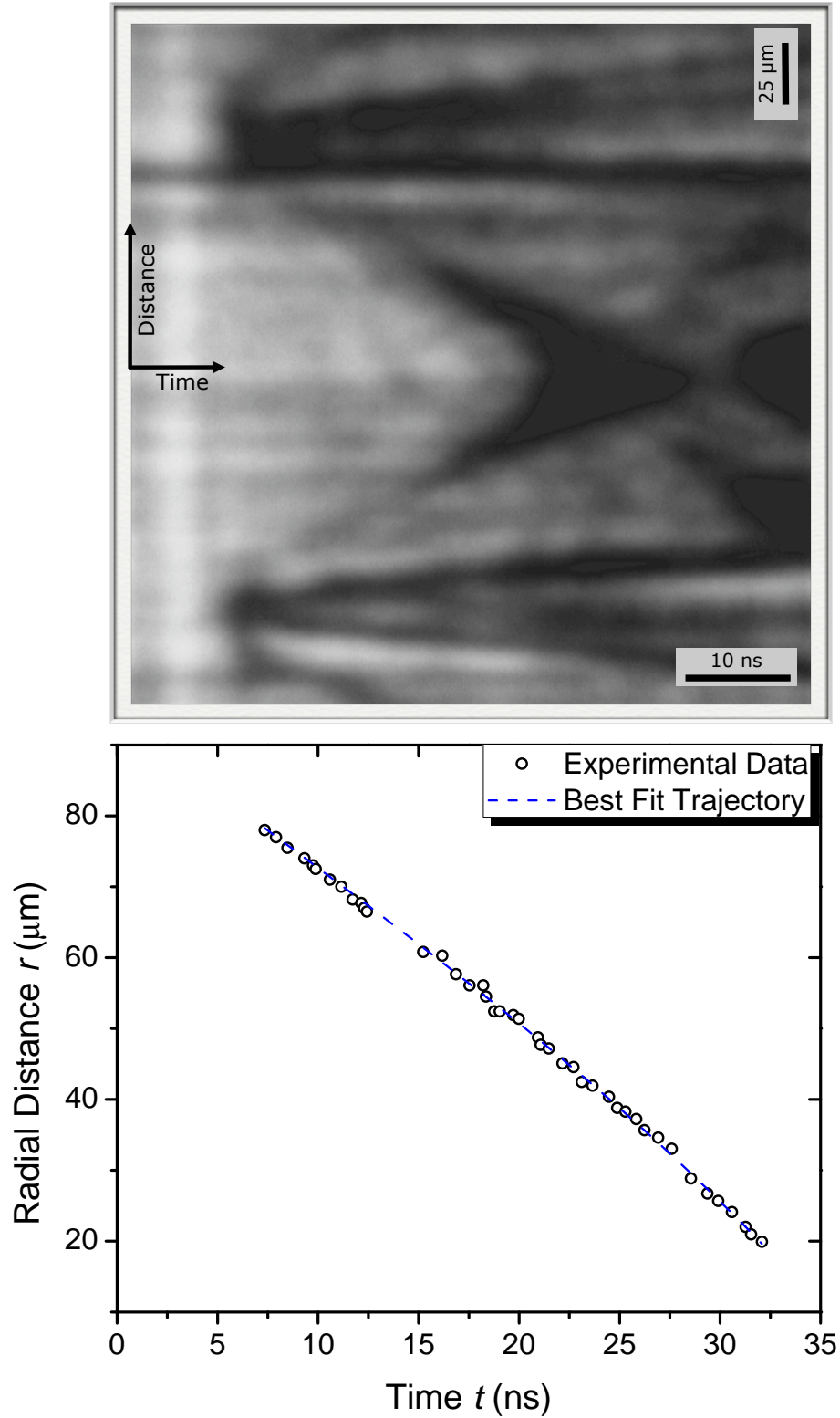
Figure 6-5: (Top) Single-shot streak image of a cylindrically focusing shock wave propagating in water at an input laser energy of 1.25 mJ. (Bottom) Shock wave trajectory (shown in the blue dotted line) extracted from the streak image by nonlinear polynomial least squares fit to the experimental data.
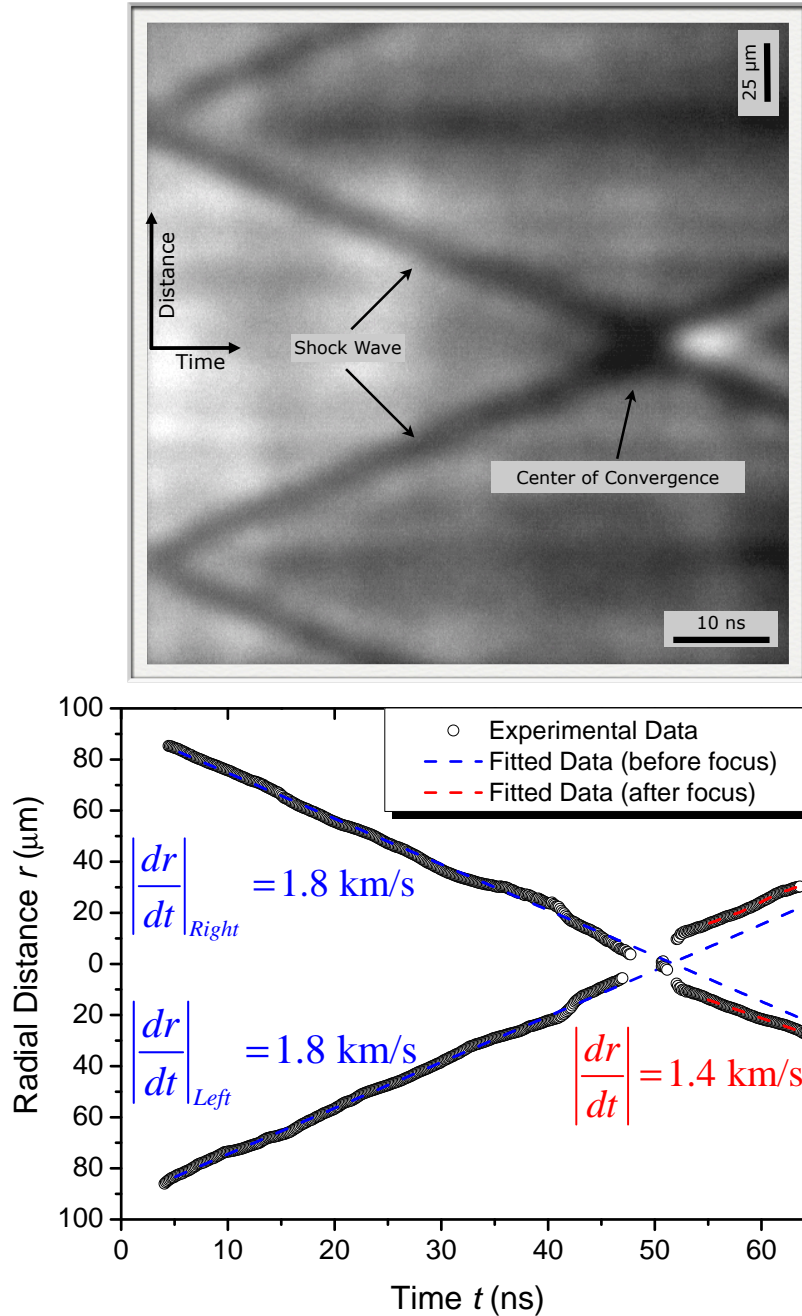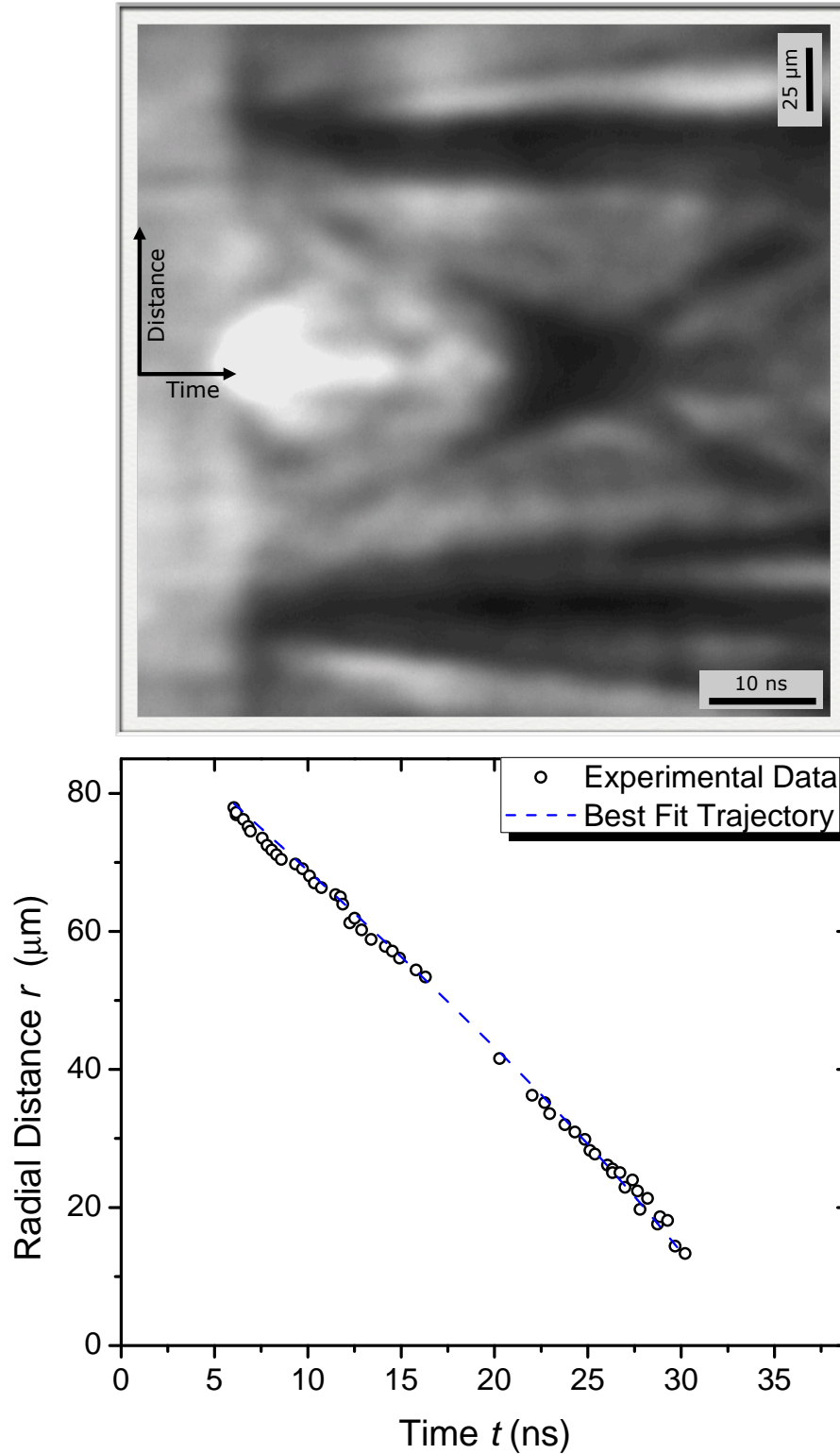
Figure 6-6: (Top) Single-shot streak image of a cylindrically focusing shock wave propagating in water at an input laser energy of 2.50 mJ. (Bottom) Shock wave trajectory (shown in the blue dotted line) extracted from the streak image by nonlinear polynomial least squares fit to the experimental data.

the photocathode and was better than 150 ps. To check the reproducibility of the method, shock waves from several laser shots at equal excitation pulse energies were investigated. The uncertainty in shock front position was around 5 μm close to center of convergence since the shock front was very broad, and it was not possible to decide on its position with precision better than 5 μm. Hence, the uncertainty in shock front position really start out around 1 μm and got bigger, reached 5 μm, as the shock got close to the center.

6.4.2   Determination of Shock Speed

The shock wave is visualized by the refractive-index change arising from the shock-wave-induced compression of water by means of a streak photography, which then allows the position of the shock to be followed through time, and the speed of the shock to be determined directly by differentiation of the trajectory of the shock wave.

There is the appearance of a discontinuity in the propagation distance as the shock waves moves through the focus. This phenomenon is clearly observed in Figure 6-3. The slope of the trajectory (or shock velocity) before the focus is 1.8 km/s and then it becomes 1.4 km/s after the waves diverges away from the focus. However, the propagation distance is greater for diverging waves at any time instant (as shown in red dotted lines) than what would have been predicted using extrapolated values for the waves converging towards the focus (as shown by blue dotted lines after 50 ns time delay). This is likely due to the Gouy phase shift, a well known occurrence for converging waves that has been observed through imaging of both terahertz waves and acoustic waves [196, 197]. Note that this is distinct from the appearance of a sudden jump of the transition from light to dark at each shock front as the waves from opposite sides meet at the center, due to the finite width of the shock waves.

The derivative of the best fit function provides shock velocity U_s which rapidly increases and approaches super-sonic velocity close to the center of convergence, suggesting strongly nonlinear propagation. A master curve depicting dependence of shock wave velocity on the radial distance for different input excitation energies is shown in Figure 6-7. A speed of about 3.4 km/s, more than twice the sound speed, is reached
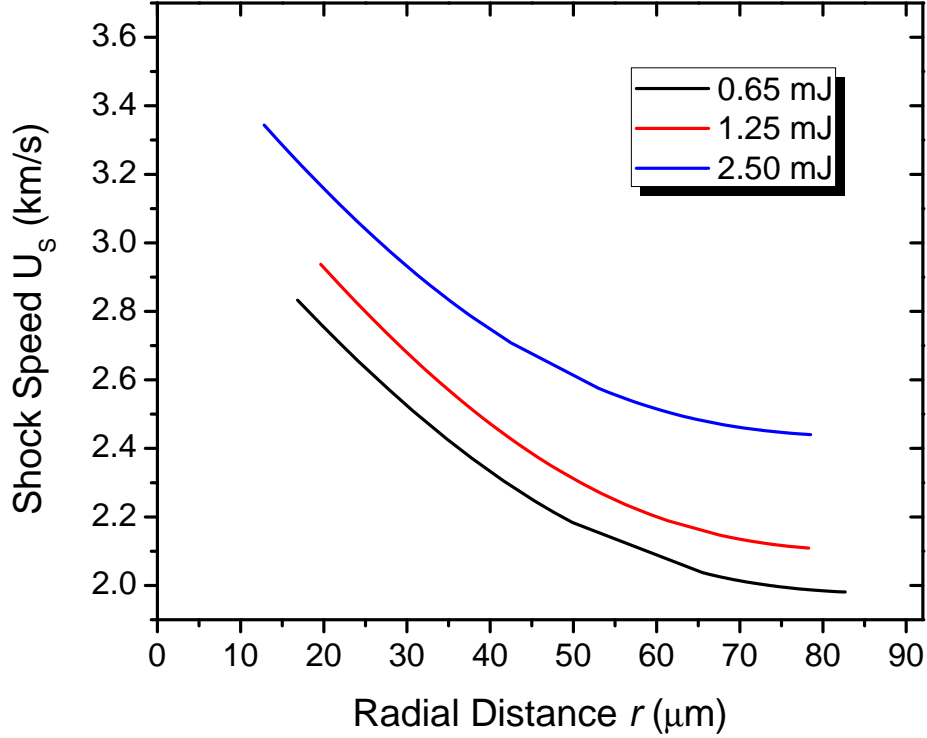
Figure 6-7: Master curve depicting dependence of shock wave velocity on the radial distance for different input excitation energies.

at a point 12 μm away from the focus for an input energy of 2.50 mJ.

6.4.3 Determination of Shock Pressure

The shock-wave peak pressure P (in GPa) in water is related to the propagation speed U_s (in km/s) of the shock through the equation of state and the jump conditions [162] at the shock front by

$$P = \rho_0 \ U_s \ \frac{U_s - c_0}{1.99} \qquad (6.1)$$

where $c_0 = 1.43$ km/s and $\rho_0 = 0.998$ g/cm^3 denote the acoustic velocity and the density of the undisturbed water, respectively. This is the same relationship used in the previous chapter (see Figure 5-15) for estimating shock pressure for data generated using CCD imaging.

Other relationships between the shock pressure P and the shock velocity U_s are

given by Cole [198] in equations 6.2 and 6.3

$$P = A \ \rho_0 \ U_s \left[10^{(U_s - c_0)/B} - 1 \right] \tag{6.2}$$

where $A = 5.190$ km/s and $B = 25.306$ km/s are empirical constants determined from Rankine-Hugoniot data.

$$P = C \left[2 \left(\frac{n-1}{n+1} \right) \left(\frac{U_s}{c_0} - 1 \right) + 1 \right]^{\frac{2n}{n-1}} - C \tag{6.3}$$

where n and C are parameters of the Tait equation of state. For water, $C = 0.275$ GPa, and $n = 7.44$.

The estimated shock pressure P determined from equations 6.1 - 6.3 are in good agreement with each other. Equation 6.3 is preferred for its versatility in the present work so as to compare the shock pressure values with those obtained through numerical modeling. Figure 6-8 shows the shock wave pressure P in water as a function of radial distance for different input excitation energies using the empirical relationship given in equation 6.3. An excitation input energy of 2.50 mJ is able to reach a substantial pressure of 3.5 GPa at a radial distance of 12 μm from the focus. The pressure is expected to be even higher as the shock fronts converge and focus at the center.

6.5 Numerical Modeling[*]

6.5.1 Methodology & Formulation

A numerical simulation of the laser shock experiment was performed using a finite element code developed and used by "Radovitzky Group"at MIT [199]. This code uses an explicit integration, Lagrangian finite element formulation to solve the finite elastodynamics problem, with the unknown variable being the displacement of the

[*]Done collaboratively with Piotr Fidkowski in the group of Prof. R. Radovitzky
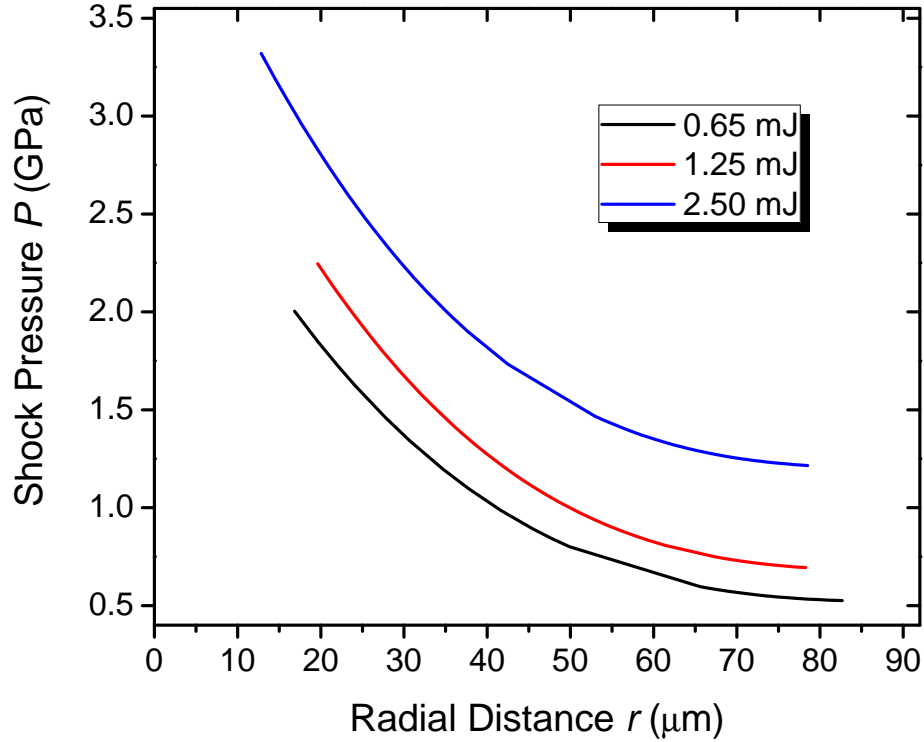
Figure 6-8: Estimation of shock wave pressure in water as a function of radial distance for different input excitation energies using the empirical Hugoniot relationship given in equation 6.3.

mesh. Using a Lagrangian formulation for modeling a fluid is slightly unusual, but will allow us to use the same framework for shocks in solids.

To model the constitutive response of the water, we use a Newtonian fluid with an equation of state. Given a deformation field

$$x = \phi(X) \tag{6.4}$$

where x are the spatial coordinates and X are the material coordinates, we can calculate the stress tensor in the water via

$$\sigma_{ij} = 2\,\mu\,d_{ij}^{\mathrm{dev}} + p\delta_{ij} \tag{6.5}$$

where μ is the usual fluid viscosity and d_{ij}^{dev} is the deviatoric part of the rate of

deformation tensor

$$d_{ij} = \frac{1}{2}(v_{i,j} + v_{j,i}) \tag{6.6}$$

with

$$v_i = \dot{\phi}_i \phi^{-1} \tag{6.7}$$

representing the components of the velocity vector. The pressure p derives from an equation of state for the material, and is assumed to depend only on the volumetric part of the deformation. For water, a particularly stable equation of state for shock problems is the Tait equation of state [199], which derives from an energy of the form

$$e = e_0 - \frac{p_0 + p_c}{\Gamma_0 \, \rho_0} + \frac{p + p_c}{\Gamma_0 \, \rho} \tag{6.8}$$

where e is the internal energy, p the pressure and ρ the density and e_0, p_0, ρ_0 the same quantities at their reference or initial state. The Tait parameter Γ_0 is a constant and the computed pressure p_c (which is purely a material property) is given by

$$p_c = \rho_0 \, a_0^2 - (\Gamma_0 + 1) \, p_0 \tag{6.9}$$

where a_0 is the speed of sound in the reference state.

If we assume an isentropic process, then the partial derivative of internal energy with respect to the specific volume $v = 1/\rho$ gives

$$\left.\frac{\partial e}{\partial v}\right|_s = -p \tag{6.10}$$

After some substitution and integration we derive the dependence of pressure on density

$$p = \frac{p_c}{\Gamma_0 + 1}\left[\left(\frac{\rho}{\rho_0}\right)^{\Gamma_0+1} - 1\right] + p_0\left(\frac{\rho}{\rho_0}\right)^{\Gamma_0+1} \tag{6.11}$$

We can assume that the change in the second term in the above equation is small and reform the equation as

$$p = B\left[\left(\frac{\rho}{\rho_0}\right)^{\Gamma_0+1} - 1\right] + p_0 \tag{6.12}$$

154

where B is a constant, known as second Tait parameter, and p_0 is the reference pressure of the water.

For water, we use the parameters $\rho_0 = 998$ kg/m^3, $\Gamma_0 = 6.15$, $B = 3.042 \times 10^8$, and $\mu = 1.002 \times 10^{-3}$ Pa-s. This yields a theoretical acoustic wave speed of 1476 m/s and reference pressure p_0 of 1.014×10^5 Pa. The above equation also indicates how we can apply our initial conditions. The energy from the laser impulse goes into heating of the water. Given the very short time scale of the laser impulse, this heating causes an increase in pressure, which we apply via the reference or initial pressure p_0. Currently, this pressure increase is applied as a step increase in the concentric ring of the laser pulse.

The numerical formulation as it is will not be very good at handling shock conditions since the very thin shock cannot be resolved by a finite discretization. "*Shock Capturing*" refers to additional techniques used to allow the numerical code to handle a discontinuous shock. Artificial viscosity is one such technique, that essentially smears the shock across several elements while trying to maintain the proper relationships across the shock. We use the formulation of artificial viscosity employed by Lew et al. [200]. In this formulation, we define a modification of our fluid viscosity,

$$\mu_h = \mu + \Delta\mu \tag{6.13}$$

where μ is the physical viscosity coefficient and $\Delta\mu$ is the added artificial viscosity. At any integration point within the element, the artificial viscosity can be calculated by

$$\Delta\mu = \begin{cases} \max(0, -\frac{3}{4}h\rho(c_1\Delta u - c_L a) - \mu) & \Delta u < 0 \\ 0 & \Delta u \geq 0 \end{cases} \tag{6.14}$$

where h is the element size, c_1 and c_L are parameters, a is the acoustic wave speed and Δu is a measure of the velocity jump across the element. This artificial viscosity will smear the shock out over several elements, which allows our discretization to capture the essentially discontinuous shock.

The simulation was run over a variety of initial reference pressures using a 3-D

mesh with 214684 2nd order tetrahedral elements. This explicit simulation is parallelized, and simulations are generally done on 64 processors available in the group cluster. Pressure data was averaged around the ring and then post-processed to extract the peak location, which was defined as the average of the 95% crossover locations.

6.5.2   Simulations

The numerical simulations for input energies of 0.15 mJ and 0.65 mJ are shown in Figure 6-9. The experimental data and the simulations are in good agreement for the shock wave trajectories and thus, the model can be used to estimate shock pressure close to the focus.

The numerical simulations are helpful to determine shock pressure close to the focus where resolution becomes poor in streak camera images. Figure 6-10 shows a plot of radial pressure values derived through numerical simulation for different input energies. The pressures were around 1.25 GPa and 6.5 GPa close to the focus for input energies of 0.15 mJ and 0.65 mJ respectively. In contrast, estimation of shock pressures from streak camera images using the empirical Hugoniot relationship on the extracted trajectories (as shown in Figure 6-8) is a big challenge and there are inherent problems associated with spatial resolution of the streak images, especially close to the focus where interesting shock dynamics come into play.
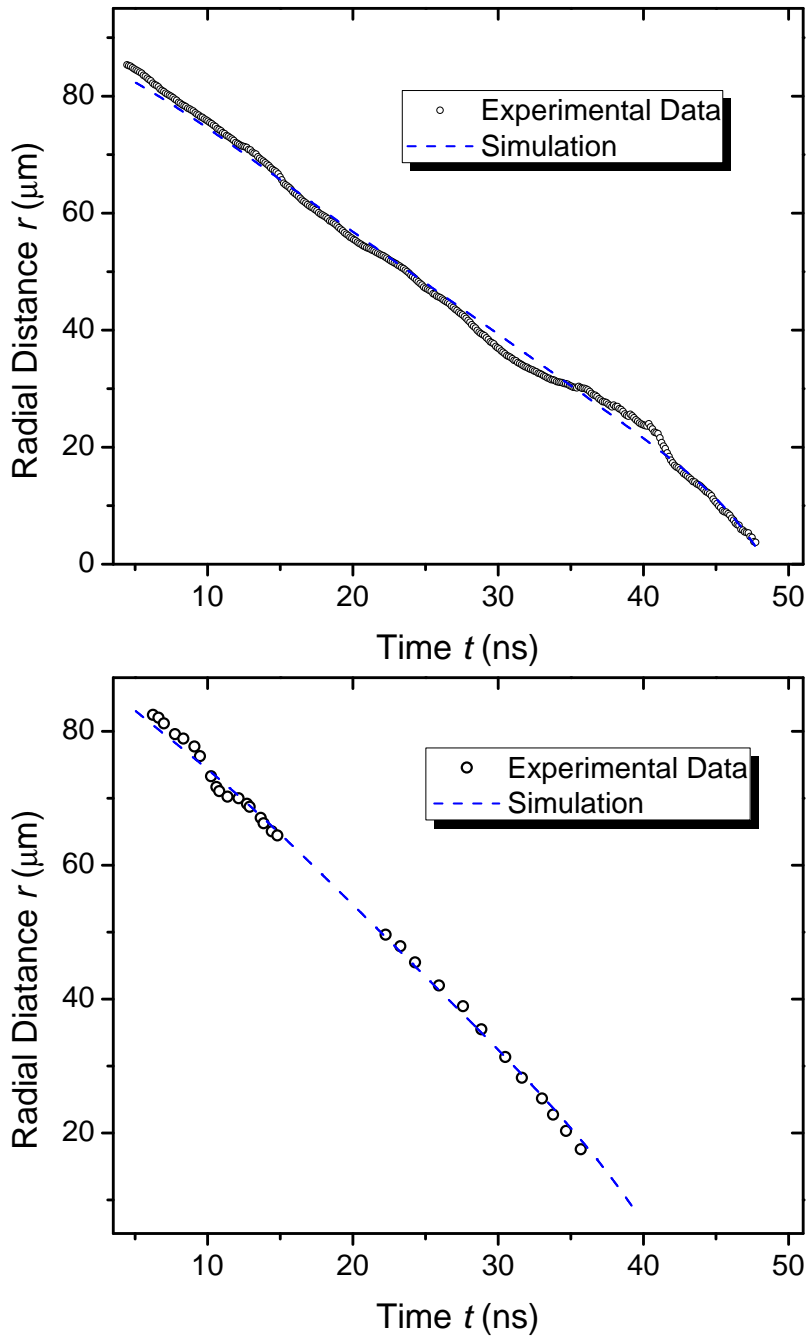
Figure 6-9: Simulated trajectory (represented by blue dotted line) for a cylindrical focused shock wave propagating in water at an input laser energy of 0.15 mJ (Top) and 0.65 mJ (Bottom). The open circles represent the experimental data extracted through streak camera imaging.
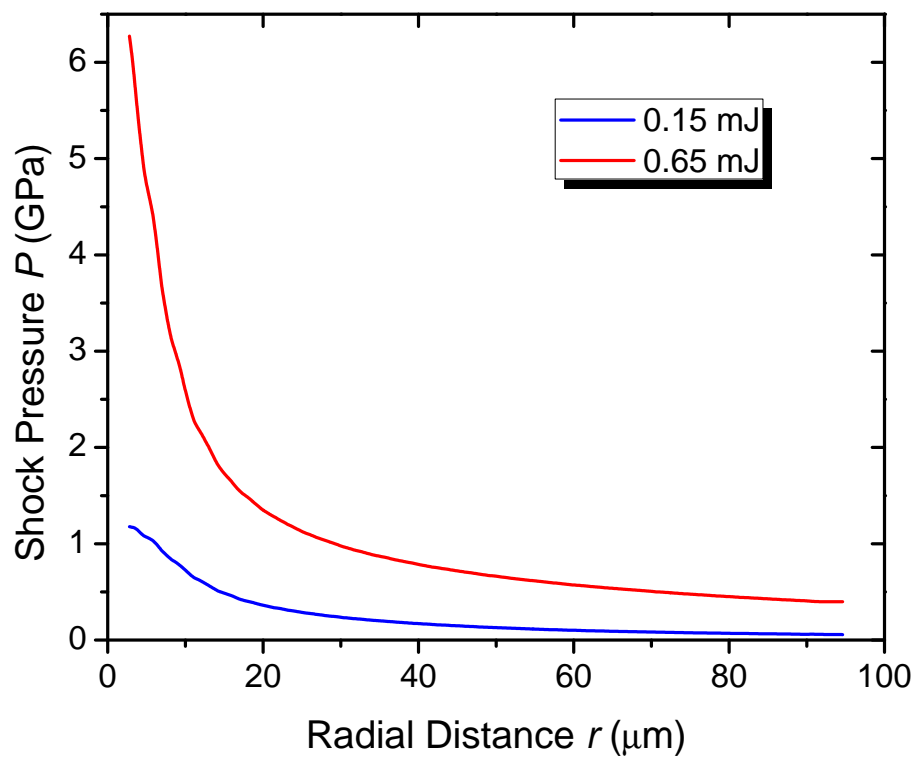
Figure 6-10: Plot of radial pressure values derived through numerical simulation for input energies of 0.15 mJ and 0.65 mJ, indicating the higher pressure of the shock close to the focus.

6.6   Conclusion

The feasibility of single-shot spatially and temporally resolved streak camera pressure measurements of shock waves in water has been demonstrated. The CCD images shown in the previous chapter were recorded during separate events, with an increasing time delay between the shock generation and the photograph of the shock wave, and the shock trajectory was then reconstructed from collected CCD images at different time delays. The complete shock wave trajectory is obtained from the streak image in a single shot, and the shock position is also determined much more accurately which is of particular importance close to the focus where the propagation and the intensification of the shock wave is very rapid.

In conclusion, the results show that the dynamics of the shock phenomena can be studied with high spatial and temporal resolution by direct imaging using a streak camera as a detector. Furthermore the relative ease and the speed of obtaining spatially resolved pressure amplitudes allows parametric studies such as investigations of the pulse energy and pulse duration dependence of shock-wave emission during laser-induced breakdown. Numerical simulations have been performed to estimate shock pressure, and a considerably high pressure is reached close to the focus.

Chapter 7

Conclusions and Future Directions

7.1 Summary and Conclusions

Firstly, impulsive stimulated thermal scattering (ISTS) photoacoustic measurements were conducted with a range of acoustic wavelengths and corresponding frequencies in order to extract the full set of acoustic and modulus parameters for novel structures. These measurements were performed on complex materials including block copolymers, multilayer polymeric films, nanocrystalline and metallic materials, and ceramic structures. The results illustrate the general value of ISTS measurements in revealing the mechanical behavior of nanostructured polymeric materials. The acoustic properties of a multilayer structure produced by sequential spin coating of PMMA and nano-TiO_2 showed a very low group velocity in the high-wavevector range and a strong dispersion in the group velocity at higher frequencies. These results suggest that this type of material could be used in the future for shock mitigation applications.

Subsequently, a novel method for optical cylindrical shock focusing was developed in a manner that permits direct real-time visualization of the shock front and the shocked material using either a charge-coupled device (CCD) camera or a streak camera. This approach opens up new possibilities for controlling the shock parameters and allows access to pressures in the multiple gigapascal range. The optical generation of a shock wave is followed by time-resolved optical measurements of sample properties both during and after shock propagation. Furthermore, the optical configuration and

sample geometry make shock wave formation and propagation directly accessible to a wide variety of real-time spectroscopic probes of molecular and collective responses. The characterization of an illustrative test sample composed of a thin confined layer of water loaded with carbon nanoparticles was described to demonstrate the utility and potential of this new technique.

Single-shot streak camera measurements were conducted to investigate the dynamic properties of water under shock loading. Combined with numerical simulations, it was demonstrated that there was considerable amplification in shock pressure close to the focus and shock pressures close to 10 GPa were reached in and around the focus.

The parameters of the laser pulse used to launch the shock wave, including beam size and shape, pulse duration, and intensity, are fully controllable, yielding considerable control over the shock wave that is generated. The mechanical response of newly fabricated advanced materials and structures to ballistic shock loading can now be measured directly and rapidly even with an extremely small sample volume ($<< 1$ mm^3).

7.2   Future Directions

The power spectrum of a typical blast is broad, with spectral components (with most destructive energy) present between 1 and 20 kHz [201]. Efforts to mitigate the harmful effects of blast waves could involve attempts to attenuate, reflect, or generally control the most damaging parts of the power spectrum. In an attempt to address this problem, methods of fabricating two-dimensionally periodic *phononic crystals* – band gap structures designed to forbid the propagation of specific acoustic modes, are being developed [202, 203]. Examining the response of such structures with band gaps in the spectrum of shock frequencies will provide important information toward developing materials for blast mitigation. In laser shock measurements described in this thesis, the power spectrum of the induced shock lies at far higher frequencies and correspondingly shorter wavelength ranges than mechanically generated shocks.

162

However, the mitigation principles learned from laser shock measurements are scalable to the ranges appropriate for blast mitigation.

The method of optical shock generation may be applied to individual material components of complex assemblies to assess their intrinsic behavior under extreme conditions and to assemblies themselves to assess their collective performance. Tracing the changes in the values of the mechanical properties of the components details the energy propagation and dissipation modes following nonlinear viscoelastic compression. The generated data can be correlated with important physical processes including viscous flow, thermal diffusion, phase transitions, phase separation, chemical reactions, and plastic changes in microstructural morphology induced by the propagation of shock waves through the material. Direct observation of shock propagation through periodic and other heterogeneous structures will help to guide optimization of such structures for shock mitigation. Since the shock is delivered to a submillimeter target spot by a high-power, ultrafast laser pulse, novel samples designs can be quickly and effectively surveyed to diagnose and subsequently optimize their readiness in mitigating blast threats.

The developed method is also useful for the characterization of phononic bandgap materials and other structures with tailored acoustic properties, and for the assessment of the mechanical properties of multicomponent polymer systems and the dependences of their properties on composition and processing variables. The developed technique can be applied to the characterization of dynamic mechanical properties and shock response of complex materials and nanostructures, human tissue models, and specially fabricated periodic structures that may show exceptional shock mitigation properties. The shock responses that will be determined for various materials and structures include changes in viscomechanical properties, phase transitions or vitrification, and potential loss of mechanical integrity (in particular delamination) for multilayer structures. Shock propagation through the materials, and in particular through tailored nanostructures, will be measured and assessed. This characterization is essential for the optimization of new materials and structures for high performance shock mitigation.

Most of the performance parameters of materials and assemblies under ballistic or blast impact can be measured using the current technique with some modifications which support the multi-dimensional utility of the developed laser shock spectroscopy technique.

7.2.1   Shock Measurements in Polymeric Systems

The extension of the developed technique to polymeric systems will further the understanding of the shock responses of these materials to dynamic conditions. Specifically, it will enable the quantitative evaluation of the temporal evolution of mechanical properties in the nanoseconds to milliseconds ranges following shock loading. The ability to measure these changes as a function of shock parameters will produce important information regarding the interaction of ultrafast mechanical impact and material behavior. This will require understanding and analysis of non-linear viscoelastic and non-linear acoustic responses [204].

The rate-dependence of the elastic, plastic and failure behavior of polymers is well known under quasi-static and low rate deformation; however, the behavior under very high rates of deformation is still not well understood. The present spectroscopic technique can help to provide such an understanding for polymers, from molecular mechanisms of deformation resistance up to the elastic-viscoplastic stress strain response. This understanding can then be used in the development of a constitutive model that is accurate at these deformation rates.

A wide variety of complex materials including energy-absorbing and heterogeneous polymeric nanocomposites can be characterized using this technique. Research has shown that the physical properties of a given polymer may be dramatically altered by the introduction of a secondary nanoscale particulate phase, even at very low weight percentage loading [205]. Typical materials for future investigations include systems that show promise of heightened energy absorption and acoustic wave deflection and reflection under shock-loading conditions. Systems will be selected to take advantage of mechanisms such as filler-toughening, amorphization, chain scission, activated flow, and pressure-induced melting. Being able to directly measure the temporal develop-

ment of the mechanical properties of a polymer will indicate transitions and dynamical behavior within the material. Depending on the characteristic material behavior, the moduli may increase or decrease. Some viscous materials jam under high strain rate, whereas others can exhibit flow.

7.2.2 Thermal Curing Effects of Shock Waves on Polymers[*]

Laser-induced shock loading creates a lot of heat, which then dissipates by diffusion. The moving shock wave carries substantial energy and can induce thermal curing in photoresist polymers (e.g. SU-8) on a faster time-scale than diffusion. This phenomenon has been observed and further investigated using laser-induced shock loading on SU-8 samples. The usual procedure for writing in SU-8 involves exposure to UV light to activate photoacids followed by baking at elevated temperature to accelerate crosslinking and then a development step through solvent immersion. The sample if exposed to UV light and immediately developed without baking will completely wash away.

A sample produced with a two-photon direct write system in 5 micron thick SU-8 was used for preliminary experimentation. The axial resolution of the voxel was commensurate with thickness, so exposure was uniform through the thickness of the film. Figure 7-1 shows a SEM image of a baked/cured SU-8 film after laser shock loading. A 200 micron square was drawn in a film by rastering the low energy two-photon laser horizontally with vertical steps of 1 micron with an intensity picked so as to not heat the sample to the point of cross-linking. After the square was drawn, the high energy laser spot was focused at the center of the patterned area creating a shock and the sample was developed immediately afterwards. The explosion exposed (or cross-linked) some area directly around it, but otherwise only appears to have developed the pattered region as can be seen by the horizontal lines. This is expected to be due to the heat wave that the shock wave creates. Further study of this phenomenon could elucidate the possibilities for 3D ultrafast curing of photoresists and could also provide information about the temperature of the heat wave generated by a shock.

---

[*]Done collaboratively with Jon Singer in the group of Prof. Edwin L. Thomas
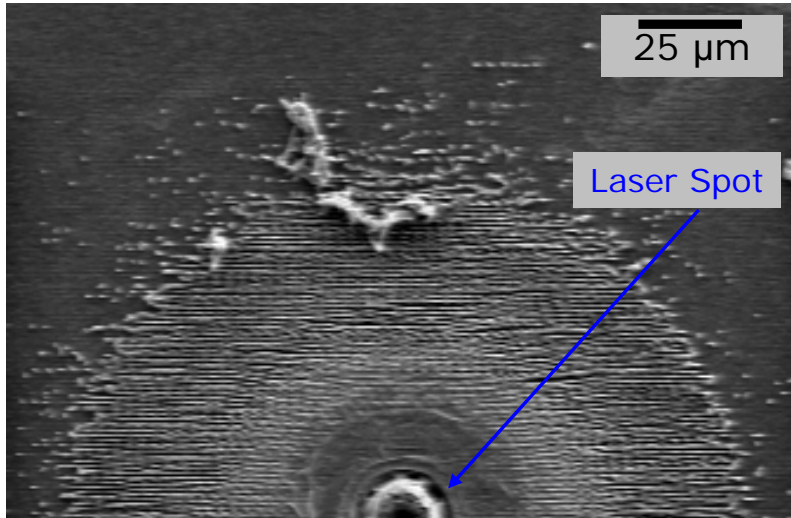
Figure 7-1: SEM image of a cured SU-8 film by laser shock that induces local heating. The high energy laser is focused to a 1 micron spot size at the center to create shock wave which potentially heats the surrounding SU-8 film at a rate faster than that predicted from thermal diffusion phenomena. Only the top half of the SEM image is shown here.

7.2.3 ISTS-Shock Measurements

Laser-induced shock loading can be synchronized with an additional laser pulse in order to generate and measure acoustic waves. ISTS measurements are therefore possible that track the dynamical evolution of mechanical properties in shocked materials. ISTS measurements of sample evolution will be conducted during the time period following the formation of the initial shock front. In this way the time-dependent evolution of the sample viscomechanical properties can be followed. This is of crucial importance in understanding the performance of protective materials under shock loading conditions, and is possible to carry out with small quantities of materials that are still under development in order to guide their optimization. These measurements will be of fundamental interest and will provide the static and dynamic material parameters for nanostructured polymeric systems.

Figure 7-2 shows a new experimental geometry that may permit shock pressure to be maintained for several nanoseconds. In this geometry, as described in Chapter 5, the sample is sandwiched between two sapphire or glass plates and the shock is excited directly within the sample. The shock wave propagates laterally in the plane of the
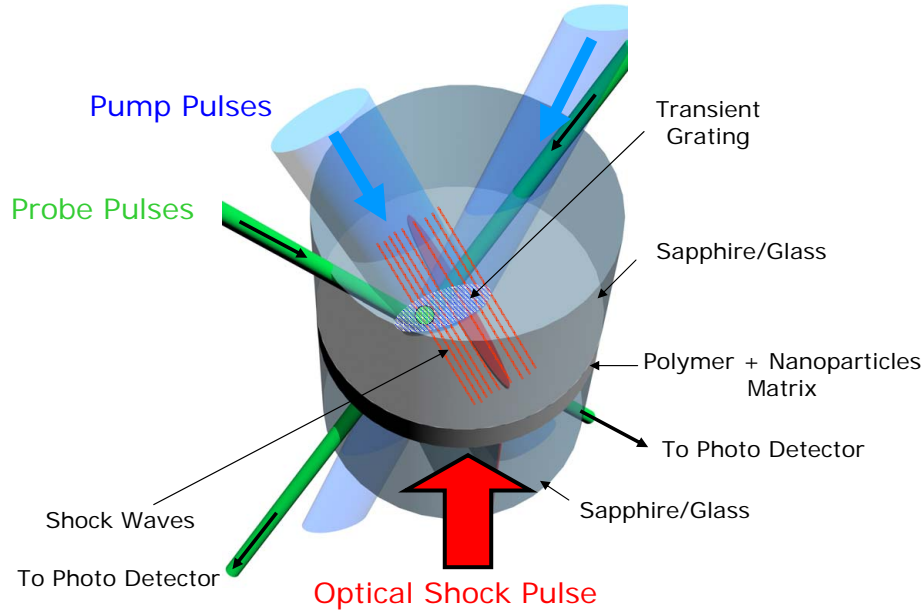
Figure 7-2: Proposed sample geometry for ISTS-Shock measurements. The sample (polymer with nanoparticles) is sandwiched between two sapphire or glass plates and the shock is excited directly within the sample using a cylindrically focused optical laser pulse.

sample, rather than through the sample plane, and the shock wave duration can easily be extended to many nanoseconds so that the ISTS acoustic wave frequency can be determined under shock loading conditions. The shock rise time is given by the duration of the shock wave, which is given by the temporal and spatial characteristics of the shock excitation process. A sharp edge (several microns) will yield a fairly sudden rise (about 1 ns) while a broad width could yield a total shock duration of tens of nanoseconds. Moreover, ISTS measurements are not disrupted by the destruction of the sample region that is irradiated by the shock pulse.

7.2.4 Shock Dynamics in Air[*]

Gas expansion is a very complex process which may be understood as a combination of elementary gas dynamic processes where the details of the specific processes and the order in which they occur depend on the chemical and physical nature of the material being ablated [206]. Although the details of each ablation event may vary,

---
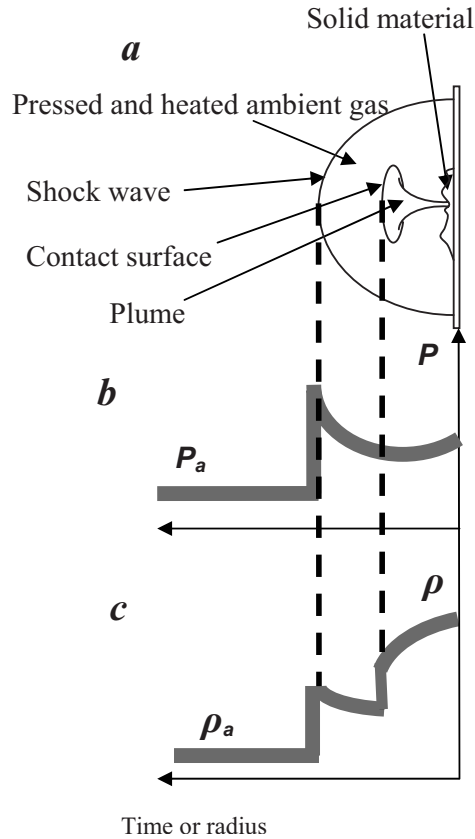
Figure 7-3: Sketches of the ablation process (a) and the corresponding pressure (b) and density (c) distributions [207]. P_a and ρ_a refer to ambient pressure and density respectively at room temperature (298 K) and normal pressure (1 atm).

certain fundamental processes are well known, such as the formation of a shock wave, the propagation of the shock wave into the environment, and the expansion of the newly formed gas into a mushroom-shaped plume that is bounded by the contact surface behind the shock wave (see Figure 7-3).

Future studies will focus on characterization of laser ablation process in air and the expansion of the newly formed gas into the environment. It would be interesting to study this phenomenon as a function of substrate material (e.g. aluminum, gold, etc.) and surrounding gas and laser power to get a better idea of what controls the shock dynamics. Preliminary work has been done and time-resolved raw images have been recorded (as shown in Figure 7-4) to provide a direct dynamic picture of the interesting hybrid ablation process within the 300 ns time window associated with laser-matter interaction. Each time after a image is recorded at a specific time delay, the target is
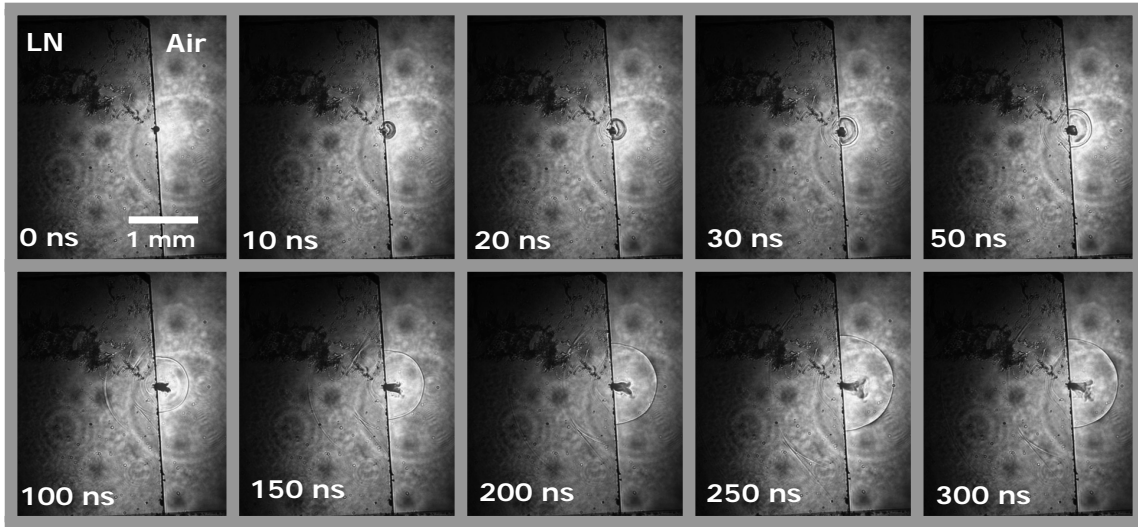
Figure 7-4: Time-resolved raw images of shock wave propagation in air at the indicated time delays after a 200 nm thick aluminum target on the edge of 500 μm thick lithium niobate (LN) crystal is ablated by a 10 ns laser pulse with 100 mJ energy, focused to a 30 μm $\times$ 500 μm spot.
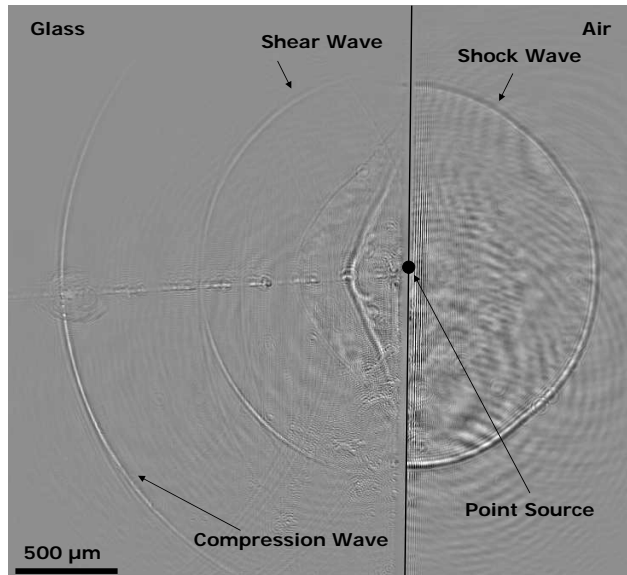
Figure 7-5: Processed image at 300 ns time delay of shock wave propagation. The compression and shear waves are propagating at the speed of 6.0 km/s and 3.5 km/s respectively within 1 mm thick borosilicate glass. The point source refers to the spot where the laser pulse is cylindrically focused to generate shock waves in both glass and air.

shifted to a new position with a fresh area before the next image is taken. The raw images can be processed so as to do background and dark current substraction, and one of the refined image at 300 ns time delay is shown in Figure 7-5. It is obvious that there are compressional (or longitudinal) and shear waves propagating within the glass as well as a shock wave propagating in the air. The direct visualization of waves in solids and air can be exploited to study interesting phenomena of wave propagation and shock dynamics in hybrid environments.

7.2.5 THz Interaction with Shock Fronts*

The portion of the phase diagram reached through shock loading is generally inaccessible by other means, due to the unique combination of density, stress, and temperature. An insulator-to-metal phase transition can occur when the structure of a sample changes due to a change in pressure, temperature, or stress. Because shock waves generate such extreme pressures and stresses, they are capable of introducing metallization in many materials. In silicon, for instance, shock pressures in the range of 10 - 20 GPa can induce metallization [208].

In addition it has been proposed that metallization can be induced at a shock front even for materials that do not undergo a metal-to-insulator phase transition at high static pressures. For a visible probe, a change in reflectivity could result from metallization or band gap narrowing, an effect that is quite possible at these high pressures. To distinguish between metallization and band gap narrowing, we propose to monitor THz reflection off the shock front. Because the THz energy is so low, a large change in reflectivity would only result from complete metallization. The experimental geometry is shown in Figure 7-6. Lithium niobate (LN) crystals are an ideal material to generate terahertz (THz) radiation through impulsive stimulated Raman scattering (ISRS) and to visualize propagating THz waves through a phase-contrast method. Because of these capabilities, the geometry in Figure 7-6 makes it possible to launch the shock wave and the THz and detect them both in a single laser shot.

---

*Done collaboratively with Kit Werley, Johanna Wendlandt Wolfson and Taeho Shin
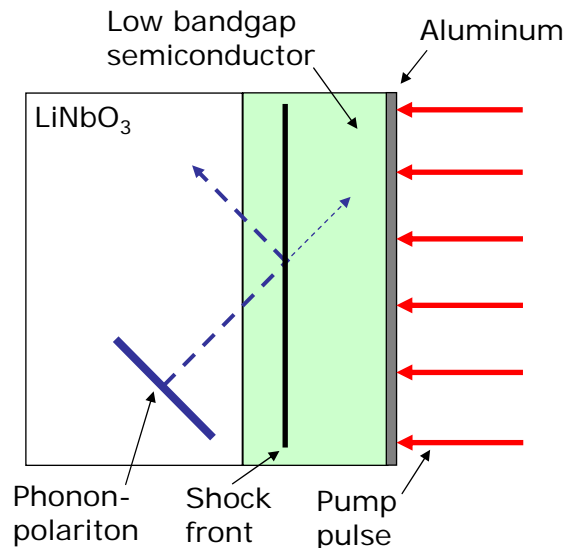
Figure 7-6: Proposed schematic for studying the interaction of terahertz (THz) waves with shock fronts. THz generation is done through impulsive stimulated Raman scattering (ISRS) and THz visualization is done through a phase-contrast method.

Because details at the shock front are not well understood (e.g. thickness of the metallic region due to metallization, change in conductivity which controls the penetration depth of the THz into the metallic region, etc.) it would be wise to initially use some material known to undergo an insulator-metal phase transition at static pressures lower than the shock pressure. Because there is a relatively thick region at this high pressure, it should be relatively easy to visualize the effects with THz, even on a single shot basis. This experiment could provide a proof of principle test for the experimental technique of looking for metallization in the very thin region that is the shock front itself.

7.2.6 Integration with Other Shock Spectroscopies

The optical configuration and sample geometry make shock wave formation and propagation directly accessible to optical imaging and spectroscopic probes with wavelengths ranging from UV to far-IR. The measurement is not disrupted by the destruction of the sample region that is irradiated by the shock pulse. The shock wave duration is given by the width of the ring-focused shock beam, and can easily

be extended to many nanoseconds so that real-time measurements including visible, infrared (IR), impulsive stimulated Raman scattering (ISRS) and terahertz (THz) spectroscopy of sample electronic and vibrational modes can be conducted to determine both molecular and collective material responses to shock. The shock profile can be visualized interferometrically to characterize shock propagation as well as shock-induced sample responses. Pressure and temperature measurements at the focus of shock waves can be conducted by direct optical imaging, black body radiation (IR light emission) and molecular probe using pressure- and temperature-sensitive dyes.

Bibliography

[1] M. A. Meyers. *Dynamic Behavior of Materials.* John Wiley and Sons, Inc., New York, 1994.

[2] S. N. Luo, D. C. Swift, T. E. Tierney IV, D. L. Paisley, G. A. Kyrala, R. P. Johnson, A. A. Hauer, O. Tschauner, and P. D. Asimow. *Laser-induced Shock Waves in Condensed Matter: Some Techniques and Applications. High Pressure Research*, 24(4):409–422, 2004.

[3] R.W. Hertzberg. *Deformation and Fracture Mechanics of Engineering Materials.* John Wiley and Sons, New York, 4th edition, 1996.

[4] C. J. Morath and H. J. Maris. *Phonon Attenuation in Amorphous Solids Studied by Picosecond Ultrasonics. Physical Review B*, 54(1):203–213, 1996.

[5] H. Maris. *Picosecond Ultrasonics. Scientific American*, 278(1):86–89, 1998.

[6] N. Gomopoulos, G. Saini, M. Efremov, P. F. Nealey, K. A. Nelson, and G. Fytas. *Nondestructive Probing of Mechanical Anisotropy in Polyimide Films on Nanoscale. Macromolecules*, 43(3):1551–1555, 2010.

[7] M. Sinha. *Probing Polymer Networks Using Pulse Propagation and Brillouin Light Scattering Techniques.* Ph.D. Dissertation, University of Cincinnati, 2000.

[8] D. H. Torchinsky. *Optical Study of Shear and Longitudinal Acoustic Waves and Complex Relaxation Dynamics of Glass Forming Liquids.* Ph.D. Dissertation, Massachusetts Institute of Technology, Department of Physics, June 2008.

[9] G. Saini, T. Pezeril, D. H. Torchinsky, J. Yoon, S. E. Kooi, E. L. Thomas, and K. A. Nelson. *Pulsed Laser Characterization of Multicomponent Polymer Acoustic and Mechanical Properties in the sub-GHz Regime.* Journal of Materials Research, 22(3):719–723, 2007.

[10] T. F. Crimmins. *Ultrahigh Frequency Characterization of Complex Materials using Transient Grating Techniques.* Ph.D. Dissertation, Massachusetts Institute of Technology, Department of Chemistry, June 2000.

[11] L. Dhar, J. A. Rogers, and K. A. Nelson. *Noncontact Determination of Transverse Isotropic Elastic Moduli in Polyimide Thin Films using a Laser based Ultrasonic Method.* Applied Physics Letters, 65:312–314, 1994.

[12] R. M. Slayton, K. A. Nelson, and A. A. Maznev. *Transient Grating Measurements of Film Thickness in Multilayer Metal Films.* Journal of Applied Physics, 90(9):4392–4402, 2001.

[13] J. A. Rogers, A. A. Maznev, M. J. Banet, and K. A. Nelson. *Optical Generation and Characterization of Acoustic Waves in Thin Films: Fundamentals and Applications.* Annual Review of Materials Science, 30: 117–157, 2000.

[14] J. A. Rogers. *Real Time Impulsive Stimulated Thermal Scattering of Thin Polymer Films.* SM Thesis, Massachusetts Institute of Technology, Department of Chemistry, 1992.

[15] J. A. Rogers. *Time-resolved Photoacoustic and Photothermal Measurements on Surfaces, Thin Films and Multilayer Assemblies.* Ph.D. Dissertation, Massachusetts Institute of Technology, Department of Chemistry, 1995.

[16] Y. X. Yan. Ph.D. Dissertation, Massachusetts Institute of Technology, Department of Physics, 1988.

[17] Y.-X. Yan and K. A. Nelson. *Impulsive Stimulated Light Scattering. I. General Theory.* Journal of Chemical Physics, 87:6240–6256, 1987.

[18] Y.-X. Yan and K. A. Nelson. *Impulsive Stimulated Light Scattering. II. Comparison to Frequency-domain Light Scattering Spectroscopy. Journal of Chemical Physics*, 87:6257–6265, 1987.

[19] A. R. Duggal, J. A. Rogers, K. A. Nelson, and M. Rothschild. *Real-time Characterization of Acoustic Modes of Polyimide Thin Film Coatings using Impulsive Stimulated Thermal Light Scattering. Applied Physics Letters*, 60:692–694, 1992.

[20] Y. W. Yang and K. A. Nelson. *Impulsive Stimulated Light-scattering from Glass-forming Liquids - Generalized Hydrodynamics Approach. Journal of Chemical Physics*, 103(18):7722–7731, 1995.

[21] A. R. Duggal, J. A. Rogers, and K. A. Nelson. *Real-Time Optical Characterization of Surface Acoustic Modes of Polyimide Thin-Film Coatings. Journal of Applied Physics*, 72(7):2823–2839, 1992.

[22] Y. W. Yang, K. A. Nelson, and F. Adibi. *Optical Measurement of the Elastic-moduli and Thermal Diffusivity of a C-N Film. Journal of Materials Research*, 10(1): 41–48, 1995.

[23] S. Silence. *Time-resolved Light Scattering Studies of Structural Rearrangements in Disordered Condensed Phase Systems.* Ph.D. Dissertation, Massachusetts Institute of Technology, Department of Chemistry, 1991.

[24] F. Mammeri, E. Le Bourhis, L. Rozes, and C. Sanchez. *Mechanical Properties of Hybrid Organic-inorganic Materials. Journal of Materials Chemistry*, 15: 3787–3811, 2005.

[25] L. Chazeau, C. Gauthier, G. Vigier, and J. Y. Cavaille. *Relationship Between Microstructural Aspects and Mechanical Properties of Polymer-based Nanocomposites. Handbook of Organic-Inorganic Hybrid Materials and Nanocomposites*, 2: 63–111, 2003.

[26] J. Yoon, W. Lee, J. M. Caruge, M. Bawendi, E. L. Thomas, S. E. Kooi, and P. N. Prasad. *Defect-mode Mirrorless Lasing in Dye-doped Organic/Inorganic Hybrid One-dimensional Photonic Crystal. Applied Physics Letters*, 88(9):091102, 2006.

[27] T. Gorishnyy, C. Ullal, M. Maldovan, G. Fytas, and E. L. Thomas. *Hypersonic Phononic Crystals. Physical Review Letters*, 94(11), 2005.

[28] G. Lu and T. X. Yu. *Energy Absorption of Structures and Materials.* Cambridge, Woodhead Publications, Boca Raton, CRC Press, 2003.

[29] N. A. Vachhani. *Using Narrowband Pulse-shaping to Characterize Polymer Structure and Dynamics: Deathstar GHz Spectroscopy.* SM Thesis, Massachusetts Institute of Technology, Department of Materials Science and Engineering, 2005.

[30] D. P. Dandekar, B. A. M. Vaughan, and W. G. Proud. *Shear Strength of Aluminum Oxynitride. American Institute of Physics Conference Proceedings*, 2007.

[31] T. Hartnett, S. D. Bernstein, E. A. Maguire, and R. W. Tustison. *Optical Properties of Aluminum Oxynitride. Infrared Physics & Technology*, 39(4):203–211, 1998.

[32] W. Xiao and X. Jiang. *Optical and Mechanical Properties of Nanocrystalline Aluminum Oxynitride Films prepared by Electron Cyclotron Resonance Plasma Enhanced Chemical Vapor Deposition. Journal of Crystal Growth*, 264(1-3):165–171, 2004.

[33] S. Dreer, R. Krismer, P. Wilhartitz, and G. Friedbacher. *Statistical Evaluation of Refractive Index, Growth Rate, Hardness and Young's Modulus of Aluminium Oxynitride Films. Thin Solid Films*, 354(1-2):43–49, 1999.

[34] N. D. Corbin. *Aluminum Oxynitride Spinel: A Review. Journal of the European Ceramic Society*, 5:143–154, 1989.

[35] K. J. McClellan, F. Chu, and J. M. Roper. *Room Temperature Single Crystal Elastic Constants of Boron Carbide. Journal of Materials Science*, 36(14):3403–3407, 2001.

[36] O. Conde, A. J. Silvestre, and J. C. Oliveira. *Influence of Carbon Content on the Crystallographic Structure of Boron Carbide Films. Surface and Coatings Technology*, 125(1-3):141–146, 2000.

[37] J. Sun, H. Ling, W. J. Pan, N. Xu, Z. F. Ying, W. D. Shen, and J. D. Wu. *Chemical Structure and Micro-Mechanical Properties of Ultra-Thin Films of Boron Carbide Prepared by Pulsed-Laser Deposition. Tribology Letters*, 17(1):99–104, 2004.

[38] E. Scolan and C. Sanchez. *Energy Absorption of Structures and Materials. Chemistry of Materials*, 10:3217, 1998.

[39] D. R. Lide. *CRC Handbook of Chemistry and Physics.* CRC Press, New York, 84th edition, 2003.

[40] J. A. Howarter and J. P. Youngblood. *Optimization of Silica Silanization by 3–Aminopropyltriethoxysilane. Langmuir*, 22(26):11142–11147, 2006.

[41] J. Brandrup, E. H. Immergut, and E. A. Grulke. *Polymer Handbook.* Wiley-Interscience, New York, 1999.

[42] W. P. Minnear and R. C. Bradt. *Elastic Properties of Polycrystalline TiO_{2-x}. Journal of American Ceramic Society*, 60(9-10):458–459, 1977.

[43] F. M. Ashby and D. R. H. Jones. *Engineering Materials*, volume 1. Butterworth-Heinemann, Oxford, 2nd edition, 1996.

[44] D. P. Dandekar. *Private Communication*, 2008.

[45] J. K. Cocson, C. S. Hau, P. M. Lee, C. C. Poon, A. H. Zhong, J. A. Rogers, and K. A. Nelson. *Transverse Isotropic Elastic Moduli and In-plane Thermal Diffusivity in Silicon-supported Thin Films of a Photosensitive Polyimide Measured*

Using Impulsive Stimulated Thermal Scattering. *Polymer*, 36(21):4069–4075, 1995.

[46] *PI-2600 Series - Low Stress Polyimides*. HD MicroSystems, 250 Cheesequake Road, Parlin, NJ 08859, *www.hdmicrosystems.com*.

[47] K. Miyake, N Satomi, and S. Sasaki. *Elastic Modulus of Polystyrene Film from Near Surface to Bulk Measured by Nanoindentation using Atomic Force Microscopy*. *Applied Physics Letters*, 89:031925, 2006.

[48] P. H. Mott, J. R. Dorgan, and C. M. Roland. *The Bulk Modulus and Poisson's Ratio of Incompressible Materials*. *Journal of Sound and Vibration*, 312:572–575, 2008.

[49] O. Wolff and D. Johannsmann. *Shear Moduli of Polystyrene Thin Films Determined with Quartz Crystal Resonators in the Sandwich Configuration*. *Journal of Applied Physics*, 87(9):4182–4188, 2000.

[50] M. Chen, J. W. McCauley, and K. J. Hemker. *Shock-Induced Localized Amorphization in Boron Carbide*. *Science*, 299(5612):1563–1566, 2003.

[51] T. Sekine, X. Li, T. Kobayashi, Y. Yamashita, P. Patel, and J. W. McCauley. *Aluminum Oxynitride at Pressures up to 180 GPa*. *Journal of Applied Physics*, 94(8):4803–4806, 2003.

[52] D. B. Hayes. *Introduction to Stress Wave Phenomena*. Sandia National Laboratories, Albuquerque, 1973.

[53] D. D. Dlott. *Ultrafast Spectroscopy of Shock Waves in Molecular Materials*. *Annual Review of Physical Chemistry*, 50:251–278, 1999.

[54] D. D. Dlott. *Nanoshocks in Molecular Materials*. *Accounts of Chemical Research*, 33(1):37–45, 2000.

[55] T. J. Ahrens. *Rock Physics and Phase Relations*, Volume 3, Chapter - Shock Wave Data for Rocks (35-44), American Geophysical Union, 1995.

[56] S. P. Marsh. *LASL Shock Hugoniot Data.* University of California Press, Berkeley, CA, 1980.

[57] Y. B. Zel'dovich and Y. P. Raiser. *Physics of Shock Waves and High-temperature Hydrodynamic Phenomena.* Academic Press, New York, 1967.

[58] A. D. Mulliken. *Mechanics of Amorphous Polymers and Polymer Nanocomposites during High Rate Deformation.* Ph.D. Dissertation, Massachusetts Institute of Technology, Department of Mechanical Engineering, 2006.

[59] C. León, K. L. Ngai, and C. M. Roland. *Relationship between the Primary and Secondary Dielectric Relaxation Processes in Propylene Glycol and its Oligomers. Journal of Chemical Physics*, 110(23):11585–11591, 1999.

[60] S. S. Sarva, S. Deschanel, M. C. Boyce, and W. Chen. *Stress-strain Behavior of a Polyurea and a Polyurethane from Low to High Strain Rates. Polymer*, 48:2208–2213, 2007.

[61] J. D. Ferry. *Viscoelastic Properties of Polymers.* Wiley, New York, 1961.

[62] M. V. Zhernokletov and B. L. Glushak. *Material Properties under Intensive Dynamic Loading.* Springer, Inc., New York, 2006.

[63] S. M. Walley, J. E. Field, P. H. Pope, and N. A. Safford. *The Rapid Deformation-Behavior of Various Polymers. Journal De Physique III*, 1(12):1889–1925, 1991.

[64] J. Dunn, D. F. Price, S. J. Moon, R. C. Cauble, P. T. Springer, and A. Ng. *1-10 Mbar Laser-driven Shocks using the Janus Laser Facility. AIP Conference Proceedings*, 620(Part 2):1371, 2002.

[65] Y. M. Gupta. *Determination of the Impact Response of PMMA using Combined Compression and Shear Loading. Journal of Applied Physics*, 51(10):5352–5361, 1980.

[66] N. Hemmi, D. H. Torchinsky, K. A. Zimmerman, J. M. Winey, K. A. Nelson, and Y. M. Gupta. *Photoacoustic Measurements to Determine Acoustic Velocities in Shocked Condensed Materials: Application to Liquid Benzene*. Applied Physics Letters, 92(10):101926, 2008.

[67] D. E. Hare, J. Franken, and D. D. Dlott. *Coherent Raman Measurements of Polymer Thin-film Pressure and Temperature during Picosecond Laser Ablation*. Journal of Applied Physics, 77(11):5950–5960, 1995.

[68] C. A. Bolme. *Ultrafast Dynamic Ellipsometry of Laser Driven Shock Waves*. Ph.D. Dissertation, Massachusetts Institute of Technology, Department of Chemistry, September 2008.

[69] K. P. Leung, S. S. Yao, A. G. Doukas, R. R. Alfano, and P. Harris. *Photoluminescence Determination of the Pressure and Temperature of the Shock Wave Induced by a Picosecond Laser Pulse in the Layered Semiconductor GaSe*. Physical Review B, 31(2):942–946, 1985.

[70] X. Z. Lu, R. Rao, B. Wilman, S. Lee, A. G. Doukas, and R. R. Alfano. *Effect of Picosecond Laser-driven Shock Waves on Spontaneous and Stimulated Emissions in GaSe*. Physical Review B, 35(14):7515–7519, 1987.

[71] X. A. Shen and Y. M. Gupta. *Shock-induced Fluorescence Shift of Rhodamine-6G in Ethanol Solution*. Journal of Applied Physics, 70(12):7549–7553, 1991.

[72] Y. A. Gruzdkov and Y. M. Gupta. *Emission and Fluorescence Spectroscopy to Examine Shock-induced Decomposition in Nitromethane*. Journal of Physical Chemistry A, 102(43):8325–8332, 1998.

[73] N. C. Holmes, W. J. Nellis, W. B. Graham, and G. E. Walrafen. *Spontaneous Raman Spectroscopy of Shocked Water*. Physica B+C, 139:568–570, 1986.

[74] T. Kobayashi and T. Sekine. *In-situ Raman Spectroscopy of Shock-compressed Benzene and its Derivatives*. Physical Review B (Condensed Matter and Materials Physics), 62(9):5281–5284, 2000.

[75] M. Nicol, M. L. Johnson, and N. C. Holmes. *Chemiluminescence of Shock-pyrolyzed Benzene. Physica B+C*, 139:582–586, 1986.

[76] G. I. Pangilinan and Y. M. Gupta. *Time-resolved Raman Measurements in Nitromethane Shocked to 140 kbar. Journal of Physical Chemistry*, 98(17):4522–4529, 1994.

[77] G. I. Pangilinan and Y. M. Gupta. *Use of Time-resolved Raman scattering to Determine Temperatures in Shocked Carbon Tetrachloride. Journal of Applied Physics*, 81(10):6662–6669, 1997.

[78] A. M. Renlund, S. A. Sheffield, and W. M. Trott. *Time-resolved Infrared Spectral Photography Studies of Shock-induced Chemistry in Carbon Disulfide. Shock Waves in Condensed Matter*, 237-242, 1986.

[79] D. D. Dlott, S. Hambir, and J. Franken. *The New Wave in Shock Waves. Journal of Physical Chemistry B*, 102(12):2121–2130, 1998.

[80] J. Franken, S. Hambir, D. E. Hare, and D. D. Dlott. *Shock Waves in Molecular Solids: Ultrafast Vibrational Spectroscopy of the First Nanosecond. Shock Waves*, 7(3):135–145, 1997.

[81] S. A. Hambir, J. Franken, D. E. Hare, E. L. Chronister, B. J. Baer, and D. D. Dlott. *Ultrahigh Time-resolution Vibrational Spectroscopy of Shocked Molecular Solids. Journal of Applied Physics*, 81(5):2157–2166, 1997.

[82] L. Davison and M. Shahinpoor. *High-Pressure Shock Compression of Solids III.* Springer, Inc., New York, 1998.

[83] G. E. Duvall, K. M. Ogilvie, R. Wilson, P. M. Bellamy, and P. S. P. Wei. *Optical Spectroscopy in a Shocked Liquid. Nature*, 296:846–848, 1982.

[84] S. D. McGrane, D. S. Moore, and D.J. Funk. *Shock Induced Reaction Observed via Ultrafast Infrared Absorption in Poly(vinyl nitrate) Films. Journal of Physical Chemistry A*, 108(43):93429347, 2004.

[85] T. de Rességuier, L. Signor, A. Dragon, M. Boustie, G. Roy, and F. Llorca. *Experimental Investigation of Liquid Spall in Laser Shock-loeaded Tin. Journal of Applied Physics*, 101(1):013506, 2007.

[86] S. M. Gallivan and Y. M. Gupta. *Study of Tensile Deformation in Shocked Z-cut, α–quartz using Time-resolved Raman Spectroscopy. Journal of Applied Physics*, 78(3):1557–1564, 1995.

[87] A. Matsuda, K. G. Nakamura, and K. Kondo. *Time-resolved Raman Spectroscopy of Benzene and Cyclohexane under Laser-driven Shock Compression. Physical Review B*, 65(17):174116, 2002.

[88] K. G. Nakamura, K. Wakabayashi, and K. Kondo. *Transient Bond Scission of Polytetrafluoroethylene under Laser-induced Shock Compression studied by Nanosecond Time-resolved Raman spectroscopy. AIP Conference Proceedings*, 620(Part 2):1259, 2002.

[89] H. Kim, S. A. Hambir, and D. D. Dlott. *Ultrafast High Repetition Rate Absorption Spectroscopy of Polymer Shock Compression. Shock Waves*, 12(1):79–86, 2002.

[90] S. A. Hambir, J. Franken, D. E. Hare, E. L. Chronister, B. J. Baer, and D. D. Dlott. *Ultrahigh Time-resolution Vibrational Spectroscopy of Shocked Molecular Solids. Journal of Applied Physics*, 81(5):2157–2166, 1997.

[91] S. A. Hambir, H. Kim, and D. D. Dlott. *Ultrafast Dynamics of Nanoshocks in Molecular Materials. AIP Conference Proceedings*, 505(Part 2):945, 2000.

[92] G. Tas, S. A. Hambir, J. Franken, D. E. Hare, and D. D. Dlott. *Coherent Raman Spectroscopy of Nanoshocks. Journal of Applied Physics*, 82(3):1080–1087, 1997.

[93] A. S. Lagutchev, J. E. Patterson, W. T. Huang, and D. D. Dlott. *Ultrafast Dynamics of Self-assembled Monolayers under Shock Compression: Effects of Molecular and Substrate Structure. Journal of Physical Chemistry B*, 109(11):5033–5044, 2005.

[94] J. Franken, S. A. Hambir, and D. D. Dlott. *Ultrafast Shock-induced Orientation of Polycrystalline Films: Applications to High Explosives. Journal of Applied Physics*, 85(4):2068–2074, 1999.

[95] L. Davison, D. E. Grady, and M. Shahinpoor. *High-Pressure Shock Compression of Solids II.* Springer, Inc., New York, 1996.

[96] V. E. Fortov, R. F. Trunin, L. V. Al'tshuler, and A. I. Funtikov. *High-Pressure Shock Compression of Solids VII.* Springer, Inc., New York, 2004.

[97] L. M. Barker and R. E. Hollenbach. *Laser Interferometer for Measuring High Velocities of Any Reflecting Surface. Journal of Applied Physics*, 43(11):4669–4675, 1972.

[98] O. T. Strand, L. V. Berzins, D. R. Goosman, W. W. Kuhlow, P. D. Sargis, and T. L. Whitworth. *Velocimetry Using Heterodyne Techniques. Proceedings of SPIE - The International Society for Optical Engineering*, 5580:593–599, 2005.

[99] J. S. Wark, R. R. Whitlock, A. A. Hauer, J. E. Swain, and P. J. Solone. *Sub-nanosecond X-ray Diffraction from Laser-shocked Crystals. Physical Review B*, 40(8):5705–5714, 1989.

[100] P. A. Rigg and Y. M. Gupta. *Real-time X-ray Diffraction to Examine Elastic-Plastic Deformation in Shocked Lithium Fluoride Crystals. Applied Physics Letter*, 73(12):1655–1657, 1998.

[101] Q. Johnson and A. C. Mitchell. *First X-Ray Diffraction Evidence for a Phase Transition during Shock-Wave Compression. Physical Review Letter*, 29(20):1369–1371, 1972.

[102] T. d'Almeida and Y. M. Gupta. *Real-Time X-Ray Diffraction Measurements of the Phase Transition in KCl Shocked along [100]. Physical Review Letter*, 85(2):330–333, 2000.

[103] J. P. Geindre, P. Audebert, A. Rousse, F. Fallies, J. C. Gauthier, A. Mysyrowicz, A. Dos Santos, G. Hamoniaux, and A. Antonetti. *Frequency-domain Interferometer for Measuring the Phase and Amplitude of a Femtosecond Pulse Probing a Laser-produced Plasma. Optics Letters*, 19(23):1997–1999, 1994.

[104] E. Tokunaga, A. Terasaki, and T. Kobayashi. *Frequency-domain Interferometer for Femtosecond Time-resolved Phase Spectroscopy. Optics Letters*, 17(16):1131–1133, 1992.

[105] R. Evans, A. D. Badger, F. Fallies, M. Mahdieh, T. A. Hall, P. Audebert, J. P. Geindre, J. C. Gauthier, A. Mysyrowicz, G. Grillon, and A. Antonetti. *Time- and Space-resolved Optical Probing of Femtosecond Laser-driven Shock Waves in Aluminum. Physical Review Letters*, 77(16):3359–3362, 1996.

[106] K. T. Gahagan, D. S. Moore, D. J. Funk, R. L. Rabie, S. J. Buelow, and J. W. Nicholson. *Measurement of Shock Wave Rise Times in Metal Thin Films. Physical Review Letters*, 85(15):3205–3208, 2000.

[107] A. Benuzzi-Mounaix, M. Koenig, J. M. Boudenne, T. A. Hall, D. Batani, F. Scianitti, A. Masini, and D. Di Santo. *Chirped Pulse Reflectivity and Frequency-domain Interferometry in Laser-driven Shock Experiments. Physical Review E*, 60(3):R2488–R2491, 1999.

[108] J. P. Chen, R. X. Li, Z. N. Zeng, X. T. Wang, W. Y. Wang, Y. H. Jiang, C. F. Cheng, and Z. Z. Xu. *Simultaneous Measurement of Laser-induced Shock Wave and Released Particle Velocities at Mbar Pressure. Journal of Applied Physics*, 94(2):858–862, 2003.

[109] C. Quoix, G. Hamoniaux, A. Antonetti, J.C. Gauthier, J. P. Geindre, and P. Audebert. *Ultrafast Plasma Studies by Phase and Amplitude Measurements with Femtosecond Spectral Interferometry. Journal of Quantitative Spectroscopy and Radiative Transfer*, 65(1):455–462, 2000.

[110] D. J. Funk, D. S. Moore, K. T. Gahagan, S. J. Buelow, J. H. Reho, G. L. Fisher, and R. L. Rabie. *Ultrafast Measurement of the Optical Properties of Aluminum during Shock-wave Breakout. Physical Review B*, 64(11), 2001.

[111] S. D. McGrane, D. S. Moore, and D. J. Funk. *Ultrafast Spectroscopy and Interferometry of Laser-shocked Thin Films: Practical Considerations. Proceedings of the SPIE - The International Society for Optical Engineering*, 5448(1):165–170, 2004.

[112] T. de Rességuier, S. Couturier, M. Boustie, J. David, G. Nierat, and F. Bauer. *Characterization of Laser-driven Shocks of High Intensity using Piezoelectric Polymers. Journal of Applied Physics*, 80(7):3656–3661, 1996.

[113] D. J. Funk, D. S. Moore, S. D. McGrane, K. T. Gahagan, J. H. Reho, S. J. Buelow, J. Nicholson, G. L. Fisher, and R. L. Rabie. *Ultrafast Studies of Shock Waves using Interferometric Methods and Transient Infrared Absorption Spectroscopy. Thin Solid Films*, 453:542–549, 2004.

[114] S. D. McGrane, D. S. Moore, and D. J. Funk. *Sub-picosecond Shock Interferometry of Transparent Thin Films. Journal of Applied Physics*, 93(9):5063–5068, 2003.

[115] S. D. McGrane, D. S. Moore, and D. J. Funk. *Measurement of Shocked Thin Polymer Film Hugoniot Properties with Ultrafast Dynamic Ellipsometry. AIP Conference Proceedings*, 706:1181–1186, 2004.

[116] D. J. Funk, D. S. Moore, S. D. McGrane, J. H. Reho, and R. L. Rabie. *Ultra-fast Spatial Interferometry: A Tool for Characterizing Material Phase and Hydrodynamic Motion in Laser-excited Metals. Applied Physics A-Materials Science and Processing*, 81(2):295–302, 2005.

[117] D. S. Moore, D. J. Funk, K. T. Gahagan, J. H. Reho, G. L. Fisher, S. D. McGrane, and R. L. Rabie. *Sub-picosecond Laser-driven Shocks in Metals and Energetic Materials. AIP Conference Proceedings*, 620(Part 2):1333, 2002.

[118] D. S. Moore, K. T. Gahagan, S. J. Buelow, R. L. Rabie, D. J. Funk, S. A. Sheffield, L. L. Davis, T. Lippert, H. Brand, and J. W. Nicholson. *Time- and Space-resolved Optical Probing of the Shock Rise Time in Thin Aluminum Films. AIP Conference Proceedings*, 505(Part 2):1003–1006, 2000.

[119] K. T. Gahagan, J. H. Reho, D. S. Moore, D. J. Funk, and R. L. Rabie. *Ultrafast Time-resolved 2D Spatial Interferometry for Shock Wave Characterization in Metal Films. AIP Conference Proceedings*, 620(Part 2):1351–1354, 2002.

[120] D. J. Funk, D. S. Moore, J. H. Reho, K. T. Gahagan, S. D. McGrane, and R. L. Rabie. *Ultrafast Measurement of the Optical Properties of Shocked Nickel and Laser Heated Gold. AIP Conference Proceedings*, 620:1227–1230, 2002.

[121] C. A. Bolme, S. D. McGrane, D. S. Moore, and D. J. Funk. *Single Shot Measurements of Laser-driven Shock Waves using Ultrafast Dynamic Ellipsometry. Journal of Applied Physics*, 102(3):033513, 2007.

[122] D. S. Moore, K. T. Gahagan, J. H. Reho, D. J. Funk, S. J. Buelow, R. L. Rabie, and T. Lippert. *Ultrafast Nonlinear Optical Method for Generation of Planar Shocks. Applied Physics Letters*, 78(1):40–42, 2001.

[123] S. D. McGrane, D. S. Moore, D. J. Funk, and R. L. Rabie. *Spectrally Modified Chirped Pulse Generation of Sustained Shock Waves. Applied Physics Letters*, 80(21):3919–3921, 2002.

[124] K. T. Gahagan, D. S. Moore, D. J. Funk, J. H. Reho, and R. L. Rabie. *Ultrafast Interferometric Microscopy for Laser-driven Shock Wave Characterization. Journal of Applied Physics*, 92(7):3679–3682, 2002.

[125] R. G. McQueen, S. P. Marsh, J. W. Taylor, J. N. Fritz, and W. J. Carter. *High Velocity Impact Phenomena*. Academic, New York, 1970.

[126] J. R. Asay and D. B. Hayes. *Shock Compression and Release Behavior near Melt States in Aluminum. Journal of Applied Physics*, 46(11):4789–4800, 1975.

[127] S. H. Phillips, T. S. Haddad, and S. J. Tomczak. *Developments in Nanoscience: Polyhedral Oligomeric Silsesquioxane (POSS)-Polymers. Current Opinion in Solid State and Materials Science*, 8(1):21–29, 2004.

[128] Z. Zhang and G. Gogos. *Theory of Shock Wave Propagation During Laser Ablation. Physical Review B (Condensed Matter and Materials Physics)*, 69(23):235403/1–235403/9, 2004.

[129] I. Y. S. Lee, J. R. Hill, H. Suzuki, D. D. Dlott, B. J. Baer, and E. L. Chronister. *Molecular-Dynamics Observed 60 ps Behind a Solid-State Shock Front. Journal of Chemical Physics*, 103(19):8313–8321, 1995.

[130] H. Matsuo and Y. Nakamura. *Experiments on Cylindrically Converging Blast Waves in Atmospheric Air. Journal of Applied Physics*, 51(6):3126–3129, 1980.

[131] H. Matsuo and Y. Nakamura. *Cylindrically Converging Blast Waves in Air. Journal of Applied Physics*, 52(7):4503–4507, 1981.

[132] A. Ramu and M. P. Ranga Rao. *Converging Spherical and Cylindrical Shock Waves. Journal of Engineering Mathematics*, 27:411–417, 1993.

[133] M. Koenig *et al. High Pressures Generated by Laser Driven Shocks: Applications to Planetary Physics. Nuclear Fusion*, 44:S208–S214, 2004.

[134] K. Takayama and T. Saito. *Shock Wave - Geophysical and Medical Applications. Annual Review of Fluid Mechanics*, 36:347–379, 2004.

[135] K. P. Stanyukovich. *Unsteady Motion of Continuous Media.* Oxford: Pergamon Press, 1960.

[136] M. Van Dyke and A. J. Guttmann. *The Converging Shock Wave from a Spherical or Cylindrical Piston. Journal of Fluid Mechanics*, 120:451–462, 1982.

[137] K. G. Guderley. *Starke Kugelige und Zylindrische Verdichtungsstöße in der Nähe des Kugelmittelpunktes bzw. der Zylinderachse (German) or Powerful*

Spherical and Cylindrical Compression of Shocks in Neighbourhood of the Spherical and Cylindrical Axis (English). Luftfahrt-Forschung, 19(9):302–312, 1942.

[138] R. W. Perry and A. Kantrowitz. *The Production and Stability of Converging Shock Waves. Journal of Applied Physics*, 22(7):878–886, 1951.

[139] H. Matsuo. *Converging Shock Waves Generated by Instantaneous Energy Release over Cylindrical Surfaces. Physics of Fluids*, 22(9):1618–1622, 1979.

[140] J. H. Lee and B. H. K. Lee. *Cylindrical Imploding Shock Waves. Physics of Fluids*, 8(12):2148–2152, 1965.

[141] M. Watanabe and K. Takayama. *Stability of Converging Cylindrical Shock Waves. Shock Waves*, 1(2):149–160, 1991.

[142] K. Takayama, O. Onodera, and Y. Hoshizawa. *Experiments on the Stability of Converging Cylindrical Shock Waves. Advances in Theoretical and Applied Mechanics*, 32:117–127, 1984.

[143] K. Takayama, H. Kleine, and H. Grönig. *An Experimental Investigation of the Stability of Converging Cylindrical Shock Waves in Air. Experiments in Fluids*, 5(5):315–322, 1987.

[144] J. H. T. Wu, R. A. Neemeh, and P. P. Ostrowski. *Experimental Studies of the Production of Converging Cylindrical Shock Waves. American Institute of Aeronautics and Astronautics Journal*, 18(1):47–48, 1980.

[145] K. Fong and B. Ahlborn. *Stability of Converging Shock Waves. Physics of Fluids*, 22(3):416–421, 1979.

[146] J. C. T. Wang. *On the Theory of Imploding Shocks. Journal of Applied Mathematics and Physics*, 33(1):53–62, 1982.

[147] R. B. Lazarus. *One Dimensional Stability of Self-similar Converging Flows. Physics of Fluids*, 25(7):1146–1155, 1982.

[148] V. Eliasson, N. Apazidis, N. Tillmark, and M. B. Lesser. *Focusing of Strong Shocks in an Annular Shock Tube. Shock Waves*, 15:205–217, 2006.

[149] H. Matsuo, K. Ebihara, and Y. Ohya. *Spectroscopic Study of Cylindrically Converging Shock Waves. Journal of Applied Physics*, 58(7):2487–2491, 1985.

[150] S. G. Kelly and A. H. Nayfeh. *Non-linear Propagation of Directional Spherical Waves. Journal of Sound and Vibration*, 72(1):25–37, 1980.

[151] S. G. Kelly and A. H. Nayfeh. *Non-linear Propagation of General Directional Spherical Waves. Journal of Sound and Vibration*, 79(1):145–156, 1981.

[152] H. Matsuo, Y. Ohya, K. Fujiwara, and H. Kudoh. *Numerical Simulation of Cylindrically Converging Shock Waves. Journal of Computational Physics*, 75(2):384–399, 1988.

[153] R. C. Srivastava, D. Leutloff, K. G. Roesner, and K. Kuwahara. *Numerical Investigations of Converging Cylindrical and Spherical Shock Waves. Astrophysics and Space Science*, 192(1):1–9, 1992.

[154] P. A. Bélanger and M. Rioux. *Ring Pattern of a Lens-Axicon Doublet Illuminated by a Gaussian Beam. Applied Optics*, 17(7):1080–1086, 1978.

[155] M. de Angelis, L. Cacciapuoti, G. Pierattini, and G. M. Tino. *Axially Symmetric Hollow Beams using Refractive Conical Lenses. Optics and Lasers in Engineering*, 39:283–291, 2003.

[156] Y. Yang, S. Wang, Z. Sun, and D. D. Dlott. *Near-Infrared and Visible Absorption Spectroscopy of Nano-Energetic Materials Containing Aluminum and Boron. Propellants, Explosives, Pyrotechnics*, 30(3):171–177, 2005.

[157] Y. Yang, S. Wang, Z. Sun, and D. D. Dlott. *Near-Infrared Laser Ablation of Polytetrafluoroethylene (Teflon) Sensitized by Nanoenergetic Materials. Applied Physics Letters*, 85(9):1493–1495, 2004.

[158] X. Wen, D. E. Hare, and D. D. Dlott. *Laser Polymer Ablation Threshold Lowered by Nanometer Hot Spots. Applied Physics Letters*, 64(2):184–186, 1994.

[159] Y. Yang, S. Wang, Z. Sun, and D. D. Dlott. *Propagation of Shock-induced Chemistry in Nanoenergetic Materials: The First Micrometer. Journal of Applied Physics*, 95(7):3667–3676, 2004.

[160] J. E. Patterson, A. S. Lagutchev, S. A. Hambir, W. Huang, H. Yu, and D. D. Dlott. *Time- and Space-resolved Studies of Shock Compression Molecular Dynamics. Shock Waves*, 14(5-6):391–402, 2005.

[161] Y. Yang, Z. Sun, S. Wang, and D. D. Dlott. *Fast Spectroscopy of Laser-Initiated Nanoenergetic Materials. Journal of Physical Chemistry B*, 107(19):4485–4493, 2003.

[162] S. Katsuki, K. Tanaka, T. Fudamoto, and T. Namihira. *Shock Waves due to Pulsed Streamer Discharges in Water. Japanese Journal of Applied Physics*, 45(1A):239–242, 2006.

[163] A. C. Mitchell and W. J. Nellis. *Equation of State and Electrical Conductivity of Water and Ammonia Shocked to the 100 GPa (1 Mbar) Pressure Range. Journal of Chemical Physics*, 76(12):6273–6281, 1982.

[164] J. M. Walsh and M. H. Rice. *Dynamic Compression of Liquids from Measurements on Strong Shock Waves. Journal of Chemical Physics*, 26(4):815–823, 1957.

[165] A. P. Rybakov and I. A. Rybakov. *Reaction of Condensed Matter to Extremely Short-duration and Intense Loading - Strength of Solids and Liquids Under Dynamic Grooming. European Journal of Mechanics - B/Fluids*, 14(2):197–205, 1995.

[166] M. Nakahara, K. Nagayama, and Y. Mori. *Shock Wave Dynamics of High Pressure Pulse in Water and Other Biological Materials Based on Hugoniot Data. Japanese Journal of Applied Physics*, 47(5):3510–3517, 2008.

[167] J. R. Swider, V. A. Hackley, and J. Winter. *Characterization of Chinese Ink in Size and Surface. Journal of Cultural Heritage*, 4:175–186, 2003.

[168] G. X. Chen, M. H. Hong, T. C. Chong, H. I. Elim, G. H. Ma, and W. Ji. *Preparation of Carbon Nanoparticles with Strong Optical Limiting Properties by Laser Ablation in Water. Journal of Applied Physics*, 95(3):1455–1459, 2004.

[169] Z. F. Li, G. H. Luo, W. P. Zhou, F. Wei, R. Xiang, and Y. P. Liu. *The Quantitative Characterization of the Concentration and Dispersion of Multi-walled Carbon Nanotubes in Suspension by Spectrophotometry. Nanotechnology*, 17:3692–3698, 2006.

[170] K. Nagayama, Y. Mori, K. Shimada, and M. Nakahara. *Shock Hugoniot Compression Curve for Water up to 1 GPa by Using a Compressed Gas Gun. Journal of Applied Physics*, 91(1):476–482, 2002.

[171] M. Takeda, H. Ina, and S. Kobayashi. *Fourier Transform Method of Fringe Pattern Analysis for Computer based Topography and Interferometry. Journal of the Optical Society of America*, 72(1):156–160, 1982.

[172] J. H. Gladstone and T. P. Dale. *Researches on the Refraction, Dispersion, and Sensitiveness of Liquids. Philosophical Transactions of the Royal Society of London*, 153:317–343, 1863.

[173] H. S. Yadav, D. S. Murty, S. N. Verma, K. H. C. Sinha, B. M. Gupta, and D. Chand. *Measurement of Refractive Index of Water under High Dynamic Pressures. Journal of Applied Physics*, 44(5):2197–2200, 1973.

[174] C. Glorieux, K. Van de Rostyne, and V. Gusev. *Nonlinearity of Acoustic Waves at Solid-Liquid Interfaces. Journal of the Acoustical Society of America*, 111(1):95–103, 2002.

[175] C. K. Jen, P. Cielo, J. Bussiere, F. Nadeau, and G. W. Farnell. *Phase Variation of Focused Surface Acoustic Wave. Applied Physics Letters*, 46(3):241–243, 1985.

[176] M. Campbell, D. N. Sharp, M. T. Harrison, R. G. Denning, and A. J. Turberfield. *Fabrication of Photonic Crystals for the Visible Spectrum by Holographic Lithography*. Nature, 404(6773):53–56, 2000.

[177] Yu. V. Miklyaev, D. C. Meisel, A. Blanco, G. von Freymann, K. Busch, W. Koch, C. Enrich, M. Deubel, and M. Wegener. *Three-dimensional Face-Centered-Cubic Photonic Crystal Templates by Laser Holography: Fabrication, Optical Characterization, and Band-structure Calculations*. Applied Physics Letters, 82(8):1284–1286, 2003.

[178] P. J. Hogg. *Composites in Armor*. Science, 314(5802):1100–1101, 2006.

[179] S. Jeon, J. U. Park, R. Cirelli, S. Yang, C. E. Heitzman, P. V. Braun, P. J. A. Kenis, and J. A. Rogers. *Fabricating Complex Three-dimensional Nanostructures with High-resolution Conformable Phase Masks*. Proceedings of the National Academy of Sciences, 101(34):12428–12433, 2004.

[180] L. Martí-López, R. Ocaña, J. A. Porro, M. Morales, and J. L. Ocaña. *Optical Observation of Shock Waves and Cavitation Bubbles in High Intensity Laser-induced Shock Processes*. Applied Optics, 48(19):3671–3680, 2009.

[181] W. Lauterborn and W. Hentschel. *Cavitation Bubble Dynamics Studied by High Speed Photography and Holography: Part One*. Ultrasonics, 23(6):260–268, 1985.

[182] W. Lauterborn and W. Hentschel. *Cavitation Bubble Dynamics Studied by High Speed Photography and Holography: Part Two*. Ultrasonics, 24(2):59–65, 1986.

[183] G. Paltauf, R. Nuster, M. Haltmeier, and P. Burgholzer. *Photoacoustic Tomography using a MachZehnder Interferometer as an Acoustic Line Detector*. Applied Optics, 46(16):3352–3358, 2007.

[184] T. Balciunas, A. Melninkaitis, G. Tamosauskas, and V. Sirutkaitis. *Time-resolved Off-axis Digital Holography for Characterization of Ultrafast Phenomena in Water*. Optics Letters, 33(1):58–60, 2008.

[185] U. Wernekinck and W. Merzkirch. *Speckle Photography of Spatially Extended Refractive-index Fields. Applied Optics*, 26(1):31–32, 1987.

[186] J. Lapsien and D. Meiners. *Digital Speckle Techniques for Measuring Light Deflection Profiles of inhomogeneous Phase Objects. Applied Optics*, 36(28):7180–7187, 1997.

[187] S. Minardi, A. Gopal, M. Tatarakis, A. Couairon, G. Tamošauskas, R. Piskarskas, A. Dubietis, and P. Di Trapani. *Time-resolved Refractive Index and Absorption Mapping of Light-plasma Filaments in Water. Optics Letters*, 33(1):86–88, 2008.

[188] G. S. Settles. *Schlieren and Shadowgraph Techniques - Visualizing Phenomena in Transparent Media.* Springer-Verlag, New York, 2001.

[189] Y. Nakano and K. Murata. *Measurements of Phase Objects using the Talbot effect and Moiré Techniques. Applied Optics*, 23(14):2296–2299, 1984.

[190] R. Petkovšek, J. Možina, and G. Močnik. *Optodynamic Characterization of the Shock Waves After Laser-induced Breakdown in Water,. Optics Express*, 13(11):4107–4112, 2005.

[191] H. Kleine, H. Grönig, and K. Takayama. *Simultaneous Shadow, Schlieren and Interferometric Visualization of Compressible Flows. Optics and Lasers in Engineering*, 44(3):170–189, 2006.

[192] Y. Mori, K. Shimada, M. Nakahara, and K. Nagayama. *New Water Shock Sensor. Reviews of Scientific Instruments*, 72(4):2123–2127, 2001.

[193] A. Vogel, S. Busch, and U. Parlitz. *Shock Wave Emission and Cavitation Bubble Generation by Picosecond and Nanosecond Optical Breakdown in Water. Journal of the Acoustical Society of America*, 100(1):148–165, 1996.

[194] J. Noack and A. Vogel. *Single-shot Spatially Resolved Characterization of Laser-induced Shock Waves in Water. Applied Optics*, 37(19):4092–4099, 1998.

[195] R. Pecha and B. Gompf. *Microimplosions: Cavitation Collapse and ShockWave Emission on a Nanosecond Time Scale*. Physical Review Letters, 84(6):1328–1330, 2000.

[196] T. Feurer, N. S. Stoyanov, D. W. Ward, and K. A. Nelson. *Direct Visualization of the Gouy Phase by Focusing Phonon-Polaritons*. Physical Review Letters, 88(25):257402, 2002.

[197] N. C. R. Holme, B. C. Daly, M. T. Myaing, and T. B. Norris. *Gouy Phase Shift of Single-Cycle Picosecond Acoustic Pulses. Applied Physics Letters*, 83(2):392–394, 2003.

[198] R. H. Cole. *Underwater Explosions*. Dover Publications Inc., New York, 1965.

[199] N. Kambouchev. *Analysis of Blast Mitigation Strategies Exploiting Fluid-Structure Interaction*. Ph.D. Dissertation, Massachusetts Institute of Technology, Department of Aeronautics and Astronautics, September 2007.

[200] A. Lew, R. Radovitzky, and M. Ortiz. *An Artificial-Viscosity Method for the Lagrangian Analysis of Shocks in Solids with Strength on Unstructured, Arbitrary-Order Tetrahedral Meshes. Journal of Computer-Aided Materials Design*, 8:213–231, 2001.

[201] A. Makris, J. Nerenberg, J. P. Dionne, C. R. Bass, and C. Chichester. *Reduction of Blast Induced Head Acceleration in the Field of Anti-Personnel Mine Clearance*. 2001.

[202] T. Gorishnyy, C. K. Ullal, M. Maldovan, G. Fytas, and E. L. Thomas. *Hypersonic Phononic Crystals. Physical Review Letters*, 94(11):115501/1–115501/4, 2005.

[203] E. J. Reed, M. Soljaččić, and J. D. Joannopoulos. *Color of Shock Waves in Photonic Crystals. Physical Review Letters*, 90(20):203904, 2003.

[204] S. Catheline, J. L. Gennisson, M. Tanter, and M. Fink. *Observation of Shock Transverse Waves in Elastic Media*. Physical Review Letters, 91(16):164301, 2003.

[205] L. Chazeau, C. Gauthier, G. Vigier, and J. Y. Cavaille. *Handbook of Organic-Inorganic Hybrid Materials and Nanocomposites. Relationship Between Microstructural Aspects and Mechanical Properties of Polymer-based Nanocomposites*. Volume 2:63-111. American Scientific Publishers, Stevenson Ranch, CA, 2003.

[206] N. Zhang, X. Zhu, J. Yang, X. Wang, and M. Wang. *Time-resolved Shadowgraphs of Material Ejection in Intense Femtosecond Laser Ablation of Aluminum*. Physical Review Letters, 99(16):167602, 2007.

[207] T. A. Bormotova and R. Blumenthal. *Ultraviolet Laser Ablation of Polycarbonate and Glass in Air*. Journal of Applied Physics, 105(3):034910, 2009.

[208] S. D. Gilev and A. M. Trubachev. *Metallization of Silicon in a Shock Wave: the Metallization Threshold and Ultrahigh Defect Densities*. Journal of Physics: Condensed Matter, 16:8139–8153, 2004.